



THE HONG KONG
POLYTECHNIC UNIVERSITY

香港理工大學

Pao Yue-kong Library

包玉剛圖書館

Copyright Undertaking

This thesis is protected by copyright, with all rights reserved.

By reading and using the thesis, the reader understands and agrees to the following terms:

1. The reader will abide by the rules and legal ordinances governing copyright regarding the use of the thesis.
2. The reader will use the thesis for the purpose of research or private study only and not for distribution or further reproduction or any other purpose.
3. The reader agrees to indemnify and hold the University harmless from and against any loss, damage, cost, liability or expenses arising from copyright infringement or unauthorized usage.

IMPORTANT

If you have reasons to believe that any materials in this thesis are deemed not suitable to be distributed in this form, or a copyright owner having difficulty with the material being included in our database, please contact lbsys@polyu.edu.hk providing details. The Library will look into your claim and consider taking remedial action upon receipt of the written requests.

The Hong Kong Polytechnic University

Department of Mechanical Engineering

**A Numerical Study of Supersonic Particle-Laden
Flow in Cold Gas Dynamic Spray Coating Process**

HO CHEUK YEI

**A thesis submitted in partial fulfillment of the requirements for
the degree of Master of Philosophy**

February 2012

CERTIFICATE OF ORIGINALITY

I hereby declare that this thesis is my own work and that, to the best of my knowledge and belief, it reproduces no material previously published or written, nor material that has been accepted for the award of any other degree or diploma, except where due acknowledgement has been made in the text.

_____ (Signed)

_____ HO CHEUK YEI _____ (Name of student)

Abstract

The cold gas dynamic spray (CGDS) process is a promising coating technology to produce high strength, strong corrosion resistance and excellent wear-resistant coating. The CGDS has many advantages over the conventional thermal spray methods, which uses kinetic energy, instead of using thermal energy, to bond the coating materials to the target substrates at a relatively low temperature without melting the materials, so many deleterious high-temperature reactions can be avoided. Therefore this technology is able to equip the manufacturers to meet more stringent requirements of engineering components they produce.

However, CGDS is not free from barriers for more advanced development. The key problem of the CGDS developers is facing is there lacks a control mechanism on the focusing of the particle beam. This problem leads to loss of costly coating powder which results in loss of deposition efficiency. Since the deposition efficiency is strongly related to the gas dynamics of the impinging jet flow, a more detailed study of the flow dynamics is needed to provide a better understanding of this process.

In this project, a two-step numerical methodology is developed to simulate the CGDS process. In the first step the gas dynamics involved in CGDS process is studied. It essentially consists of a development of supersonic flow within CGDS nozzle followed by a supersonic jet impinging on the substrate. To simulate the CGDS process, numerical simulations are carried out using a numerical scheme called conservation element and solution element (CE/SE) scheme. The CE/SE framework is a high resolution, multidimensional numerical framework that solves conservation laws in both space and time simultaneously, and able to resolve the conflict between numerical stability and accuracy. The CE/SE scheme has been successfully applied to many flow problems, including unsteady Euler flow, waves, travelling and interacting shock, explosion waves etc.

The CE/SE solver used in this project is originally developed to solve low Mach number aeroacoustics problems. Therefore, it needs to prove and validate the solver is also capable of simulating supersonic impinging jet flow which may carry shock waves. The validation tasks include simulations of free supersonic jet issuing from a convergent-divergent nozzle operating at design/off-design pressure ratio, and simulations of selected supersonic impinging jet benchmark problem. The CE/SE solver is capable of

reproducing some key features of these problems, such as shock cells at the nozzle exit of free supersonic jet problem, lambda shock system inside and overexpanded nozzle, stand-off shock and shear layer at the impinging zone of the impinging jet problem etc. The CE/SE numerical results show good agreement with existing experimental and numerical data. This shows that the CE/SE solver is capable of studying CGDS flow problem.

In CGDS process, coating particles are injected in to the CGDS nozzle where they are accelerated by the drag force whose magnitude is determined by the velocity difference between particle and carrier gas. Therefore, as the second step of the numerical methodology, a particle model is developed to calculate the drag coefficient based on the particle Reynolds number, and applied to the flow field results to calculate the particle flight path. The particles exit the nozzle with a very high velocity and gain heat energy from the preheated carrier gas. When they impact on the substrate, they either bounce off or deposit on the substrate surface. The impact speed of particle is an important parameter that has to exceed a critical value for successful deposition. A deposition model is thus developed to account for such deposition process. The impact location, impact speed and temperature of each particle are captured during its flight and the data is analyzed in more

details. The relationship between the nozzle stand-off distance, spray area and some such CGDS operating parameters as nozzle pressure ratio, temperature of carrier gas, particle inject locations are investigated and reported.

Acknowledgements

I would like to express my gratitude for the guidance, patience and financial support given by Dr Leung Chi-Kin, Randolph. I wish to extend my appreciation to Dr Shek Chan-Hung (Department of Physics and Materials Science, City University of Hong Kong) for his encouragement and invaluable help over the year. I would also like to thank Professor Jiang Zonglin (Institute of Mechanics, Chinese Academy of Sciences, Beijing, China) for his supervision and thoughts. Last but not least, funding support received from The Hong Kong Polytechnic University (through Grant No. G-U840) is gratefully acknowledge.

Table of Contents

| | |
|---|-----------|
| 1. Introduction | 1 |
| 1.1 Background | 1 |
| 1.2 History of CGDS development | 3 |
| 1.3 Working principles of CGDS | 5 |
| 1.4 Advantages of CGDS process | 7 |
| 1.5 One-dimensional nozzle gas dynamics model | 9 |
| 1.6 Gas dynamics of supersonic impinging jet | 16 |
| 1.7 Objective of present study | 18 |
| | |
| 2. Problem Formulations and Numerical Methods | 21 |
| 2.1 Governing equations of CGDS flow | 21 |
| 2.2 Non-dimensionalisation of the governing equations | 24 |
| 2.3 The flow solver | 25 |
| 2.3.1 CE/SE framework | 26 |
| 2.3.2 Conservation elements (CEs) and solution elements (SEs) | 30 |
| 2.3.3 Properties of CEs and SEs | 34 |

| | | |
|-----------|--|-----------|
| 2.3.4 | Solution scheme | 37 |
| 2.3.5 | Initial conditions | 38 |
| 2.3.6 | Boundary conditions | 39 |
| 2.4 | The particle models | 42 |
| 2.4.1 | Particle flight model | 42 |
| 2.4.2 | Particle impact model | 45 |
| 2.4.3 | Particle heat transfer model | 47 |
| 2.5 | Conclusions | 48 |
| 3. | Validation of the Flow Solver | 50 |
| 3.1 | Supersonic free jet from an underexpanded nozzle | 51 |
| 3.1.1 | Numerical setup | 52 |
| 3.1.2 | Results and discussions | 56 |
| 3.2 | Supersonic free jet from an overexpanded nozzle | 59 |
| 3.2.1 | Numerical setup | 61 |
| 3.2.2 | Results and discussions | 62 |
| 3.3 | Supersonic impinging jet form a straight duct | 68 |
| 3.3.1 | Numerical setup | 69 |
| 3.3.2 | Results and discussions | 71 |
| 3.4 | Conclusions | 73 |

| | |
|---|-----|
| 4. Results of CGDS Simulations | 74 |
| 4.1 Gas dynamics studies of the CGDS process | 75 |
| 4.1.1 Supersonic free jet simulation from the CGDS nozzle | 75 |
| 4.1.2 CGDS gas dynamics simulations | 81 |
| 4.2 Particle simulations | 96 |
| 4.2.1 Initial particle data | 96 |
| 4.2.2 Particle motion | 97 |
| 4.2.3 Heat transfer of particle | 101 |
| 4.2.4 Deposition of particle | 104 |
| 4.3 Conclusions | 109 |
| 5. Conclusions | 111 |
| References | 112 |

1. Introduction

1.1 Background

The cold gas dynamics spray (CGDS) process is a relatively new material deposition technology with many advantages over the conventional thermal spray methods and is able to equip manufacturers to meet the more stringent requirements of the engineering components which they produce. The CGDS process is an innovative and promising coating technology to produce high strength, strong corrosion resistant and excellent wear-resistant coatings. It uses kinetic energy, instead of using thermal energy, to bond the coating materials to the target substrates at a relatively low temperature without melting the materials. Therefore CGDS is also known as the aerosol deposition method (ADM) and kinetic spray coating method. Since the CGDS process is based on kinetic energy available from the high velocity of the coating powder rather than high temperature, many deleterious high-temperature reactions can be avoided. Moreover the CGDS particle beam is extremely narrow. This narrow high-density particle beam of CGDS results in a fast growth rate of coating thickness which allows better control over the shape of the coating. These advantages make the CGDS process a valuable technology for the production of high-end components requiring

higher precision; it should become a more popular choice of high-end component manufacturers in the future. More detailed features of the CGDS process will be discussed in later sections.

Albeit that it has a promising future, CGDS is not free from barriers for further development. The key problem that CGDS developers are facing is the lack of a control mechanism to focus the particle beam. This problem leads to loss of costly powder which results in loss of deposition efficiency. This problem makes CGDS technology still not good enough for wider adoption. There are many areas that can be improved. For example, the coating area of the current CGDS system is small due to the small cross-sectional area of the spray nozzle. The only way to control the coating area is to adjust the stand-off distance (SOD) between the nozzle exit and the substrate surface, together with the nozzle supply pressure. However the proper SOD and pressure are highly sensitive to the choice of powder materials and the discharge rate. Currently the optimal conditions can be achieved only by carrying out large numbers of experiments which is time-consuming and wastes a large amount of costly powder.

Since the powder transport is strongly related to the gas dynamic characteristics of the supersonic powder-laden impinging flow, these

characteristics include boundary layer problems on the nozzle wall, impinging effects in front of the substrate, structure and instability of the supersonic jet, etc. Therefore, a clear understanding of the spray flow mechanism is very important, which can provide new directions for the advancement of the CGDS technology with higher deposition efficiency and flexibility. The knowledge of CGDS gas dynamics can also be applied to other engineering problems involving supersonic impinging jets, such as vertical take-off-and-landing (VTOL) aircraft technology because the geometrical setup and its physics show a high degree of similarity to the CGDS process.

1.2 History of CGDS development

The concept of combining kinetic and thermal energies of high-velocity powder to make coatings was proposed in 1950s (Smith et al. 1958) and the application developments of CGDS were started in the 1980s. The discovery of this new coating technology was an unexpected outcome when scientists were conducting particle erosion experiments (Dykhuisen and Smith 1998). During their experiments, rapid deposition on the substrate was observed instead of erosion when the velocities of particles exceeded a critical velocity. This discovery drew the attention of some scientists and the studies of

possible applications were carried out. The first CGDS system was originally developed in the Institute of Theoretical and Applied Mechanics of the Russian Academy of Science in Novosibirsk (Alkhimov et al. 1990). The group deposited a wide range of materials and demonstrated the ability of the CGDS process for a number of applications and Russian patents were issued in 1990 and 1992 (Alkhimov et al. 1990, 1992). A US patent was issued in 1994 (Alkhimov et al. 1994) and a European patent was issued in 1995 (Alkhimov et al. 1995).

This new technology then became one of the subjects of a project undertaken by a group of companies under the auspices of the National Centre for Manufacturing Science (NCMS) of Ann Arbor, MI USA. The members came from different fields of engineering companies, namely Flame Spray Industries, Ford Motor Company, General Electric-Aircraft Engines, General Motors Corporation, The Naval Aviation Depot, TubalCain Company, and the Pratt and Whitney Division of United Technologies Corporation (McCune et al. 1995). This group of companies has carried out research on a wide range of applications of cold spray technology.

Some similar research projects were carried out afterwards. Browning (1993) proposed injecting powder into the high-speed gas

downstream of an internal combustor, through impact energy transformation; the temperature was raised to a level high enough to fuse the powder into a dense coating. Tapphorn and Gabel (1998, 2000, 2004) developed a similar CGDS process in the 1990s and the kinetic metallization (KM) process was perfected and patented in Inovati, Santa Barbara, CA USA. The feature of the KM process was the use of a specially designed and patented sonic nozzle instead of supersonic nozzle to produce high-speed particles of lower cost and complexity. Van Steenkiste *et al.* (2001, 2005) made important improvements over the original process proposed by Alkhimov *et al.* (2005). Data recording devices were installed for feedback control of process variables which enhanced systematic analysis of the cold spray process. In the recent decade, different kinds of CGDS research were conducted in the US, Russia, Germany and Japan (Payrin 2001). Such research included gas dynamics, impact of high velocity particles, coating materials and the development of specific applications.

1.3 Working principles of CGDS

The major difference between CGDS technology and conventional thermal spray technology is the idea of using of kinetic energy instead of thermal energy. Therefore the kinetic energy of the coating particles plays an

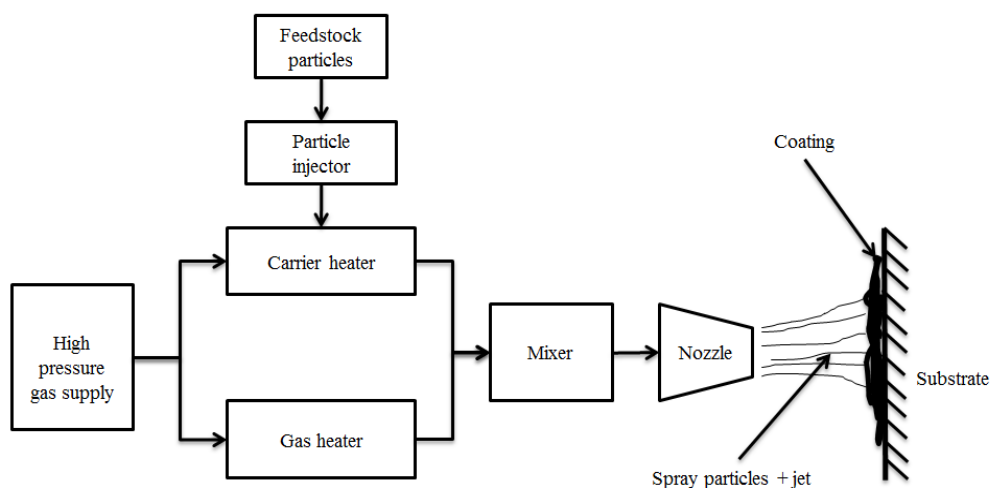


Figure 1.1 Schematic of the setup of a typical CGDS system.

important role during the process. Figure 1.1 shows the setup of a typical CGDS system. The feedstock particles are first preheated and mixed with the preheated high pressure gas in the mixing chamber. The mixture is then accelerated to a supersonic velocity by the rapid gas expansion inside the supersonic nozzle. The high-speed mixture leaves the nozzle and travels towards the substrate. When a particle impacts on the substrate, it either bounces off from or, deforms and bonds to the substrate, depending on the impact velocity of the particle. Research studies show that if the impact velocity of a particle is below a critical value, the particle bounces off and the substrate erodes instead of a coating being formed (Alkhimov et al. 1994). In contrast, if the particle impact velocity reaches the critical value, its kinetic

energy is high enough for it to undergo deformation. In this situation, deposition becomes possible and a coating can be formed on the substrate surface as a result. A large number of experimental studies (Alkhimov *et al.* 1994) reveal that the critical velocity of a particle can be estimated by:

$$\bar{V}_c = 667 - 14\bar{\rho}_g + 0.08\bar{T}_M + 0.1\bar{\sigma}_u - 0.4\bar{T}_i , \quad (1.1)$$

where $\bar{\rho}_g$ is the particle mass density (g/cm^3), \bar{T}_M is the particle melting temperature ($^{\circ}\text{C}$), $\bar{\sigma}_u$ is the particle material ultimate strength (MPa) and \bar{T}_i is the particle impact temperature ($^{\circ}\text{C}$) (Schmidt 2003). Here the bar indicates the dimensional variable and the same notation is adopted in this thesis. From Equation (1.1), it is clear that higher values of impact temperature \bar{T}_i enhance deposition because \bar{V}_c is lowered. Therefore preheated carrying gas and particles provide a more favorable condition for deposition to occur. However the preheat temperature is limited and material dependent due to the consideration of high temperature effects (Raletz 2005; Schmidt 2006).

1.4 Advantages of the CGDS process

The deleterious effects of high temperature in conventional thermal spray processes (such as evaporation, melting, oxidation, crystallization,

debonding, gas release and residual stresses) can be avoided in the CGDS process (Payrin 2011), because the operating temperature is relatively low compared to thermal spray processes, and both coating materials and the substrate are kept in a solid state throughout the CGDS process. Therefore a wider range of materials, including some oxygen sensitive and thermal sensitive coating materials, (such as pure metals, steels, nickel-chromium alloys, nickel-based super alloys, stainless steels, zinc alloys, aluminium alloys, copper alloys, composites and cermets) can be used in CGDS due to the relatively low temperature environment. In addition, some intermetallic, amorphous and nanophase materials which are not suitable for thermal spray processes can be cold sprayed. Table 1.1 shows some typical CGDS process parameters (Papyrin 2001). The carrier gas used can be air, nitrogen, helium or a mixture of these. In fact CGDS also provides benefits to some of the mechanical behaviour of the coating materials. The “peening” effect of impinging particles can benefit the compressive residual stresses. Since CGDS coatings are largely free of porosity and oxidation, post-deposition heat treatment can be applied to improve the ductility of the spray metal. Last but not least, the CGDS technology allows the reuse of overspray particles, thus providing higher deposition efficiency than conventional

thermal spray. These advantages make CGDS a valuable alternative coating method for precision products due to its relatively low cost.

| | |
|------------------------------------|----------|
| Stagnation jet pressure, (MPa) | 1-3 |
| Stagnation jet temperature, K | 600-1000 |
| Gas flow rate, m ³ /min | 1-2 |
| Powder feed rate, kg/h | 2-8 |
| Stand-off distance, mm | 10-50 |
| Power consumption, kW | 5-25 |
| Particle size, μm | 1-50 |

Table 1.1 Typical parameters of the CGDS process.

1.5 One-dimensional nozzle gas dynamics model

As mentioned before, the impact velocity of the spraying particles is critical to successful CGDS deposition. Clearly this impact velocity is influenced by the nozzle geometry and flow variables such as pressure, temperature and density of the particle carrying flow. A one-dimensional nozzle gas dynamics model is adopted (Dykhuizen and Smith 1998) to predict the spray particle velocity and this model can also be applied to determine the optimal design

of the nozzle. Figure 1.2 shows a typical supersonic nozzle used in CGDS systems which is essentially composed of a converging and a diverging section. This type of convergent-divergent (C-D) nozzle is also known as a de Laval-type nozzle. The flow variables at the reservoir are \bar{p}_0 , $\bar{\rho}_0$, \bar{T}_0 , which

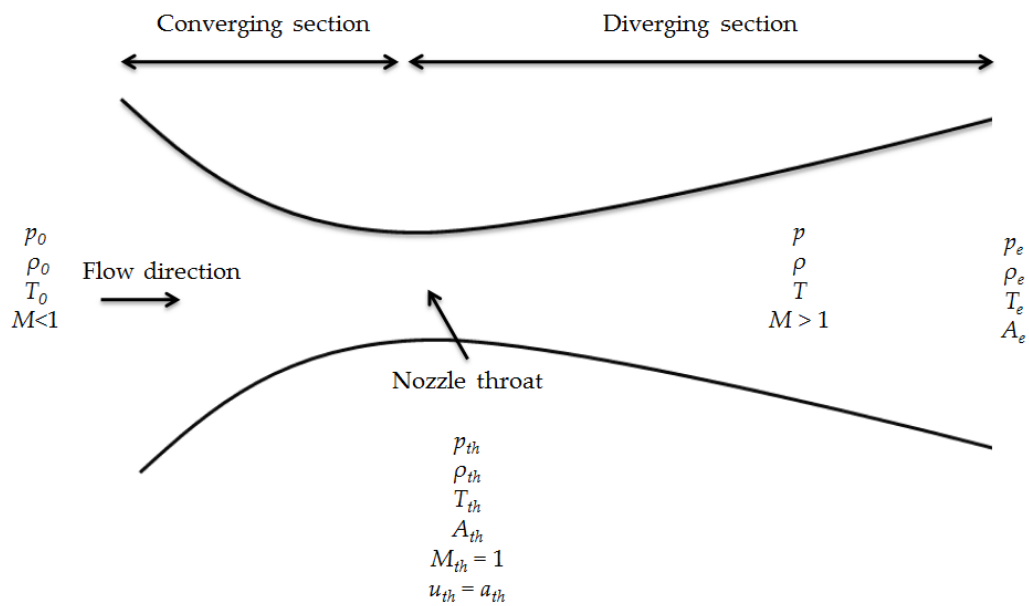


Figure 1.2 A supersonic nozzle.

are the stagnation pressure, stagnation density and stagnation temperature of the supply gas. The ratio of stagnation pressure \bar{p}_0 to ambient pressure \bar{p}_a is called the normal pressure ratio (NPR), which is the key parameter of the supply gas. The nozzle cross-section area is the smallest at the throat where the flow variables are indicated with the subscript "th" (i.e. \bar{p}_{th} , $\bar{\rho}_{th}$, \bar{T}_{th} , \bar{u}_{th} and \bar{A}_{th} represent the pressure, density, temperature, streamwise

velocity and throat cross-sectional area respectively). The subsonic gas ($M = \bar{u}/\bar{a} < 1$) is accelerated while passing through the nozzle convergent section and reaches sonic speed \bar{a}_{th} at the nozzle throat, i.e. $\bar{u}_{th} = \bar{a}_{th}$; the local Mach number M_{th} is thus at unity at the nozzle throat. The speed of sound \bar{a}_{th} at the nozzle throat can be calculated from:

$$\bar{a}_{th} = \sqrt{\gamma \bar{R} \bar{T}_{th}}, \quad (1.2)$$

where γ is the ratio of constant-pressure specific heat \bar{c}_p to constant-volume specific heat \bar{c}_v and \bar{R} is the gas constant (the universal gas constant divided by the gas molecular weight). Equation (1.2) shows that monoatomic helium is a better carrier gas than diatomic air because helium has a larger \bar{R} due to its lower atomic weight, and hence a higher speed of sound. The temperature \bar{T}_{th} , pressure \bar{p}_{th} and density $\bar{\rho}_{th}$ can be calculated by applying isentropic relations, so that:

$$\frac{\bar{T}_0}{\bar{T}_{th}} = \left(1 + \frac{\gamma - 1}{2}\right), \quad (1.3)$$

$$\frac{\bar{p}_0}{\bar{p}_{th}} = \left(1 + \frac{\gamma - 1}{2}\right)^{\gamma/(\gamma-1)}, \quad (1.4)$$

$$\frac{\bar{\rho}_0}{\bar{\rho}_{th}} = \left(1 + \frac{\gamma - 1}{2}\right)^{1/(\gamma-1)}. \quad (1.5)$$

The variation of the nozzle cross-sectional area can be specified to determine the corresponding local Mach number M from the expression below:

$$\frac{\bar{A}}{\bar{A}_{th}} = \frac{1}{M} \left[\left(\frac{2}{\gamma+1} \right) \left(1 + \frac{\gamma-1}{2} M^2 \right) \right]^{(\gamma+1)/2(\gamma-1)}. \quad (1.6)$$

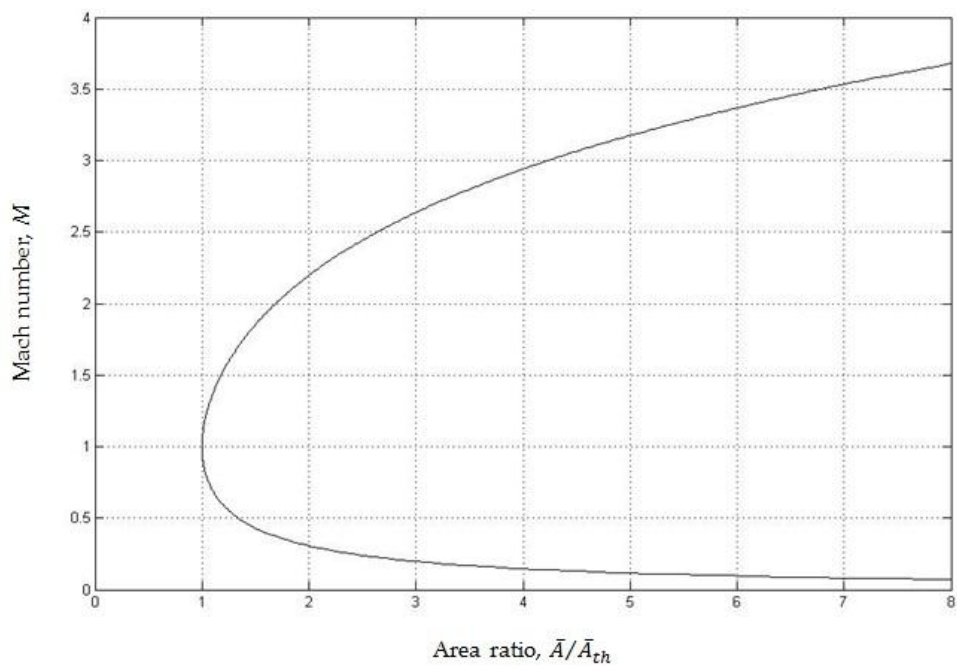


Figure 1.3 Relationship between local Mach number and the nozzle area ratio.

The lower part of the curve represents the solution in the converging zone where the flow is subsonic and the upper part of the curve represents the

solution in the diverging zone where the flow is supersonic.

Once the local Mach number has been determined, the quantities ($\bar{\rho}$, \bar{p} , \bar{T} , \bar{a} and \bar{u}) along the nozzle can also be readily calculated by using the isentropic relations:

$$\frac{\bar{T}_0}{\bar{T}} = \left(1 + \frac{\gamma - 1}{2} M^2\right) , \quad (1.7)$$

$$\frac{\bar{p}_0}{\bar{p}} = \left(1 + \frac{\gamma - 1}{2} M^2\right)^{\gamma/(\gamma-1)} , \quad (1.8)$$

$$\frac{\bar{\rho}_0}{\bar{\rho}} = \left(1 + \frac{\gamma - 1}{2} M^2\right)^{1/(\gamma-1)} . \quad (1.9)$$

The above equations can also be used to calculate the \bar{p}_e , \bar{T}_e , \bar{u}_e and $\bar{\rho}_e$ at the nozzle exit if the exit cross-sectional area \bar{A}_e is known.

One should note that Equations (1.7) to (1.9) cannot be applied to the situation where a shock wave exists inside the nozzle (Figure 1.4). For a completely shock-free isentropic supersonic flow issuing from a nozzle, the exit pressure ratio can be expressed as:

$$\bar{p}_e = \bar{p}_0 \left(1 + \frac{\gamma - 1}{2} M_e^2\right)^{-\gamma/(\gamma-1)} . \quad (1.10)$$

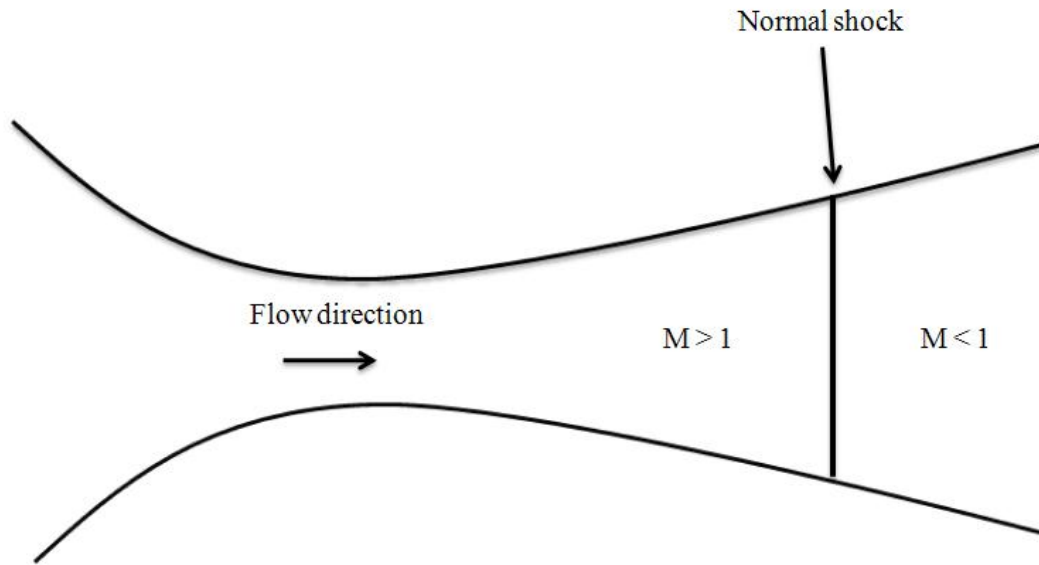


Figure 1.4 A normal shock exists in the diverging section of a nozzle.

When \bar{p}_e is less than the ambient pressure \bar{p}_a outside the nozzle, nothing happens at the convergent section but a normal shock wave emerges inside the divergent section as shown in Figure 1.4. There is a supersonic flow region upstream of the shock and a subsonic flow region downstream. The change of pressure and the Mach number across the shock is sharp and the change in Mach number and pressure ratio across the shock can be calculated by using the normal shock relationship:

$$M_2^2 = \frac{1 + [(\gamma - 1)/2]M_1^2}{\gamma M_1^2 - (\gamma - 1)/2}, \quad (1.11)$$

$$\frac{p_2}{p_1} = 1 + \frac{2\gamma}{\gamma + 1}(M_1^2 - 1), \quad (1.12)$$

where M_1 and M_2 are the Mach number upstream and downstream of the across shock.

If the back pressure outside the nozzle is less than the nozzle exit pressure, the flow inside the nozzle is fully supersonic and isentropic but an oblique shock is formed outside the nozzle (Figure 1.5). In the CGDS process, the appearance of a shock inside the nozzle should be avoided. In the absence of a shock inside the nozzle, the exit pressure \bar{p}_e can be determined by Equation (1.10) and it is usually lower than the ambient pressure in an

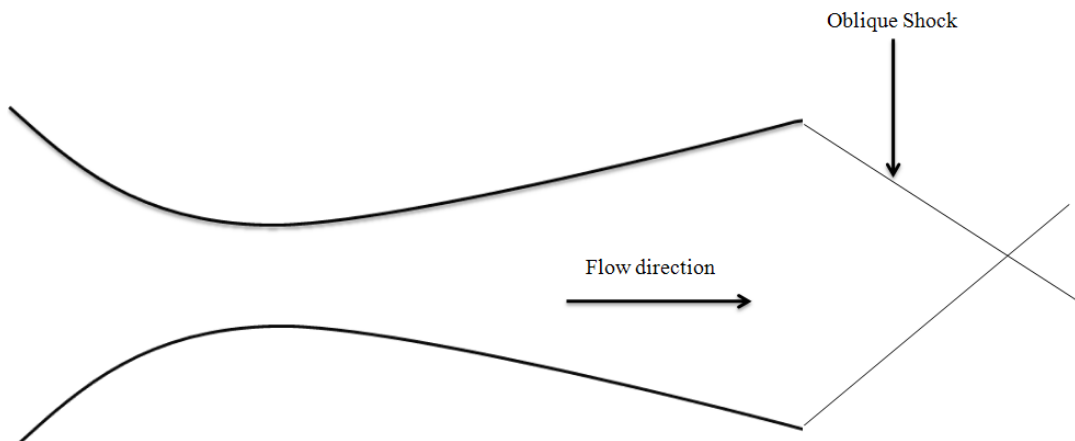


Figure 1.5 Oblique shock exists outside the nozzle.

effort to maximize the exit velocity of the gas. Because of the relatively short standoff distance (SOD) between nozzle exit and substrate surface, the

reduction of flow velocity is not significant so exit gas velocity \bar{u}_e can be used as a good approximation of the gas velocity at the substrate surface.

However, the uniform flow properties of the one-dimensional steady flow model are too simplified for predicting the results of the flow characteristics of the CGDS nozzle flow. This usually leads to overloading of coating particles, bad focusing and reduction in deposition efficiency of the CGDS process (Middha and Wexler 2003, 2005; Taylor et al. 2006).

1.6 Gas dynamics of the supersonic impinging jet

The gas dynamics of CGDS consist of two parts: nozzle flow and supersonic impinging jet. The mechanism of nozzle flow has been discussed in previous sections, but an understanding of the supersonic impinging jets mechanism is also important to give a clear picture of the CGDS process. Impinging jet flows have been studied by aerodynamic and aeroacoustic researchers for more than 30 years (Neuwerth 1974; Powell, 1988; Tam and Ahuja 1990; Henderson and Powell 1993; Krothapalli et al. 1999). A primary result of such aeroacoustic research is the highly unsteady and oscillatory behaviour of the impinging jet, which is strongly related to the discrete and high-amplitude acoustic tones caused by the feedback loop (Powell 1953). The flow structures of impinging jets were also studied in a number of studies

(Carling and Hunt 1974; Lamont and Hunt 1980). Some studies provided an insight into the impinging zone such as the condition for formation of a stagnation bubble (Gubanova et al. 1973; Gumer and Hunt 1974).

The impinging jet flow field can be divided into three main regions, namely the main jet column, the impinging zone and the distinct region. Inside the main jet column, the flow is primarily inviscid and contains shock waves and expansion. The impinging zone is a region characterized by strong gradients leading to sharp changes in local flow properties. Inside the

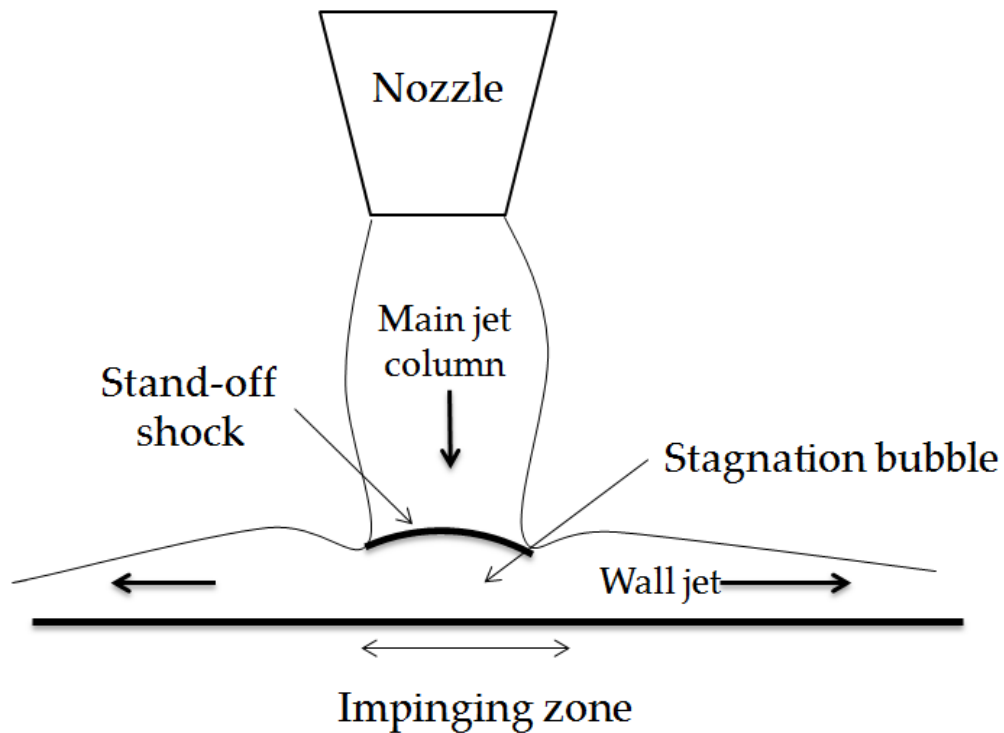


Figure 1.6 Structure of flow field in the impinging zone.

impinging zone, a stand-off shock is formed in front of the substrate, which encloses a region of recirculating, high-density and low-velocity flow (Donaldson and Snedeker 1974). The distinct region is the region in which jet flow is directed outward after impingement. All these regions are shown in Figure 1.6. The distance between the stand-off shock and the substrate surface is given by Billig's approximation (Billig 1967) as:

$$\Delta = 0.143 \bar{d}_e \left[\exp(3.24/M_e^2) \right], \quad (1.13)$$

where \bar{d}_e and M_e are the nozzle diameter and flow Mach number at the nozzle exit.

1.7 The objective of the present study

Understanding the gas dynamics of the CGDS process is crucial for further advancement of this technology. Computational simulation is an effective way to carry out these studies as it is relatively cheap compared to experiments. In the present study, a two-step approach is adopted to simulate the CGDS process. The simulation of supersonic impinging jet problems is firstly carried out, and then a particle model is applied using the numerical results calculated from the flow simulation.

The numerical simulation of the flow is based on a numerical framework called space-time conservation element and a solution element method (CE/SE) is applied to solve the CGDS gas dynamic problems. This numerical framework will be discussed in Chapter 2. Apart from gas dynamics simulations, three particle models are developed to simulate particle motion and energetics, namely, the particle flight model which is used to determine the flight path of each particle; the particle impact model which is used to determine the impact between particle and the substrate; and the heat transfer model which is used to determine the heat transfer mechanism between carrying gas and particle. All the formulations of the particle models are discussed in Chapter 2.

Before the CGDS gas dynamic simulations are carried out, some validation work should be done in order to ensure that the CE/SE framework is suitable for our problem. The validation work is done by comparing the numerical results of CE/SE simulations to existing results of the same benchmark problems, such as the flow inside a supersonic nozzle and supersonic impinging jet problems.

Once the validations of the CE/SE solver are completed, the flow simulations of the CGDS process can be carried out. After that, the particle

models can be applied to these flow results to simulate the particles in the CGDS process. The flight path and other information, such as temperature and velocity of each particle are studied in order to give a better understanding of the CGDS process. Therefore the future CGDS system can be enhanced, operate more efficiently at lower cost and be adopted widely in industry.

2 Problem Formulation and Numerical Method

The formulation governing the supersonic particle-laden flow problem and the numerical method adopted in the present study are discussed in this chapter. In the first part of this chapter, the governing equations of the CGDS gas dynamics and the numerical method adopted are described. The second part of this chapter discusses the formulation that governs the particle transport, heat transfer between the particle and carrying gas, and the impact of particles on substrate, followed by a discussion of numerical methods that are adopted to simulate the supersonic particle-laden flow problem.

2.1 Governing equations of CGDS flow

The gas dynamics of the CGDS process involve both supersonic flow and shock waves, implying that the flow should be treated as a compressible and viscous flow. Assuming that the carrying gas is a perfect gas, the compressible Navier-Stokes (N-S) equations and equation of state can be applied to the problem. The N-S equations state that mass, momentum and energy should be conserved. In dimensional form, where the flow quantities are denoted with an overbar, the mass conservation requires that:

$$\frac{\partial \bar{\rho}}{\partial \bar{t}} + \frac{\partial \bar{\rho} \bar{u}_j}{\partial \bar{x}_j} = 0, \quad (2.1)$$

where $\bar{\rho}$, \bar{u}_i , \bar{x}_j and \bar{t} represent the density, velocity, spatial coordinate and time respectively. Momentum conservation requires that:

$$\frac{\partial \bar{\rho} \bar{u}_i}{\partial \bar{t}} + \frac{\partial \bar{\rho} \bar{u}_i \bar{u}_j}{\partial \bar{x}_j} = \bar{\rho} \frac{D \bar{u}_i}{D \bar{t}} = - \frac{\partial \bar{p}}{\partial \bar{x}_i} + \frac{\partial \bar{\tau}_{ij}}{\partial \bar{x}_j}, \quad (2.2)$$

Energy conservation requires that:

$$\frac{\partial \bar{\rho} \bar{h}}{\partial \bar{t}} + \frac{\partial \bar{\rho} \bar{h} \bar{u}_i}{\partial \bar{x}_i} = \bar{\rho} \frac{D \bar{h}}{D \bar{t}} = \frac{D \bar{p}}{D \bar{t}} + \bar{\phi} - \frac{\partial \bar{q}_i}{\partial \bar{x}_i} + \bar{Q}, \quad (2.3)$$

where \bar{Q} is the rate of heat addition per unit volume, \bar{h} is the enthalpy and $D/D\bar{t} = \partial/\partial\bar{t} + \bar{u}_i \partial/\partial\bar{x}_i$ is the material derivative. The viscous stress $\bar{\tau}_{ij}$, the molecular heat flux \bar{q}_i and the rate of viscous dissipation of energy $\bar{\phi}$ are given by:

$$\bar{\tau}_{ij} = 2\bar{\mu} \left\{ \bar{S}_{ij} - \frac{1}{3} \delta_{ij} \bar{S}_{kk} \right\}, \quad (2.4)$$

$$\bar{q}_i = -\bar{k} \frac{\partial \bar{T}}{\partial \bar{x}_i}, \quad (2.5)$$

$$\bar{\phi} = \bar{\tau}_{ij} \bar{S}_{ij}. \quad (2.6)$$

In Equations (2.4) and (2.5), $\bar{\mu}$ is the viscosity of gas and \bar{k} is the thermal conductivity with the strain rate given by:

$$\bar{S}_{ij} = \frac{1}{2} \left\{ \frac{\partial \bar{u}_i}{\partial \bar{x}_j} + \frac{\partial \bar{u}_j}{\partial \bar{x}_i} \right\}. \quad (2.7)$$

The equation of state of perfect gas reads:

$$\bar{p} = \frac{\bar{\rho} \bar{R}_u \bar{T}}{\bar{W}}, \quad (2.8)$$

where \bar{R}_u is the universal gas constant and \bar{W} is the molecular weight of the gas. The specific heats of constant pressure and constant volume are defined as:

$$\bar{c}_p = \frac{\bar{R}_u \gamma}{(\gamma - 1) \bar{W}}, \quad (2.9)$$

$$\bar{c}_v = \frac{\bar{R}_u \gamma}{(\gamma - 1) \bar{W}}. \quad (2.10)$$

2.2 Normalization of the governing equations

The N-S equations (Eqs. 2.1–2.3) and the equation of state (Eq. 2.8) can be normalized by a length scale \bar{L}_{ref} , a velocity scale \bar{a}_{ref} , a density scale $\bar{\rho}_{ref}$, a time scale $\bar{L}_{ref}/\bar{a}_{ref}$ and a pressure scale $\bar{\rho}_{ref} \bar{a}_{ref}^2$, where \bar{a}_{ref} and $\bar{\rho}_{ref}$ are the speed of sound and density in ambient far away from the nozzle. The normalized equations are:

$$\frac{\partial \rho}{\partial t} + \frac{\partial \rho u_i}{\partial x_i} = 0, \quad (2.11)$$

$$\rho \frac{Du_i}{Dt} = -\frac{\partial p}{\partial x_i} + \frac{M}{Re} \frac{\partial \tau_{ij}}{\partial x_j}, \quad (2.12)$$

$$\rho \frac{Dh}{Dt} = \frac{Dp}{Dt} + \frac{M}{Re} \phi - \frac{M}{Re Pr} \frac{\partial q_i}{\partial x_i} + Q, \quad (2.13)$$

$$p = \frac{\rho T}{\gamma}, \quad (2.14)$$

where $M = \bar{u}/\bar{a}_{ref}$ is the Mach number, $Re = \bar{\rho}_{ref} \bar{a}_{ref} \bar{L}_{ref} / \bar{\mu}$ is the Reynolds number, $\bar{\mu}$ is the viscosity of the gas, $Pr = \bar{\mu} \bar{c}_p / \bar{k}$ is the Prandtl

number and \bar{k} is the thermal conductivity. These dimensionless quantities have physical meanings: the Reynolds number represents the ratio of fluid inertial and viscous forces, and the Prandtl number represents the ratio of viscous diffusion rate over thermal diffusion rate. The non-dimensional form of the governing equations can give a better understanding of the roles of different dimensionless quantities in the equations. Therefore all the equations used in the flow and particle simulations are in non-dimensional form.

2.3 The flow solver

As mentioned before, the CGDS flow is essentially supersonic compressible viscous flow; this means that a shock wave may develop in the flow. Traditional finite-difference methods such as the Lax-Wendroff scheme or MacCormack's scheme generally are not able to capture flow discontinuity with sufficient accuracy (Hirsch 1990). With the approach of von Neumann and Richtmyer (1950), this problem can be solved by adding artificial dissipation. Many wiggle-suppressing shock capturing schemes such as Harten's high resolution scheme, Yee's total variation diminishing (TVD) scheme (Yee *et al.* 1985) and the essentially non-oscillatory method (Harten *et al.* 1987), etc., are then developed for capturing shock. However the excessive

numerical damping makes the numerical scheme incapable of capturing small-scale flow features (Shu *et al.* 1992). Other numerical schemes such as spectral methods (Gottlieb and Orszag 1977) and the compact finite-difference scheme with spectral-like resolution (Lele 1992) possess higher accuracy and lower numerical dissipation; however the computation is complex and difficult to handle problems with complex geometry. This conflict between stability, flexibility and numerical accuracy can be resolved by the use of a new type of numerical scheme, the space-time conservation element and solution element (CE/SE) scheme (Chang 1995; Chang *et al.* 1998, 1999), which has been developed for low Mach number aeroacoustics (Lam *et al.* 2011).

2.3.1 CE/SE framework

The CE/SE framework is a high-resolution, multidimensional numerical framework developed at the NASA Glenn Research Centre (Chang 1995). With its principle of requiring strict conservation laws in both space and time simultaneously, it is able to resolve the conflict between numerical stability and accuracy. CE/SE is different from other conventional numerical methods such as finite difference, finite volume and spectral methods. With its mathematical simplicity, it has almost no numerical dissipation which

makes CE/SE an ideal framework for problems involving flow instability. In addition there are some unique features of this framework, including (i) a unified treatment of both space and time, (ii) enforcement of local and global space-time flux conservation, (iii) the space-time mesh that allows for evaluation of flux at the cell interface without solving the Riemann problem, (iv) originally a non-dissipative scheme but allows numerical dissipation if needed, (v) both flow variables and spatial derivatives being independent unknowns, (vi) and ad hoc numerical damping is avoided.

The non-dissipative core scheme fits the inviscid flow problems very well because it guarantees reversibility of the flow all the times. However for viscous flow problems, especially those involving shocks, an additional numerical dissipation scheme can be applied. The CE/SE framework has been successfully applied to several flow problems, such as unsteady Euler flows, acoustic waves, travelling and interacting shocks, explosion waves, etc. The two-dimensional unsteady N-S equations (Eqs. (2.1 – 2.3)) in strong conservation form are:

$$\frac{\partial u_m}{\partial t} + \frac{\partial f_m}{\partial x} + \frac{\partial g_m}{\partial y} - \frac{\partial f_{vm}}{\partial x} - \frac{\partial g_{vm}}{\partial y} = 0 , \quad (2.15)$$

where $m=1, 2, 3, 4$. In Equation (2.15), u_m represents the vector of flow

variables, and f_m and g_m represent the inviscid part of the fluxes in the x and y directions respectively. The quantities f_{vm} and g_{vm} represent the viscous part of the fluxes in the x and y directions respectively. These variables are defined as:

$$\begin{bmatrix} u_1 \\ u_2 \\ u_3 \\ u_4 \end{bmatrix} = \begin{bmatrix} \rho \\ \rho u \\ \rho v \\ \rho E \end{bmatrix}, \quad \begin{bmatrix} f_1 \\ f_2 \\ f_3 \\ f_4 \end{bmatrix} = \begin{bmatrix} \rho u \\ \rho u^2 + p \\ \rho uv \\ (\rho E + p)u \end{bmatrix}, \quad \begin{bmatrix} g_1 \\ g_2 \\ g_3 \\ g_4 \end{bmatrix} = \begin{bmatrix} \rho v \\ \rho uv \\ \rho v^2 + p \\ (\rho E + p)v \end{bmatrix}, \quad (2.16)$$

$$\begin{bmatrix} f_{v1} \\ f_{v2} \\ f_{v3} \\ f_{v4} \end{bmatrix} = \begin{bmatrix} 0 \\ \tau_{xx} \\ \tau_{xy} \\ u\tau_{xx} + v\tau_{xy} + q_x \end{bmatrix}, \quad \begin{bmatrix} g_{v1} \\ g_{v2} \\ g_{v3} \\ g_{v4} \end{bmatrix} = \begin{bmatrix} 0 \\ \tau_{xy} \\ \tau_{yy} \\ u\tau_{xy} + v\tau_{yy} + q_y \end{bmatrix}, \quad (2.17)$$

and
$$E = e + \frac{1}{2}(u^2 + v^2), \quad (2.18)$$

where τ_{xx} , τ_{yy} and τ_{xy} represent the normal and shear stresses, whereas q_x and q_y represent the heat diffusion fluxes (Venkatachari et al. 2004).

To solve the conservation law accurately, the numerical framework should be constructed to guarantee the conservation of flux in both space and time, not in space alone. To achieve this, CE/SE is constructed by utilizing the concept of unified treatment of space and time. The CE/SE framework for solving two-dimensional problems operates in a unique 3D

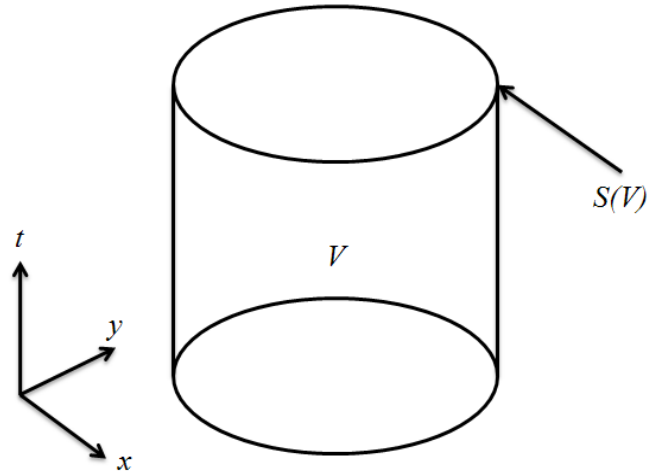


Figure 2.1 A surface element on the boundary $S(V)$ of a space time volume V .

Euclidean space E_3 as shown in Figure 2.1, in which, x , y and t as the three dimensions. In this E_3 space, all mathematics can be performed as an ordinary three-dimensional space. Applying Gauss divergence theorem in this E_3 space, the governing equations can be expressed in the integral form:

$$\oint_{S(V)} \mathbf{h}_m \cdot d\mathbf{s} = 0, \quad (2.19)$$

$$\mathbf{h}_m = (f_m - f_{vm'} g_m - g_{vm'} u_m), \quad (2.20)$$

where $S(V)$ is the boundary of the space-time volume V as shown in Figure 2.1, and $d\mathbf{s} = \mathbf{n} d\sigma$ where \mathbf{n} and $d\sigma$ are the unit normal and area of a surface

element on $S(V)$. Equations (2.19) and (2.20) show that the total space-time flux h_m leaving the volume V should vanish.

2.3.2 Conservation elements (CEs) and solution elements (SEs)

The grid system of the CE/SE framework is different from that of traditional method. A two-dimensional rectangular computational domain filled with a triangular mesh is shown in Figure 2.2. Consider the mesh $\triangle ABC$, and neighboring meshes $\triangle ACD$, $\triangle BCE$ and $\triangle ABF$: the filled circles shown in

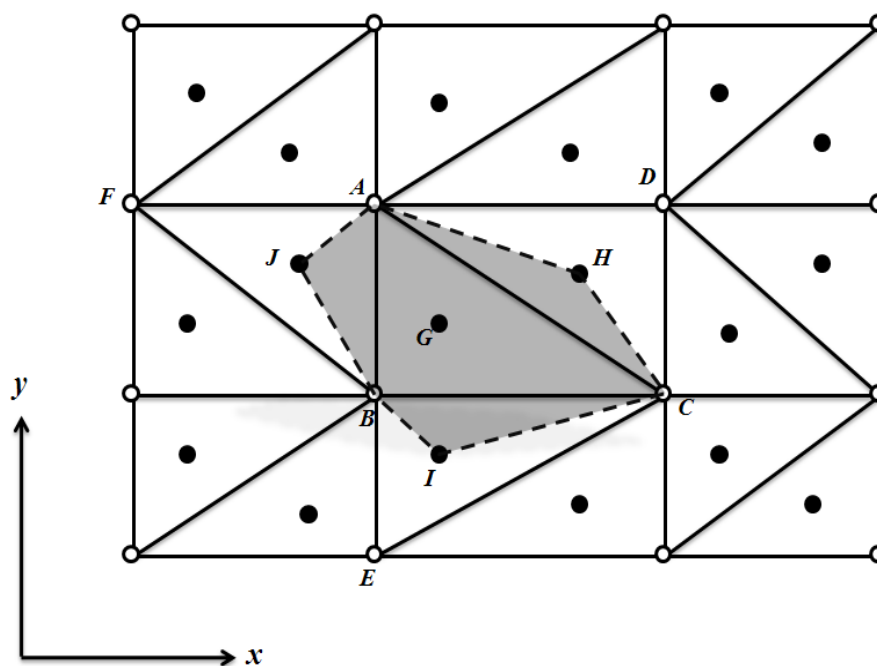


Figure 2.2 A two-dimensional domain filled with triangle meshes.

Figures 2.2 and 2.3 indicate the centroids of triangular elements as solid

circles. In the figures the open circles represent the vertices of the triangular elements; for example the point G is the centroid of $\triangle ABC$, and H , I and J are the centroids of neighboring triangles. The polygon $AHCIBJ$ is formed by joining the vertices of $\triangle ABC$ and centroids of neighboring elements. The centroid of the polygon, marked as G^* in Figure 2.3, is defined as the solution point associated with point G . Unlike other numerical methods, the flow variables are stored in the solution point G^* instead of the centroids and

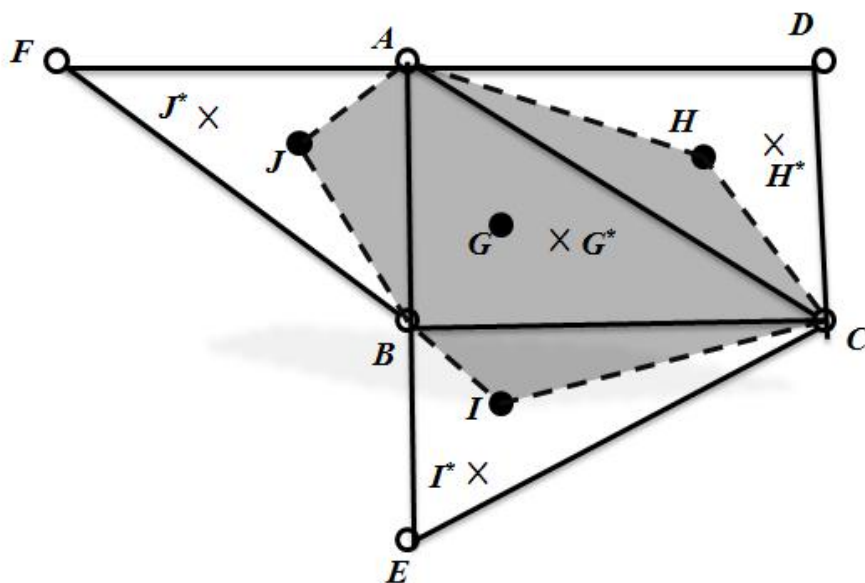


Figure 2.3 Definition of solution points.

vertices. The points H^* , I^* , and J^* are the solution points associated with points H , I , and J respectively. When this polygon is extruded along the time axis, conservation elements (CEs) associated with solution point (G^*, n) are formed, as shown in Figure 2.4. Here, $t = n\Delta t$ at the n -th time level, where $n=0, 1/2, 1, 3/2$, etc. For a given $n > 0$, G' , G , and G'' represent the mesh points at $(n-1/2)$ -th, n -th, and $(n+1/2)$ -th time levels respectively with point G

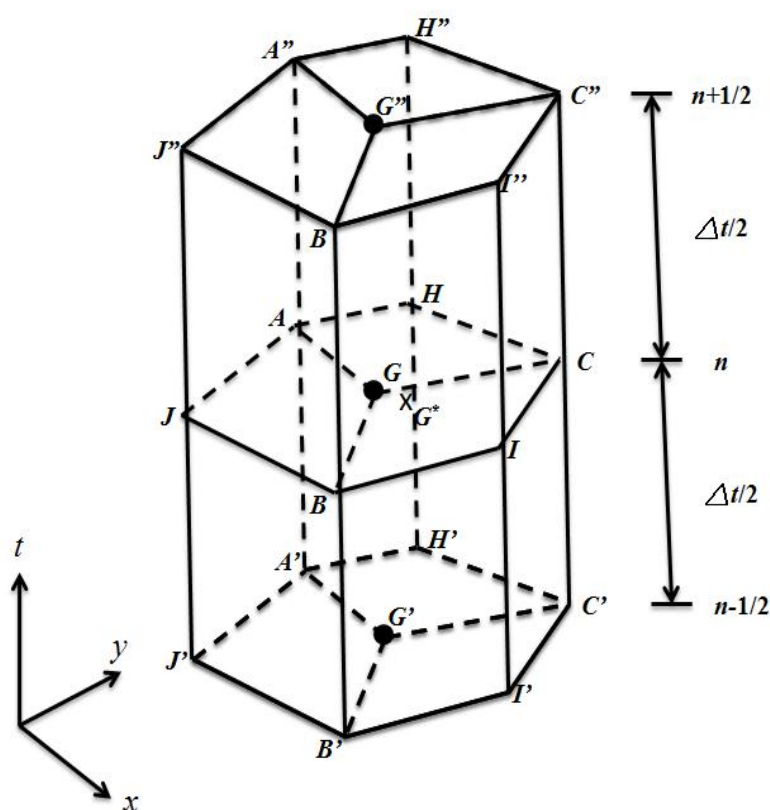


Figure 2.4 Definition of CE.

being their common spatial projection. The definition of solution element (SE) is given in Figure 2.5. In this figure the planes $A''A'G'G''$, $B''B'G'G''$, $C''C'G'G''$

and $AHCIBJ$ represent the SEs associated with solution point G^* . The SEs are non-overlapping space-time subdomains that are used for calculating the fluxes entering and leaving the CEs. Unlike the traditional numerical methods which enforce flux conservation over a spatial domain, the CEs and SEs are used to enforce the flux conservation over any space-time domain in current numerical framework. From Figures 2.4 and 2.5, each CE is bound by surfaces belonging to SEs associated with two solution points, and these two

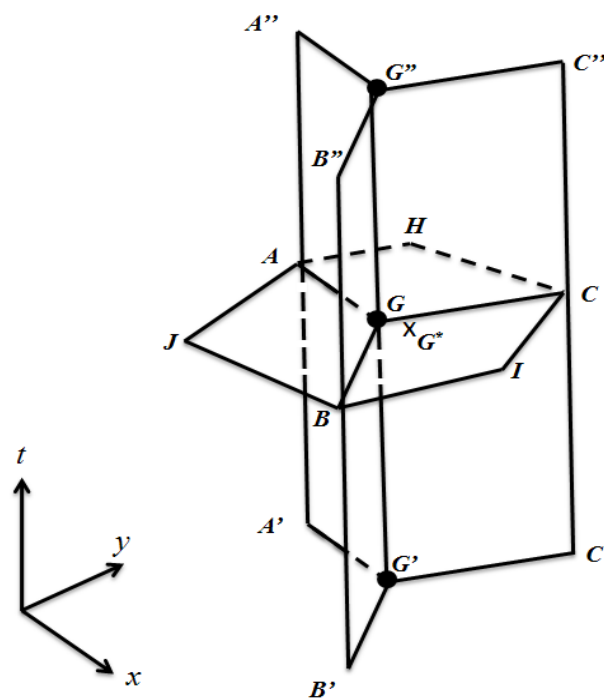


Figure 2.5 Definition of SE

solution points are at different time levels.

2.3.3 Properties of CEs and SEs

The construction of CEs does not rule out the possibility of having discontinuities in the flow variables within CEs. The integral form of the conservation laws has to be satisfied. Unlike CEs, the flow variables and the inviscid fluxes of SEs are assumed to be continuous and they are approximated by linear Taylor expansions. This assumption ensures that the SEs satisfy the differential form of the conservation laws. With flux conservation over both CEs and SEs, the solution is accurate even if the physics involve shocks or a high gradient region. Since the interface separating two neighboring CEs lies on only one SE, the flux leaving a particular CE through an interface and entering its neighboring CE through the same interface can be evaluated based on information from a single SE. The benefit of this construction is that, any interpolation or extrapolation is not needed for calculating fluxes at the interfaces. Another benefit is that it guarantees local and global flux conservation. Based on properties of SE defined above, the flux variables u_m , f_m and g_m can be approximated by $u_m^*(x,y,t)$, $f_m^*(x,y,t)$ and $g_m^*(x,y,t)$ as below:

$$u_m^*(x,y,t) = (u_m)_{G^*}^n + (u_{mx})_{G^*}^n (x - x_{G^*}) + (u_{my})_{G^*}^n (y - y_{G^*}) + (u_{mt})_{G^*}^n (t - t^n), \quad (2.21)$$

$$f_m^*(x,y,t)=(f_m^n)_{G^*}+\nabla((f_m^n)_{G^*})\cdot\mathbf{r}, \quad (2.22)$$

$$g_m^*(x,y,t)=(g_m^n)_{G^*}+\nabla((g_m^n)_{G^*})\cdot\mathbf{r}, \quad (2.23)$$

Here, $\mathbf{r} = (x-x_{G^*})\hat{\mathbf{i}}+(y-y_{G^*})\hat{\mathbf{j}}+(z-z_{G^*})\hat{\mathbf{k}}$ represents the position vector of point (x, y, z) in the E_3 space. The quantities x_{G^*} , y_{G^*} and z_{G^*} are the coordinates of solution point G^* . $(u_m)_{G^*}^n$ are the flow variables. $(u_{mx})_{G^*}^n$ and $(u_{my})_{G^*}^n$ are spatial derivatives. $(u_{mt})_{G^*}^n$ are the temporal derivatives. $(u_m)_{G^*}^n$, $(u_{mx})_{G^*}^n$, $(u_{my})_{G^*}^n$ and $(u_{mt})_{G^*}^n$ are all constants with the $SE(G^*,n)$. The viscous fluxes $f_{vm}(x,y,z)$ and $g_{vm}(x,y,z)$ are assumed to be constant within the SE and are approximated by $f_{vm}^*(x,y,z)$ and $g_{vm}^*(x,y,z)$. The definitions are:

$$f_{vm}(x,y,z) = f_{vm}^*(x,y,z), \quad (2.24)$$

$$g_{vm}(x,y,z) = g_{vm}^*(x,y,z). \quad (2.25)$$

The derivative of the inviscid fluxes can be expressed as:

$$(f_{mx})_{G^*}^n = \sum_{l=1}^4 (A_{ml})_{G^*}^n (u_{lx})_{G^*}^n, \quad (2.26)$$

$$(g_{my})_{G^*}^n = \sum_{t=1}^4 (B_{ml})_{G^*}^n (u_{ly})_{G^*}^n, \quad (2.27)$$

where $l, m = 1, 2, 3, 4$, and $(A_{ml})_{G^*}^n$ and $(B_{ml})_{G^*}^n$ are the elements of the Jacobian matrices of f_m and g_m calculated at the solution point (G^*, n) . On the other hand, $\mathbf{h}_m^*(x, y, t)$ is defined for the SE(G^*, n) and

$$\mathbf{h}_m^*(x, y, t) = (f_m^*(x, y, t) - f_{vm}^*(x, y, t), g_m^*(x, y, t) - g_{vm}^*(x, y, t), u_m^*(x, y, t)), \quad (2.28)$$

Within SE, $\mathbf{h}_m(x, y, t) = \mathbf{h}_m^*(x, y, t)$, which satisfies the differential form of the conservation laws. With the other assumption mentioned before:

$$(u_{mt})_{G^*}^n = -(f_{mx})_{G^*}^n - (g_{my})_{G^*}^n, \quad (2.29)$$

therefore twelve unknowns, i.e. u_m, u_{mx}, u_{my} , are required to be solved in CE/SE for two-dimensional problems. In conventional methods, only four unknowns, i.e. u_m , have to be solved.

2.3.4 Solution scheme

To solve for the unknowns, u_m, u_{mx}, u_{my} at solution point G^* at time level n , the equation, $\oint_{S(V)} \mathbf{h}_m \cdot d\vec{s} = 0$, is applied to the three CEs associated with solution point G^* , where the CEs are the space-time cylinders $AGBJA'G'B'J'$,

$AGCHA'G'C'H'$ and $CGBIC'G'B'I'$ (Figure 2.4). Using the properties of SE, the fluxes entering and leaving the interfaces are evaluated. In the process, the values of u_m , u_{mx} and u_{my} at solution points H'^* , I'^* and J'^* , which are all at the older time level $n-1/2$ are evaluated. So there are 12 equations and 12 unknowns at time level n , and it forms the non-dissipative scheme of the CE/SE framework.

2.3.5 Initial conditions

The far field ambient condition where flow velocity is assumed to be zero ($u_a = v_a = 0$) is applied to all solution points within the computational domain as the initial condition at the beginning of the calculations. The ambient density $\bar{\rho}_a$, temperature \bar{T}_a and pressure \bar{p}_a are non-dimensionalized as stated in Chapter 2.2, so the dimensionless ambient flow parameters become:

$$\rho_a = \frac{\bar{\rho}_a}{\bar{\rho}_{ref}} = 1, \quad (2.30)$$

$$T_a = \frac{\bar{T}_a}{\bar{T}_{ref}} = 1, \quad (2.31)$$

and the dimensionless ambient pressure can be worked out by using the equation of state for perfect gas (Equation (2.14)), so that:

$$p_a = \frac{\rho_a T_a}{\gamma} = \frac{1}{\gamma}. \quad (2.32)$$

2.3.6 Boundary conditions

Figure 2.6 shows the idea of ghost cells, which are the mirror images of the domain cells and these ghost cells are created outside the computational domain (on the other side of the edge of the domain boundary). In the CE/SE method, the boundary conditions are applied to the solution points of ghost

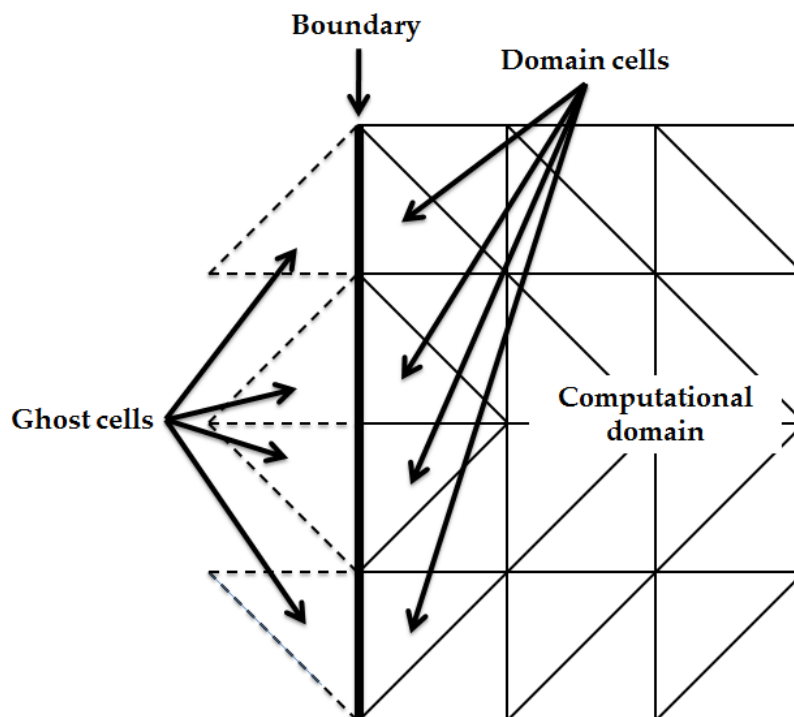


Figure 2.6 Definition of ghost cells at the boundary.

cells. The boundary conditions used in this study include the inlet condition, the no-slip adiabatic wall condition and the non-reflecting boundary condition (NRBC).

The no-slip adiabatic wall boundary condition always applied to all solid walls in the simulations including the nozzle walls and the substrate surface. The near wall approach introduced by Chang (2007) is employed. Since the cell size at the wall is small, so that the distance between the solution point of that boundary cell and the boundary practically approaches zero. Therefore, the flow variables at a ghost cell solution point can be expressed as:

$$\rho_{gc} = \rho_{ref}, \quad (2.33)$$

$$p_{gc} = p_{ref}, \quad (2.34)$$

$$u_{gc} = 0, \quad (2.35)$$

$$v_{gc} = 0. \quad (2.36)$$

The NRBC is applied to all the outflow boundaries of the simulations, where the solution vector $\mathbf{U}_{gc} = [\rho, \rho u, \rho v, \rho E]_{gc}^T$ and the spatial derivatives $(\mathbf{U}_x)_{gc}$ and $(\mathbf{U}_y)_{gc}$ at the ghost cells are expressed as:

$$\mathbf{U}_{gc} = \mathbf{U}_{b'} \quad (2.37)$$

$$(\mathbf{U}_x)_{gc} = (\mathbf{U}_x)_{b'} \quad (2.38)$$

$$(\mathbf{U}_y)_{gc} = (\mathbf{U}_y)_{b'} \quad (2.39)$$

where the subscript b denotes the boundary cells at the edge of the computational domain.

The inlet condition is applied to the nozzle inlet. With a given NPR, the inlet pressure p_{in} is defined,

$$p_{in} = \text{NPR} \cdot p_a = \text{NPR}/\gamma. \quad (2.40)$$

With given inlet gas temperature T_{in} of the supply gas, the inlet gas density ρ_{in} can be worked out by using the equation of state for perfect gas (Eqn. 2.14), so that:

$$\rho_{in} = \gamma p_{in}/T_{in} = NPR/T_{in}. \quad (2.41)$$

The streamwise inlet gas Mach number M_{in} can be found by the relationship between Mach number and area ratio (Eqn. 1.6) and thus the streamwise inlet gas velocity u_{in} can be determined from,

$$u_{in} = M_{in}/a_{in} = M_{in}/\sqrt{T_{in}}, \quad (2.42)$$

where the dimensionless speed of sound at the inlet is,

$$a_{in} = \sqrt{T_{in}}, \quad (2.43)$$

2.4 The particle models

Three models are developed for simulating the flight path of a particle, heat transfer between carrying gas and a particle, and the result of particle impact.

2.4.1 Particle flight model

Gas-particle interaction is also an important consideration in of CGDS process. Dykhuizen and Smith (1998) proposed an approximation of the dilute two-phase (gas + non-interacting particles) flow. The particle

acceleration $\frac{d\bar{\mathbf{V}}_p}{d\bar{t}}$ can be determined by the following dimensional equation of particle motion:

$$\bar{m}_p \frac{d\bar{\mathbf{V}}_p}{d\bar{t}} = \frac{C_D \pi \bar{d}_p^2 \bar{\rho}_p |\bar{\mathbf{V}}_g - \bar{\mathbf{V}}_p|^2}{8}, \quad (2.44)$$

where \bar{m}_p , $\bar{\rho}_p$ and \bar{d}_p are the mass, density and diameter of particles respectively, $\bar{\mathbf{V}}_g$ and $\bar{\mathbf{V}}_p$ is the velocity vector of the carrier gas and particle.

The particle Reynolds number ($Re_p = \bar{\rho} |\bar{\mathbf{V}}_g - \bar{\mathbf{V}}_p| \bar{d}_p / \bar{\mu}$) and particle Mach number ($M_p = |\bar{\mathbf{V}}_g - \bar{\mathbf{V}}_p| / \bar{a}_{ref}$) for CGDS processes are typically within the ranges of $0.2 < Re_p < 10^4$ and $0.1 < M_p < 2$, except the small region near the particle injection location and therefore the drag coefficient of particle C_D within this conditions can be expressed by the following empirical relationship (Crowe 1967):

$$C_D = \frac{24}{Re} \left[\frac{(1 + 0.15 Re_p^{0.687}) \left(1 + e^{-0.427 / M_p^{4.63 + 3.0 / Re_p^{0.88}}} \right)}{1 + \left(M_p / Re_p \right) \left(3.82 + 1.28 e^{-1.25 Re_p / M_p} \right)} \right]. \quad (2.45)$$

Normalizing Equation (2.44) with the same length scale \bar{L}_{ref} , density scale $\bar{\rho}_{ref}$, mass scale $\bar{\rho}_{ref} \bar{L}_{ref}^3$, velocity scale \bar{a}_{ref} and time scale $\bar{L}_{ref} / \bar{a}_{ref}$, and the normalized form of the equation of particle motion expression becomes:

$$m_p \frac{d\mathbf{V}_p}{dt} = \frac{C_D \pi d_p^2 \rho_p |\mathbf{V}_g - \mathbf{V}_p|^2}{8}. \quad (2.46)$$

By using Equations (2.45) and (2.46) with a particle initially at location $(x_{p,i}, y_{p,i})$ and gas flow velocity \mathbf{V}_g at the solution point closest to the particle, acceleration $\frac{d\mathbf{V}_p}{dt}$ of that particle can be readily found. At a time instant i , the particle located at $(x_{p,i}, y_{p,i})$ with velocity $\mathbf{V}_p = (u_{p,i}\vec{i} + v_{p,i}\vec{j})$ the coordinates and the velocity of that particle after a time step Δt become,

$$x_{p,i+1} = x_{p,i} + u_{p,i}\Delta t + \frac{1}{2} \frac{du_{p,i}}{dt} (\Delta t)^2, \quad (2.47)$$

$$y_{p,i+1} = y_{p,i} + v_{p,i}\Delta t + \frac{1}{2} \frac{dv_{p,i}}{dt} (\Delta t)^2, \quad (2.48)$$

$$u_{p,i+1} = u_{p,i} + \frac{du_{p,i}}{dt} (\Delta t), \quad (2.49)$$

$$v_{p,i+1} = v_{p,i} + \frac{dv_{p,i}}{dt} (\Delta t). \quad (2.50)$$

The flight path of each particle can be obtained by iterating this flight model through all time steps. The particle is assumed to be stationary at the instant just before injection, so the initial particle velocity $u_{p,i=0} = v_{p,i=0} = 0$.

2.4.2 Particle impact model

When a particle impinges on the substrate surface, deposition occurs if the impact velocity is higher than the critical velocity \bar{V}_c ; otherwise the particle will bounce off. A particle impact model is thus developed by assuming perfectly elastic collision between the particle and the substrate in which

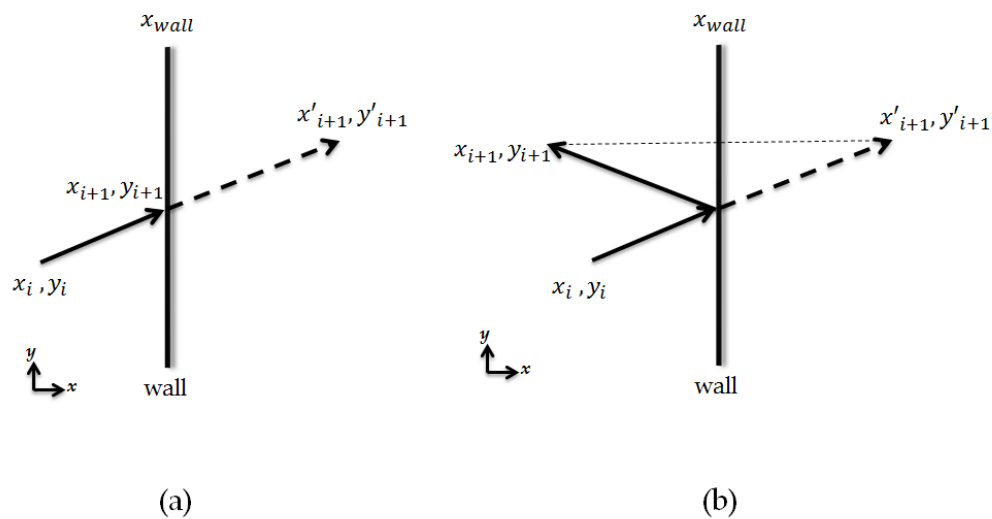


Figure 2.7 Particle impact model: (a) Successful deposition; (b) particle bounces off.

both the substrate surface and the particle are assumed to be rigid during impact. Figure (2.7a) shows the result of deposition when particle impact velocity is higher than \bar{V}_c . The location of the particle after impact is approximated as,

$$x_{p,i+1} = x_{wall} , \quad (2.51)$$

$$y_{p,i+1} = \frac{x_{wall} - x_{p,i}}{x'_{p,i+1} - x_{p,i}} (y'_{p,i+1} - y_{p,i}) + y_{p,i} , \quad (2.52)$$

where $(x_{p,i}, y_{p,i})$ is the particle location before impact and $(x'_{p,i+1}, y'_{p,i+1})$ is the particle location estimated by the particle flight model (Eqs. 2.47 – 2.50) without considering the presence of the vertical wall. If the impact velocity is lower than the critical velocity, the particle bounces off as shown in Figure 2.7b. Since the bounce-off particles are not the main concern of this project, their impact are just simply assumed to be rigid collision, and the location and velocity of particle after impact are found from,

$$x_{p,i+1} = x_{wall} - (x'_{p,i+1} - x_{wall}) , \quad (2.53)$$

$$y_{p,i+1} = y'_{p,i+1} , \quad (2.54)$$

and the horizontal and vertical components of the velocity vector of the particle after impact are given by Equations (2.55) and (2.56) respectively, i.e.

$$u_{p,i+1} = -u_{p,i} , \quad (2.55)$$

$$v_{p,i+1} = v_{p,i} , \quad (2.56)$$

where u_i and v_i are the horizontal and vertical components of the particle velocity vector before impact. Equations (2.55) and (2.56) show that there is no kinetic energy loss during the impact and the particle travels at the same speed after impact.

2.4.3 Particle heat transfer model

The impact temperature \bar{T}_i is an important parameter in Equation (1.1). It plays a role in defining the critical impact velocity for successful deposition of particles. Therefore the heat transfer between particles and the carrier gas has to be considered. In the CGDS process, the temperature of the carrier gas is higher than the coating particle so heat is transferred from surrounding gas to the particle by convection. The heat transfer rate is related to the temperature difference between carrier gas and particles, dimensions of particles, gas conductivity, etc., and it can be determined by the following expression:

$$\bar{c}_p \frac{d\bar{T}_p}{d\bar{t}} = \left(\frac{N_u \bar{k}}{\bar{d}_p} \right) \left(\frac{\bar{A}_p}{\bar{m}_p} \right) (\bar{T}_g - \bar{T}_p) , \quad (2.57)$$

where \bar{c}_p is the specific heat with constant pressure of a particle, \bar{T}_g and \bar{T}_p

are the gas and particle temperature, \bar{d}_p and \bar{A}_p are the diameter and surface area of a particle, \bar{k} is the gas thermal conductivity, and the Nusselt number N_u is the ratio of convective heat transfer to conductive heat transfer across a boundary. In CGDS process the expression of N_u is given by Ranz and Marshall (1952) is adapted in the present study which is a function of the particle Reynolds number Re_p and the Prandtl number Pr :

$$N_u = 2.0 + Re_p^{0.5} Pr^{0.33} , \quad (2.58)$$

$$Pr = \frac{\bar{c}_p \bar{\mu}}{\bar{k}} , \quad (2.59)$$

where Re_p is the particle Reynolds number, Pr is the Prandtl number and \bar{k} is the thermal conductivity. The normalized form of Equation (2.57) shows:

$$\frac{dT_p}{dt} = \left(\frac{N_u}{Pr Re_p} \right) \left(\frac{\mu A_p}{d_p m_p} \right) (T_g - T_p) \quad (2.60)$$

Similar to the particle flight model, the temperature value of each particle is also updated every iteration, so that the temperature after one time step can be expressed as:

$$T_{p,i+1} = T_{p,i} + \frac{dT_p}{dt} (\Delta t) \quad (2.61)$$

2.5 Conclusions

In this chapter, the governing equations of CGDS flow and particles it carries are both discussed including the particle flight model, the impact model and the heat transfer model. The governing equations of flow are the ideal gas equation of state and the N-S equations which state the principle of conservation of mass, momentum and energy. A numerical method called CE/SE was developed based on the non-dimensional form of the Navier-Stokes equations, and used to solve the flow problem. Although the CGDS process is highly steady within the nozzle and impinging zone, it is still worth to use this unsteady solver to simulate this process so that the unsteady flow and particle information far away from the nozzle can still be captured. This numerical method is validated and discussed in the next chapter.

3. Validation of the Flow Solver

As mentioned in previous chapters, simulation of the CGDS gas dynamics is carried out before the particle models are applied to the numerical results. The particles are essentially treated as passive scalars following the flow. The numerical solver based on the CE/SE method is used to simulate the CGDS flow, and this solver is originally developed to solve subsonic aeroacoustic problems (Lam *et al.* 2008). Therefore, it is necessary to establish and validate the capability of the CE/SE solver in simulating supersonic impinging jet flow which may carry shock waves. Since the aspect ratio of the cross section of the rectangular nozzle used in the simulations is high, so that the two-dimensional CE/SE solver can be used for validation tasks, such as simulations of free supersonic jet issuing from a convergent-divergent nozzle operating at both design and off design pressure ratios, and simulations of selected supersonic impinging jet benchmark problems. Some key features such as shock cells at the nozzle exit of free supersonic jet problem, lambda shock system inside the overexpanded nozzle, stand-off shock in the impinging zone of the imping jet problem etc., are compared to existing experimental and numerical data to show the capability of the CE/SE solver in simulating the CGDS flow problem.

3.1 Supersonic free jet from an underexpanded nozzle

The gas dynamics inside a C-D nozzle are involved in the CGDS process because both the carrying gas and particle are accelerated there. Therefore an assessment of the capability of the CE/SE solver to simulate this problem is necessary.

The NASA Langley Research Centre carried out a number of research projects on the gas dynamics of supersonic nozzle flow (Hunter 1998, 2004). A detailed experimental study of separated nozzle flow was conducted using a wind tunnel (Hunter 2004). In this experimental study, a C-D test nozzle is used (Figure 3.1) with throat area $\bar{A}_{th} = 4.317 \text{ in}^2$, an

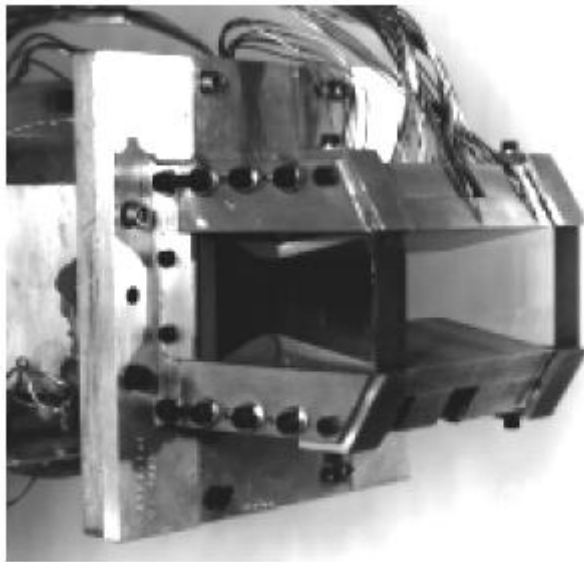


Figure 3.1 Test convergent divergent nozzle in the NASA Langley Research Centre (Hunter 2004).

expansion ratio $\bar{A}_e/\bar{A}_{th} = 1.797$ and a constant width of 3.99 in. It should be noted that a numerical simulation for comparison was also conducted by Hunter (1998) using a two-dimensional steady state CFD code PAB3D and its results agree well with the experimental data. To validate the CE/SE solver, the result of the numerical simulation including numerical schlieren images which shows the magnitude of density gradient, pressure variation, exit Mach number, etc. are compared to theory and existing data.

3.1.1 Numerical setup

The test nozzle used in Hunter's (2004) experiment was an approximate two-dimensional C-D nozzle. In the experiment, compressed air with high nozzle pressure ratio (NPR = 9) was supplied to the nozzle inlet at a temperature of about 295K. Figure 3.2 shows a schematic sketch of the two-dimensional computational domain for CE/SE simulation. The dimensions are normalized using the width of the nozzle exit. The computational domain covers only the upper half of the nozzle and the surrounding ambient region. A large buffer zone surrounding the physical domain is created and the boundary conditions are applied at the outer edge of the buffer zone. The buffer zone is a domain located between the physical domain and the outflow boundary, in which the elements size increases so

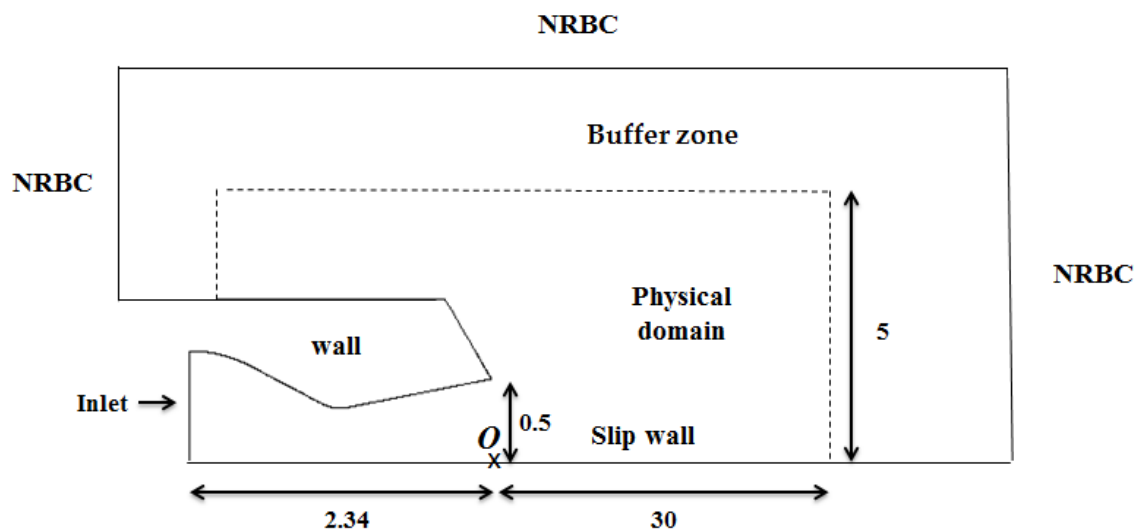
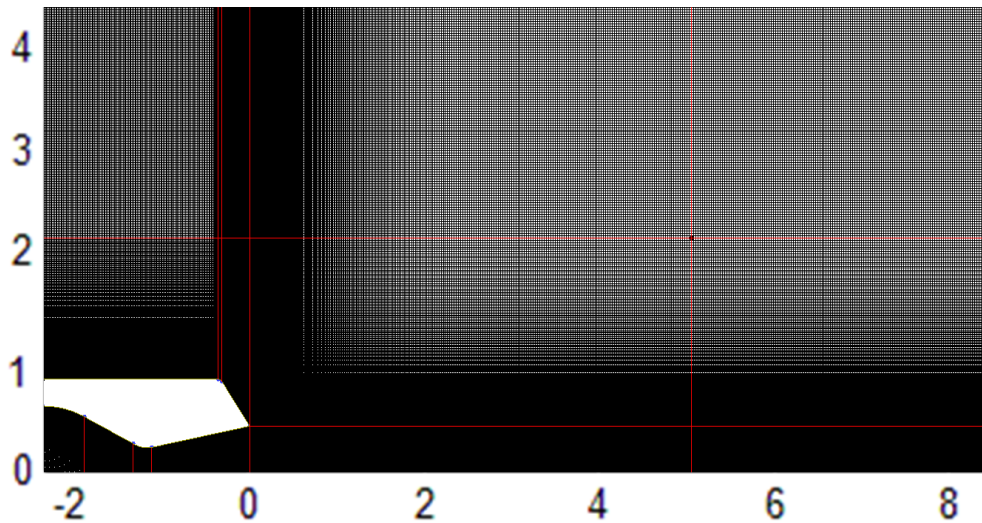


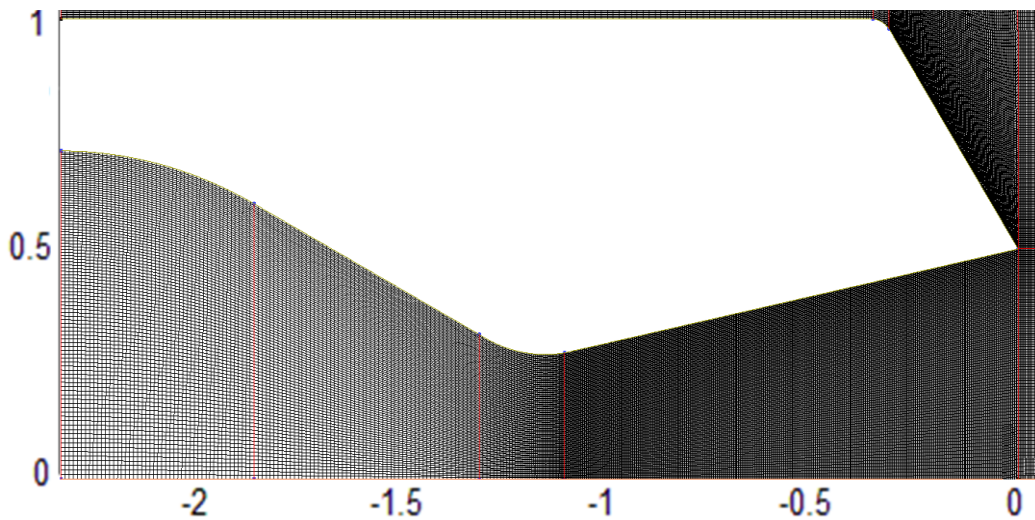
Figure 4.2 Computational domain.

that flow information is dissipated before reaching the outflow boundary. Therefore all flow disturbances can only leave outflow boundaries without any reflection, and the simulation accuracy can be enhanced by preventing contamination of flow results from reflection of disturbance. Non-reflecting boundary conditions (NRBC) are applied at the domain edges as outflow boundary and no-slip adiabatic wall boundary conditions are applied at all solid walls. The lower symmetry edge of the computational domain is treated as a slip wall. Inlet boundary conditions, which are discussed in Chapter 2.3.5, are applied to the nozzle inlet where inlet pressure $p_{in} = \text{NPR}/\gamma = 6.43$, inlet temperature $T_{in} = 1$ and $\rho_{in} = \text{NPR}/T_{in} = 9$. The inlet

streamwise velocity $u_{in} = M_{in}\sqrt{T_{in}} = 0.247$. The initial conditions within the whole computational domain are defined as ambient conditions as discussed in Chapter 2.3.4, so that $p = 1/\gamma$, $T = 1$, $\rho = 1$ and $u = v = 0$.



(a)

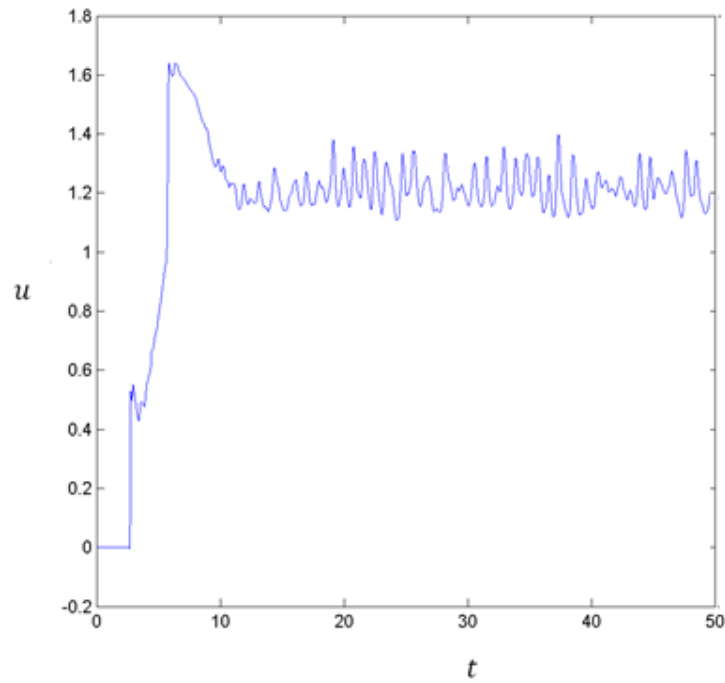


(b)

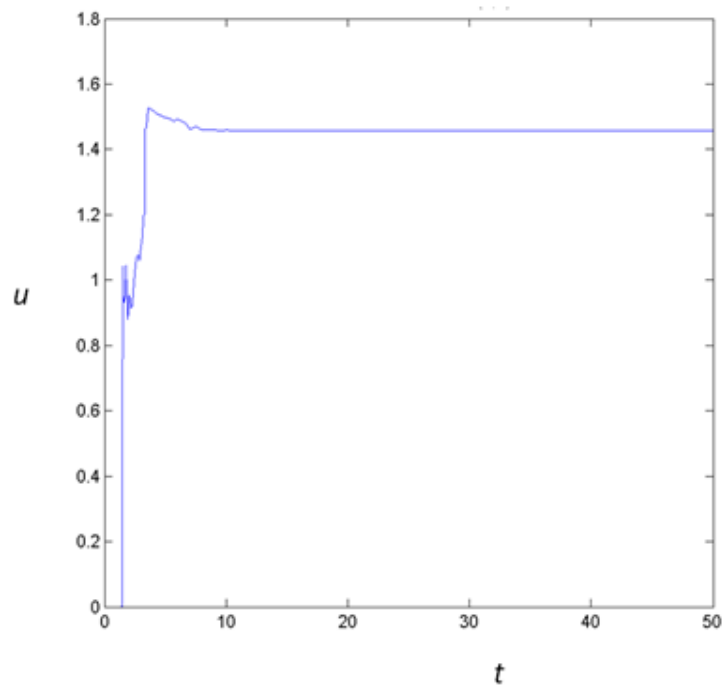
Figure 3.3 Mesh design: (a) Overall domain; (b) inside the nozzle.

The Reynolds number at to nozzle throat the simulation is 1×10^6 , and the time step size Δt is 8×10^{-5} . The computational domain (Figure 3.3) and is filled up by about 0.8 million triangular meshes and the meshing code used to generate the mesh is ICEM CFD. The calculation took about 250,000

time steps to obtain a time-stationary solution. Figure 3.4 shows the time traces of velocity u at locations $(-0.6, 0)$ and $(2, 0)$.



(a)



(b)

Figure 3.4 Temporal variations of streamwise velocity u at (a) $(2, 0)$ and (b) $(-0.6, 0)$.

3.1.2 Results and discussions

In this section, the CE/SE numerical results are compared to existing data to assess the capability of the CE/SE solver in simulating supersonic nozzle flow.

Table 3.1 shows the comparison of CE/SE results to the 1D isentropic relationship, and Hunter's experimental and numerical results. The CE/SE results shown are the averaged Mach number along the cross-sections of the nozzle exit. With given exit area ratio $\bar{A}_e/\bar{A}_{th} = 1.797$, the theoretical value of Mach number can be found by using Equation 1.6 and Figure 1.3; therefore the theoretical value of exit density ratio and exit pressure ratio can be found by using isentropic relationships (Eqs. 1.8 and 1.9): the difference is about 4%, so the results of CE/SE simulation match the theory very well, and also matches Hunter's experimental and numerical results well.

| | CE/SE | 1D isentropic relationship | Hunter's Experiment | Hunter's CFD |
|-------------------------------------|-------|----------------------------|---------------------|--------------|
| Exit density ratio, ρ_e/ρ_0 | 0.217 | 0.211 | / | / |
| Exit pressure ratio, p_e/p_0 | 0.119 | 0.114 | ~0.1 | ~0.1 |
| Exit Mach number, M_e | 2.07 | 2.08 | / | / |

Table 3.1 Flow variables at the nozzle exit.

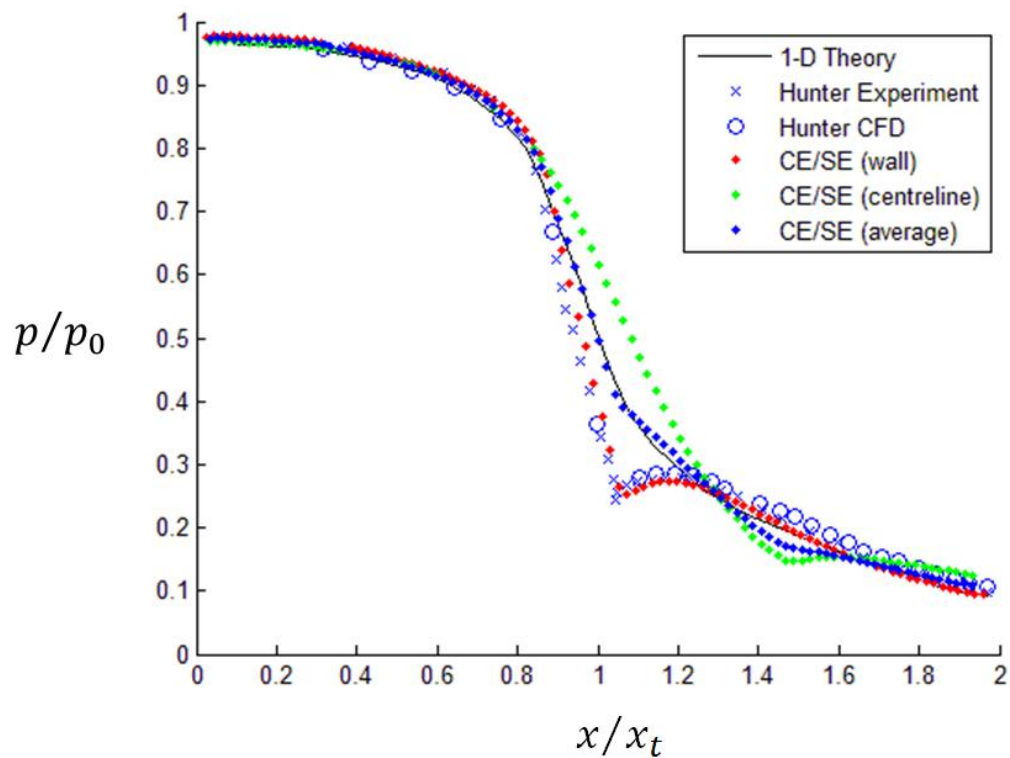


Figure 3.5 Pressure variations along the nozzle.

Figure 3.5 shows the pressure variations along the upper nozzle wall, centerline and averaged value. The CE/SE solver is able to obtain similar results on the upper nozzle wall comparing to existing experimental and numerical data. The averaged results also match the 1-D isentropic relationships. Figures 3.6 and 3.7 show the schlieren image ($|\nabla\rho|$) of Hunter's experiment and CFD at the divergent zone of the nozzle respectively. Figure 3.8 shows the numerical schlieren image of the CE/SE simulation. By comparing the shape and location of the expansion waves, the CE/SE solver gives good simulation results again that agree with Hunter's work.

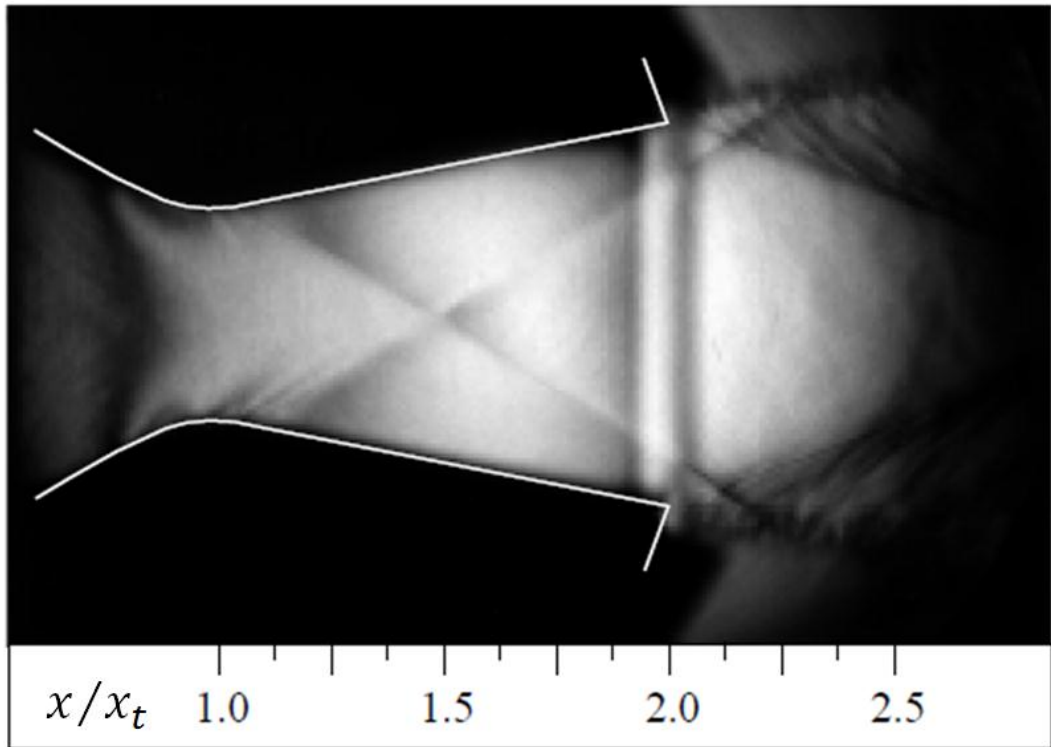


Figure 3.6 Schlieren image taken in the experiment: Hunter (1998)

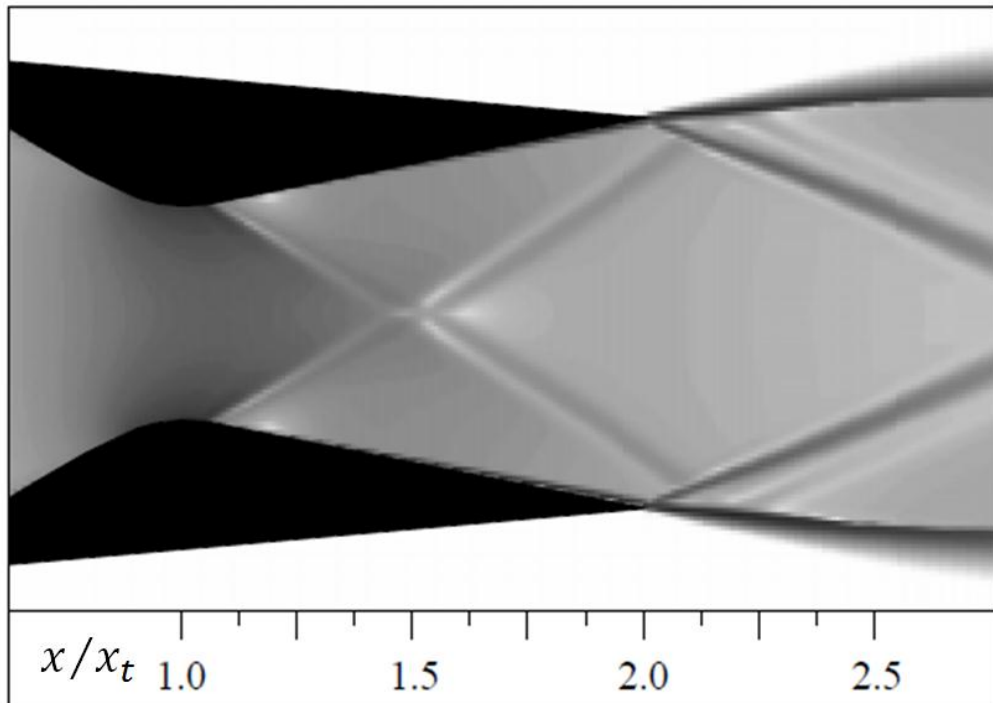


Figure 3.7 Numerical schlieren image of CFD simulation: Hunter (1998)

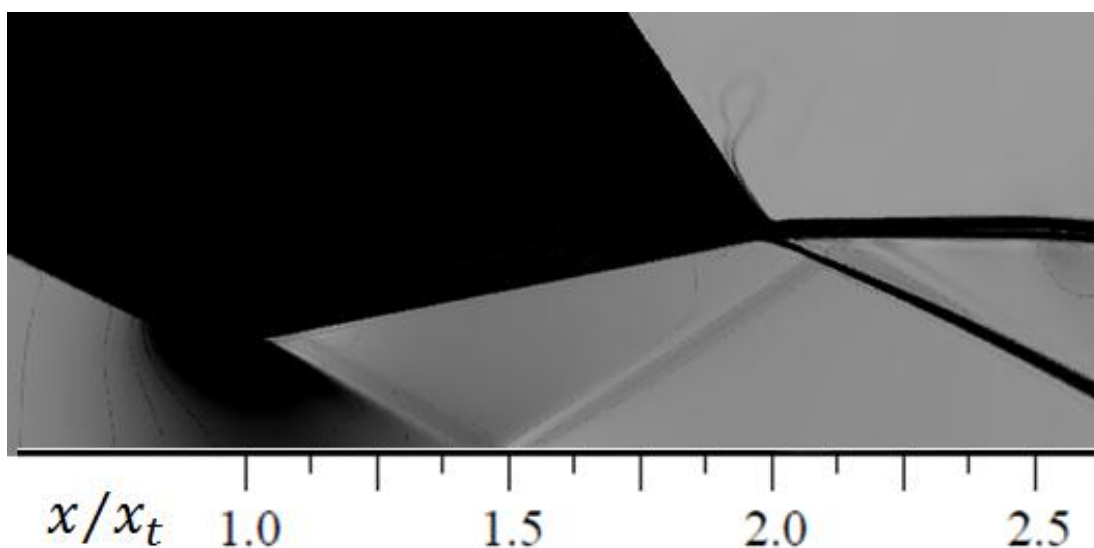


Figure 3.8 Schlieren image of CE/SE simulation, showing the density gradient magnitude $\nabla|\rho|$ of the flow at the divergent section of the nozzle.

It can be concluded that the CE/SE solver is capable of solving the internal and external flows of a supersonic nozzle when it is operating under design conditions or underexpanded conditions. Therefore it can prove that the CE/SE solver is also able to simulate the gas flow inside the CGDS nozzle accurately.

3.2 Supersonic free jet with an overexpanded nozzle

Apart from underexpanded nozzle, simulation of an overexpanded nozzle is also performed to validate the CE/SE solver. The results of existing experiments (Hunter 1993) show the appearance of shock-boundary layer interaction. Figure 3.9 is a schematic of the internal flow of an overexpanded

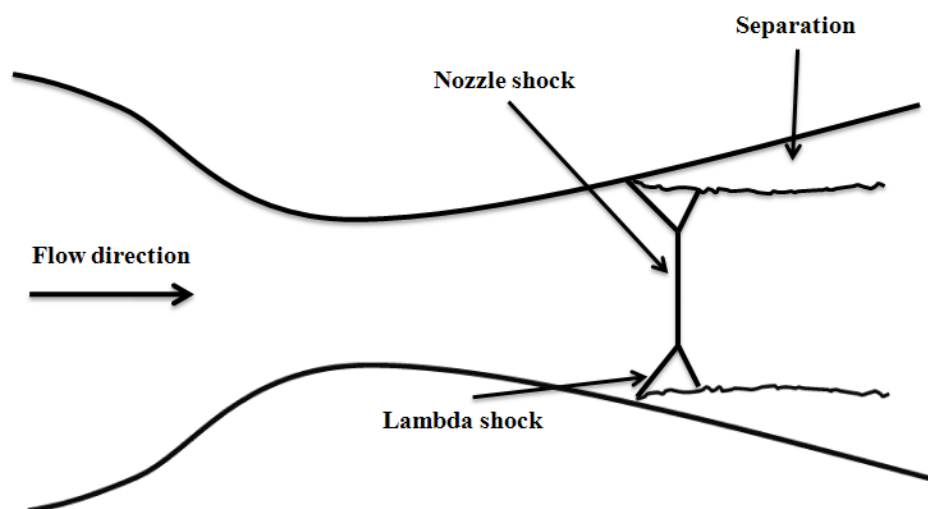


Figure 3.9 Internal lambda shock system in an overexpanded convergent-divergent nozzle.

CD nozzle: a nozzle shock with lambda shock system appears downstream of the nozzle throat and there is a fully detached separation extending from the leading lambda shock. These features occur because the nozzle expansion ratio is too large for a given NPR. A fully detached region imposes stronger turning requirements on the internal nozzle flow than a closed separation bubble. The results of the CE/SE simulation including numerical schlieren images, pressure variation, etc. are compared to existing data to access the capability of the CE/SE solver in such problem.

3.2.1 Numerical setup

The test nozzle used in the experiment is a two-dimensional C-D nozzle which is the same nozzle studied in Chapter 3.1. High pressure air with $NPR=2.4$ is supplied to the nozzle inlet at a stagnation temperature of about 295K. Figure 3.10 shows the details and boundary conditions of the two-dimensional computational domain of the CE/SE simulation. The dimensions are normalized using the length between nozzle inlet and nozzle throat, and the surrounding ambient region extends 30 units downstream

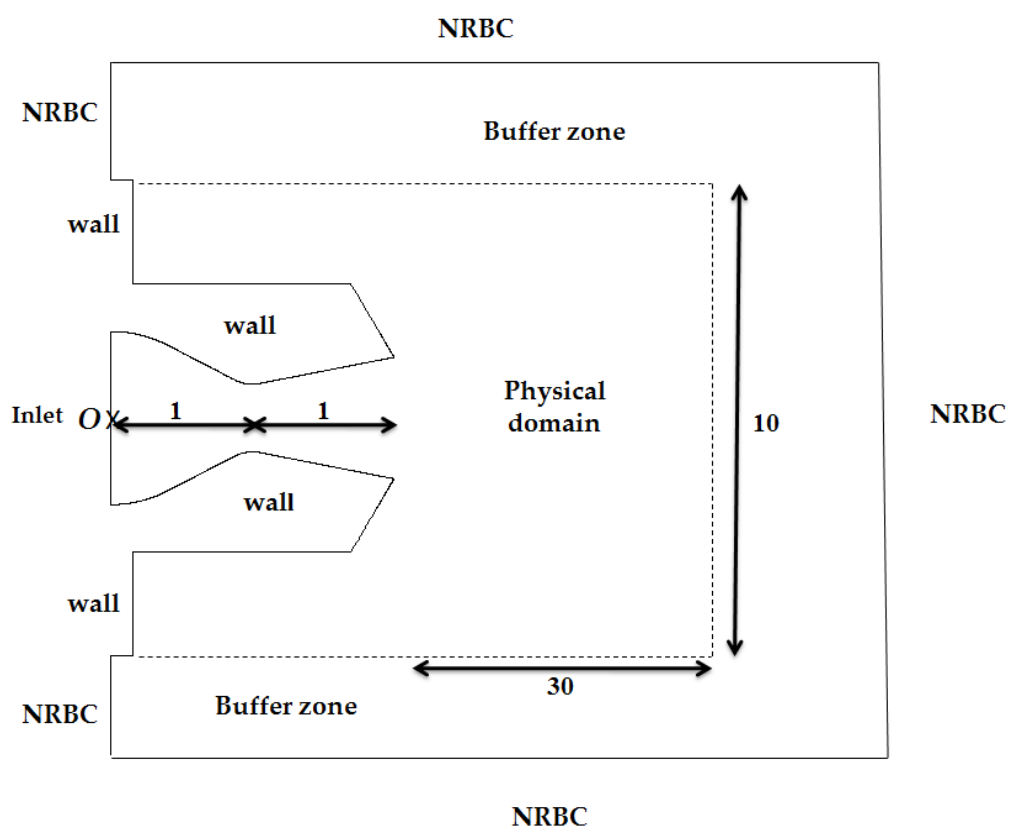


Figure 3.10 Computational domain of supersonic jet simulation with an overexpanded nozzle.

and 5 units normal to the jet axis. A large buffer zone is created surrounding the physical domain and the boundary conditions are applied at the outer edge of the buffer zone. Non-reflecting boundary conditions (NRBC) are applied at the domain edges as outflow boundary and no-slip adiabatic wall boundary conditions are applied at all solid walls. Inlet boundary conditions as discussed in Chapter 2.3.5, are applied to the nozzle inlet where inlet pressure $p_{in} = NPR/\gamma = 1.71$, inlet temperature $T_{in} = 1$ and $\rho_{in} = NPR/T_{in} = 2.4$. The inlet streamwise velocity $u_{in} = M_{in}\sqrt{T_{in}} = 0.247$. The initial conditions within the whole computational domain are defined as ambient conditions as discussed in Chapter 2.3.4, so that $p = 1/\gamma$, $T = 1$, $\rho = 1$ and $u = v = 0$.

The Reynolds number Re of the simulation is 1.1×10^6 , and the time step size Δt is 5×10^{-4} . The whole computational domain is filled up by about 2.4 million triangular meshes. The calculation took about 180,000 time steps to obtain a time stationary solution.

3.2.2 Results and discussions

Figures 3.11 and 3.12 show clearly the schlieren image of the lambda shock system of Hunter's experiment and simulation. The normal shock on the centreline and lambda foot on the nozzle wall are located at $x/x_t \approx 1.7$ and

$x/x_t \approx 1.5$ respectively. Figure 3.13 is the numerical schlieren image of the CE/SE simulation, which is created by plotting the density gradient magnitude $\nabla|\rho|$ of the time averaged solution. The comparison of different lambda shock location and shock structure are shown in Figure 3.14 and Figure 3.15. The lambda shock structure of CE/SE simulation done by Hunter, with the normal shock on the centreline and lambda foot on the nozzle wall are located at $x/x_t \approx 1.5$ and $x/x_t \approx 1.2$ respectively. The flow separates from the nozzle wall downstream of the lambda foot; therefore the separation point of CE/SE simulation is located more upstream than the existing data. The vertical normal of CE/SE simulation is shorter by comparison. More detailed comparisons of shock structure and Mach number across the shock are shown in Figure 3.15.

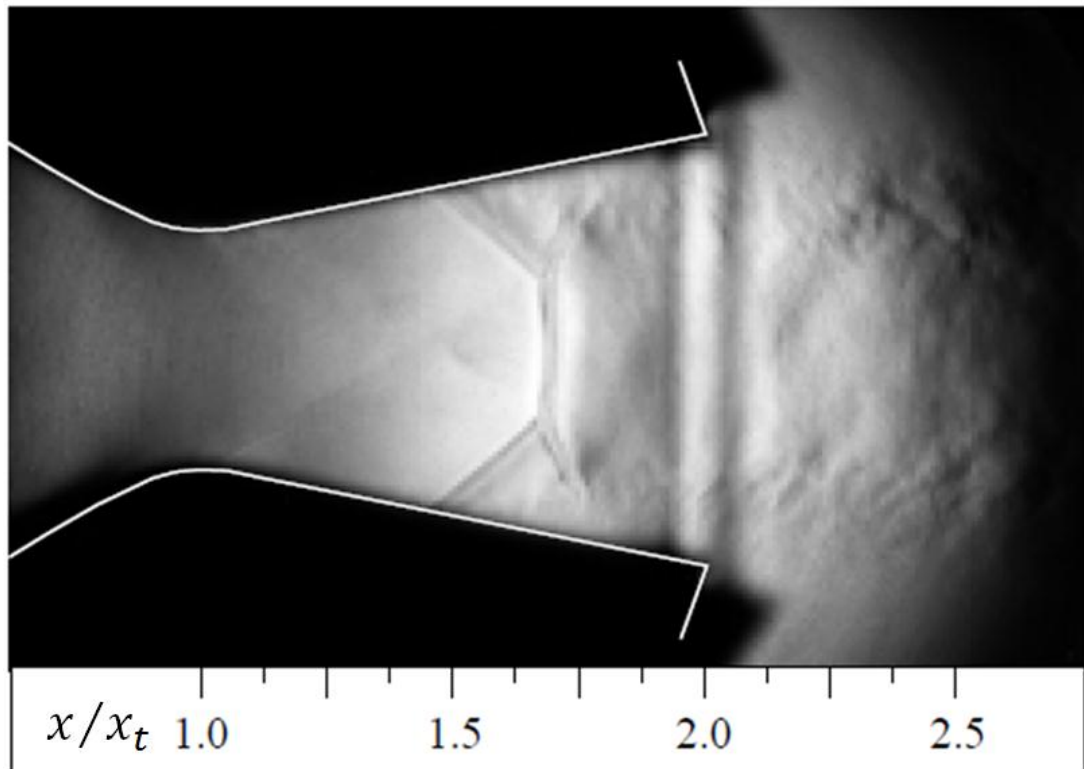


Figure 3.11 Schlieren image taken in the experiment: Hunter (1998)

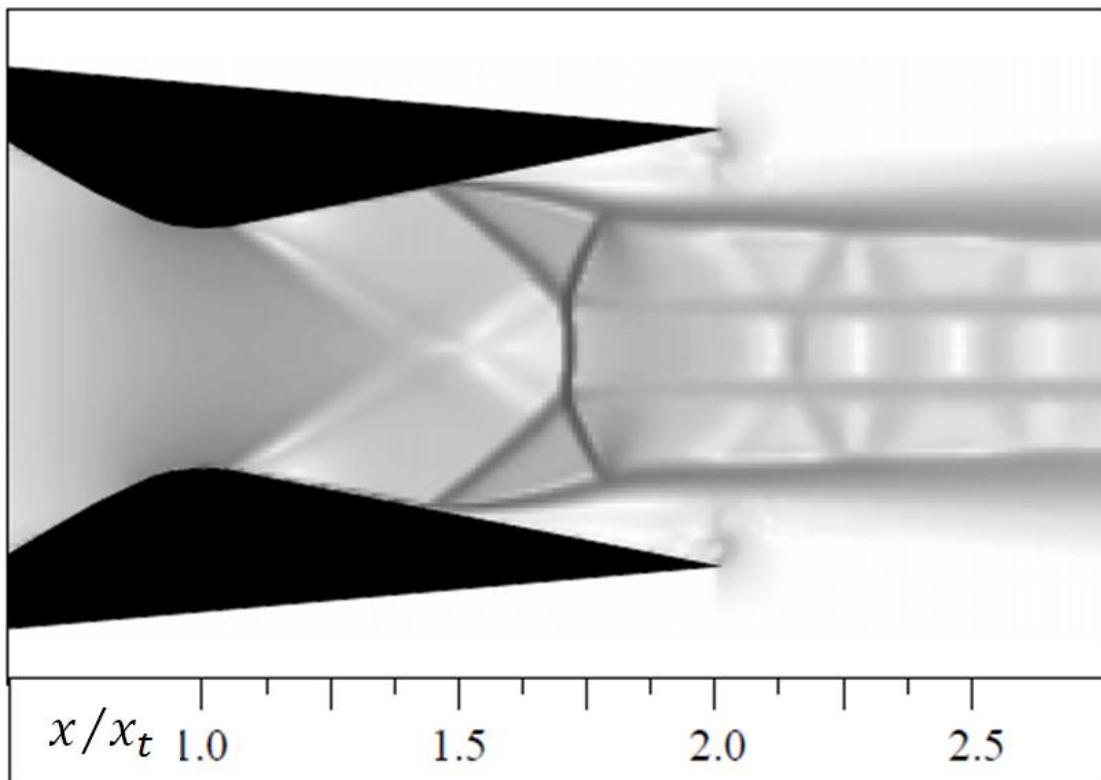


Figure 3.12 Numerical schlieren image of CFD simulation: Hunter (1998).

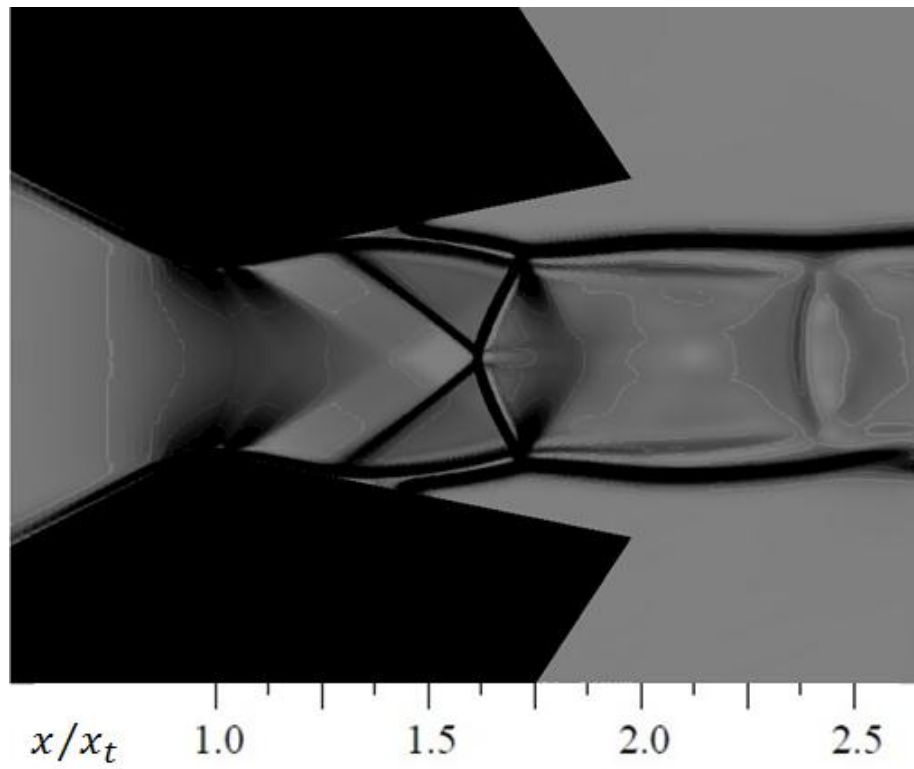


Figure 3.13 Schlieren image of CE/SE simulation, showing the density gradient magnitude $\nabla|\rho|$ of the flow at the divergent zone of the nozzle.

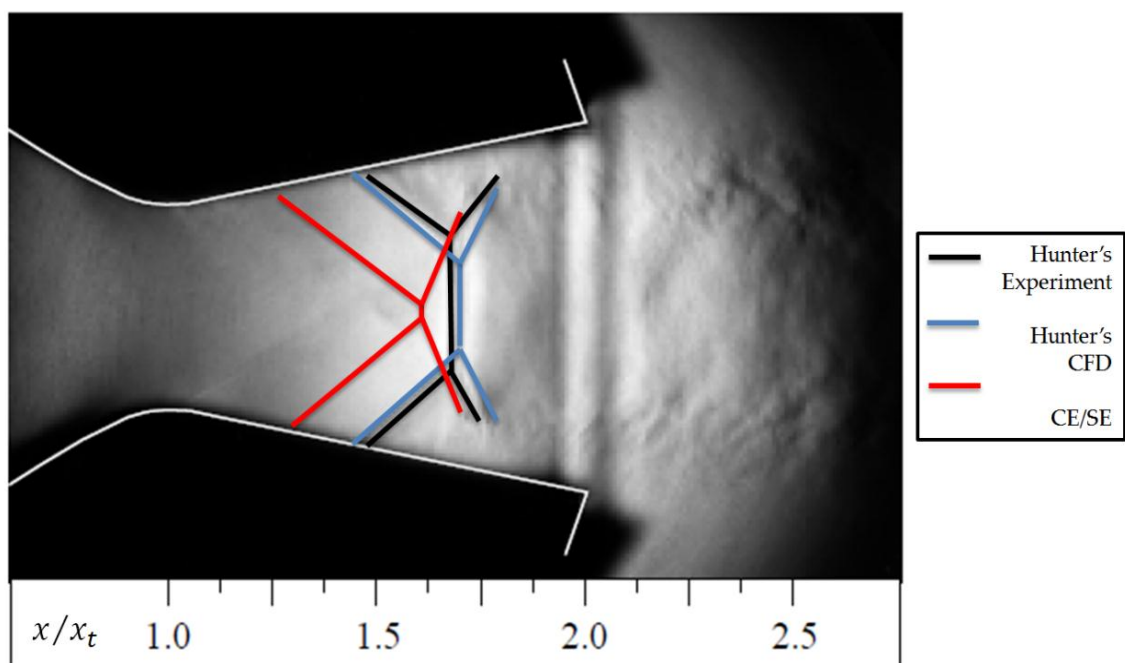


Figure 3.14 Shock location comparison.

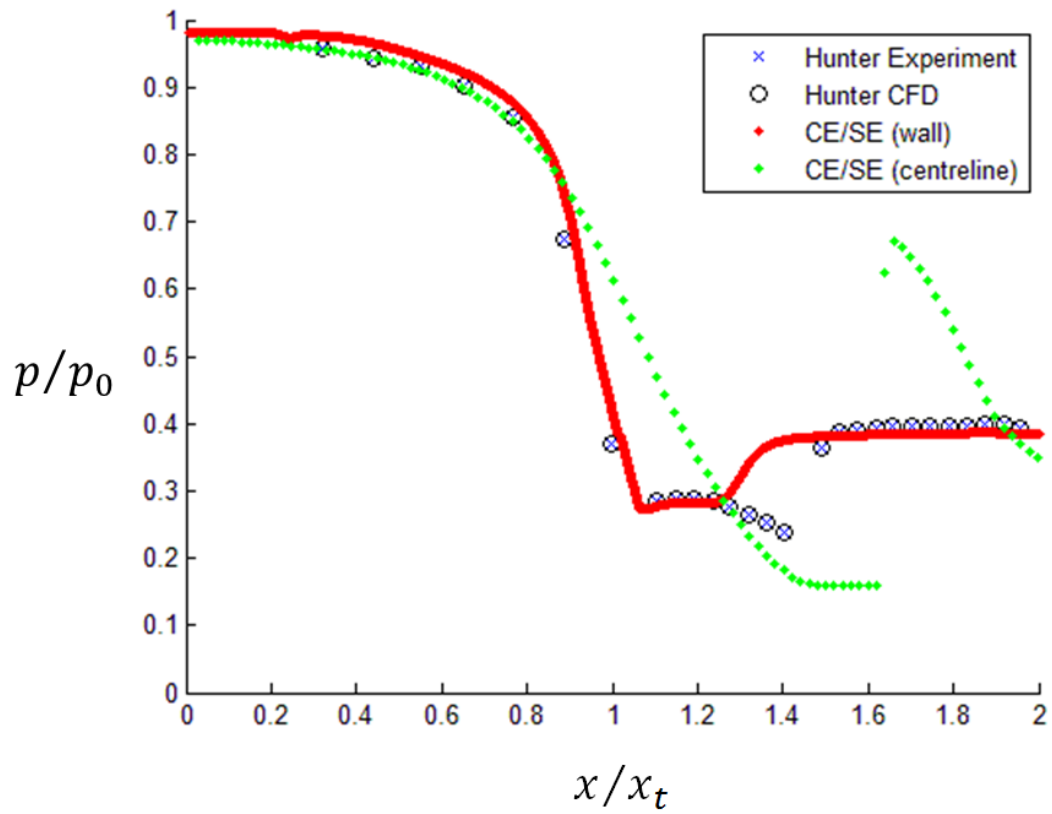


Figure 3.16 Pressure variations along the overexpanded nozzle.

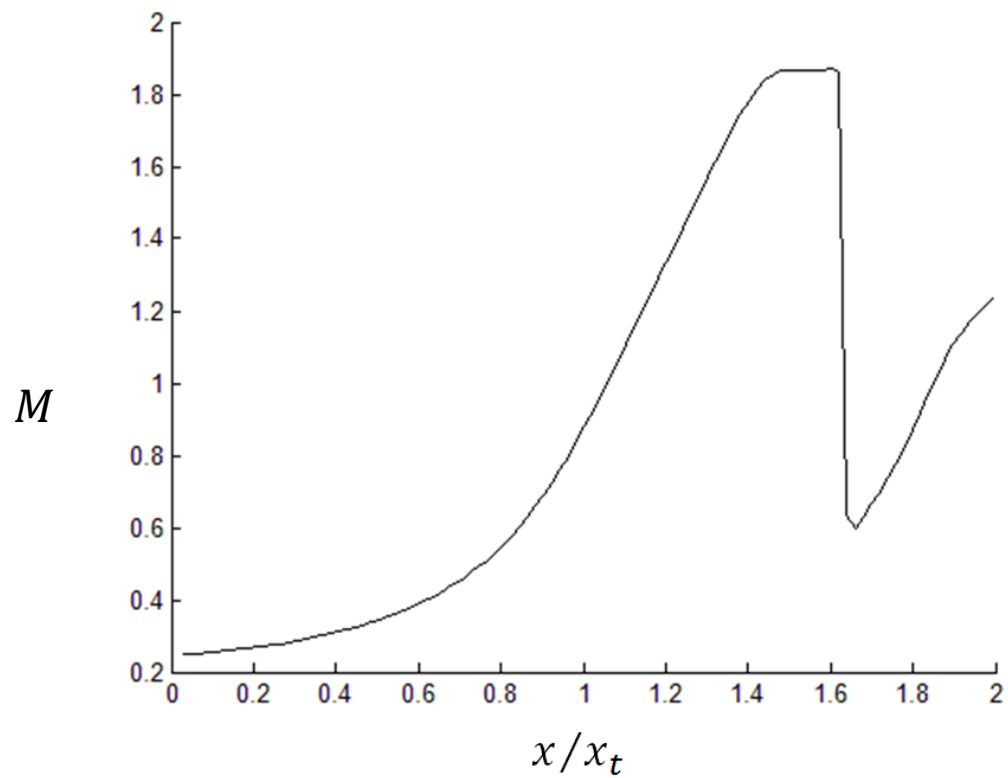


Figure 3.17 Mach number variations along the overexpanded nozzle.

the corresponding downstream Mach number M_2 is 0.601. Therefore the Mach number change across the normal shock simulated by the CE/SE solver also agreed with the normal shock relationship. On the other hand, the Mach number at the centerline at the nozzle throat is slightly less than one, it is the difference between 1D theory and 2D simulation.

3.3 Supersonic impinging jet from a straight duct

The modelling of free supersonic jet impingement on a flat solid surface is important for understanding the dynamics of CGDS flow. In order to validate our CE/SE framework for the two-dimensional supersonic jet impingement problem, the experiment done by Krothapalli (1985) is repeated. In this experiment, a converging nozzle with a rectangular exit is connected to a 40mm long straight smooth rectangular channel. The dimensions of the rectangular exit of both nozzle and channel are 50mm by 3mm with this aspect ratio; the problem can be assumed to be essentially two-dimensional. A 20mm x 20mm flat plate is placed 63mm from the channel exit to provide a large impinging surface for the jet. The controlling parameter of the jet is nozzle pressure ratio NPR = 4.81.

applied at the domain edges as outflow boundary and no-slip adiabatic wall boundary conditions are applied at all solid walls. The inlet of the straight duct is also the exit of the convergent nozzle which is not shown in the computational domain. Therefore the inlet condition at the duct inlet is the nozzle throat conditions. Assuming the Mach number $M_{in} = 1$ at the inlet of the straight duct, so that the actual $NPR = 2.54$, $p_{in} = NPR/\gamma = 1.814$, $T_{in} = 0.833$, $\rho_{in} = NPR/T_{in} = 3.04$ and the inlet streamwise velocity $u_{in} = M_{in}\sqrt{T_{in}} = 0.912$ where the initial conditions within the whole computational domain are defined as ambient conditions which was discussed in Chapter 2.3.4, so that $p = 1/\gamma$, $T = 1$, $\rho = 1$ and $u = v = 0$.

3.3.2 Results and discussions

After four million time steps of calculation, the gas dynamic features at an instant in the impinging zone are shown in Figure 3.19, which is compared to the schlieren photograph (Figure 3.20) taken in the experiment (Krothapalli 1985). Both numerical and experimental results show the appearance of shock cells in the main jet region, and the size and location of the impinging area is very similar. The unsteadiness shown are caused by the oscillation of jet. The figure shows that there are some waves generated at the shock cell and some waves are then reflected by the substrate.

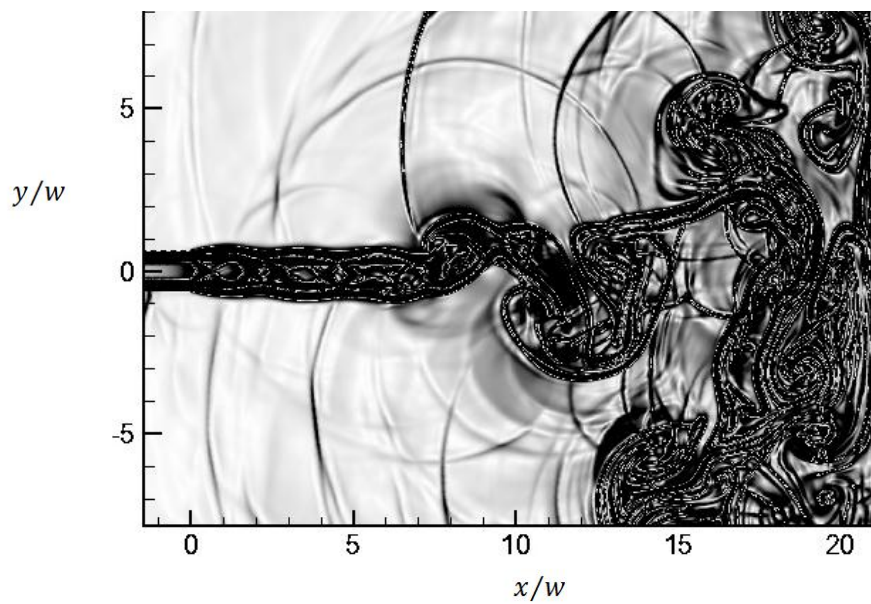
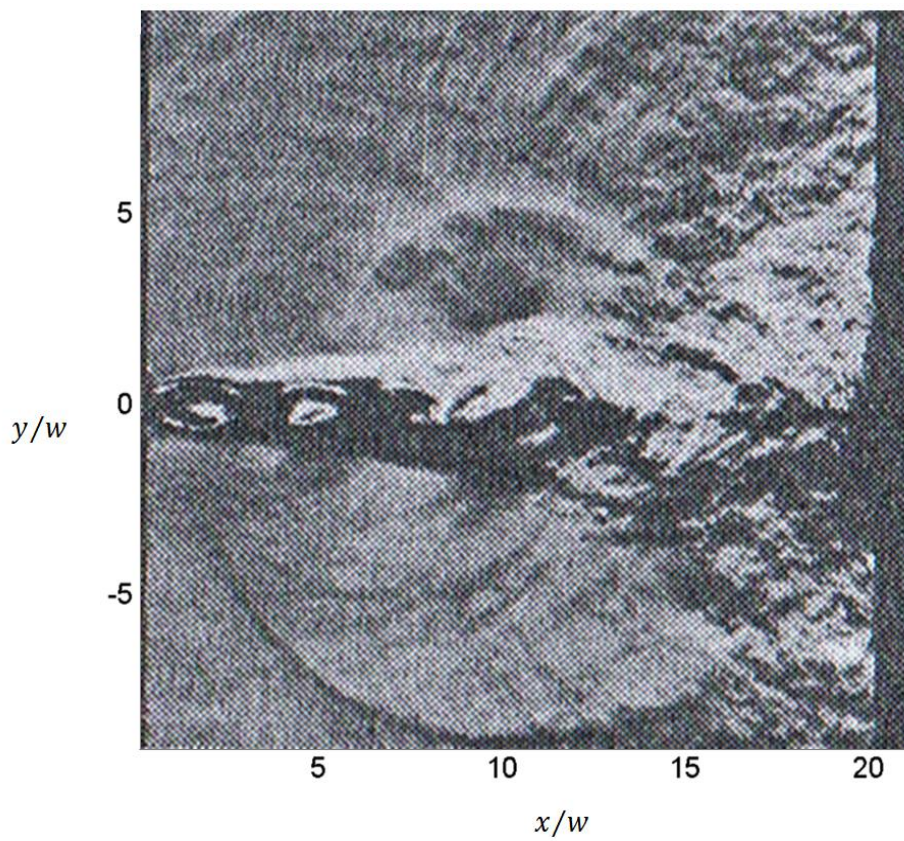


Figure 3.19 Numerical schlieren image in the impinging zone.



3.20 Schlieren photograph taken in the experiment: Krothapalli (1985).

3.4 Conclusions

The simulations carried out in this chapter prove that the CE/SE solver is capable of simulating the internal flow of the convergent-divergent nozzle in both underexpanded and overexpanded conditions; and the gas dynamics of the supersonic jet impinging on a surface. Therefore, it shows that the CE/SE solver is able to simulate both internal and external gas dynamics of the CGDS process.

4. Results of CGDS Simulations

In the first part of this chapter, the results of CE/SE simulations of CGDS gas dynamics are shown. In these simulations, high pressure gas with constant NPR and temperature is supplied at the inlet of a convergent-divergent nozzle and the gas is accelerated through the nozzle and reaches supersonic speed at the nozzle exit. Then this supersonic jet leaves the nozzle and impacts onto a normally located substrate. The supersonic jet decelerates and deflects due to the presence of the substrate surface and a transition from supersonic flow to subsonic flow there leads to the formation of a shockwave residing in front of the substrate. The pressure, density and temperature increase sharply across this stand-off shock and a high-pressure high-density high-temperature region is formed between the shock and the substrate surface. In this thesis, the gas dynamics of the CGDS process with different stand-off distances (SOD) are studied, while the nozzle geometry and supply gas conditions are kept constant.

The second part of this chapter shows the results of particle simulations. The simulations are carried out by applying the particle solver to the numerical results of the CGDS gas dynamics simulations. The particle solver is developed based on the formulations stated in Chapter 2, which

include the particle flight model, particle impact model and the heat transfer model. The particle motion and energetics of different injection locations are studied by fixing the particle initial velocity, initial temperature, size and density.

4.1 Gas dynamics studies of the CGDS process

In this section the gas dynamics of the CGDS process are studied by performing simulations using the CE/SE flow solver. A convergent-divergent nozzle with a rectangular cross-section is used, and all its dimensions are normalized by the nozzle exit width w . The length l/w of the diverging part of the nozzle is 12, the nozzle width at the throat is $1/3w$, exit area ratio $A_e/A_{th} = 3$ and the inlet width has the same length as the exit width. The NPR and temperature ratio P_0/P_a and T_0/T_a of the supply carrying gas are 12.5 and 4 respectively, where P_a and T_a are the ambient pressure and temperature.

4.1.1 Supersonic free jet from the CGDS nozzle

A simulation of the CGDS nozzle flow is carried out without the substrate to give a better understanding of the gas dynamics of the nozzle. The supply gas conditions are the same as in the CGDS simulations, so that NPR and

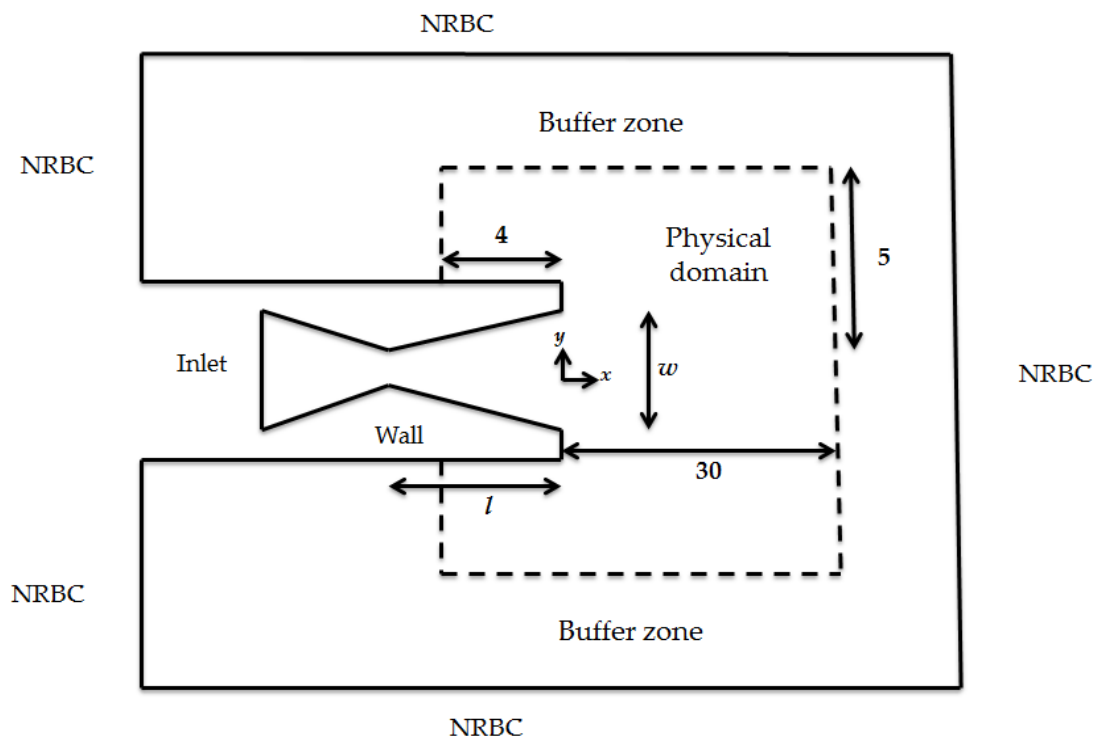


Figure 4.1 Computation domain of CGDS nozzle simulation.

supply gas temperature are 12.5 and 4 respectively. The computational domain is shown in Figure 4.1: the physical domain extends 30 units downstream, 4 units upstream and 5 units normal from the nozzle exit. The physical domain is surrounded by a large buffer zone. Non-reflecting boundary conditions (NRBC) are applied at the domain edges as outflow boundaries and no-slip adiabatic wall boundary conditions are applied at all nozzle walls. The inlet boundary conditions discussed in Chapter 2.3.5 are applied to the nozzle inlet where inlet pressure $p_{in} = NPR/\gamma = 8.93$, inlet

temperature $T_{in} = 1.5$, inlet density $\rho_{in} = NPR/T_{in} = 8.33$ and the inlet streamwise velocity $u_{in} = M_{in}\sqrt{T_{in}} = 0.24$. The initial conditions within the whole computational domain are defined as ambient conditions as discussed in Chapter 2.3.4, so that $p = 1/\gamma$, $T = 1$, $\rho = 1$ and $u = v = 0$. This simulation has a Reynolds number of 2.3×10^5 , and the time-step Δt is 1×10^{-3} . The whole computational domain is filled up by about 1 million triangular meshes and the calculation took about 100,000 iterations to obtain a converge solution inside the nozzle.

In Figure 4.2, the normalized density, normalized pressure and Mach number distribution inside and outside the nozzle are shown. The shock cells outside the nozzle can be clearly seen. Figures 4.3 to 4.6 show the density, pressure, temperature and Mach number variations along the nozzle centreline. The nozzle inlet, throat and nozzle exit are located at $x/w = -15$, $x/w = -12$ and $x/w = 0$ respectively. The results show that this CGDS nozzle is underexpanded and no shock is formed inside the nozzle; therefore the internal flow follows the isentropic relationships.

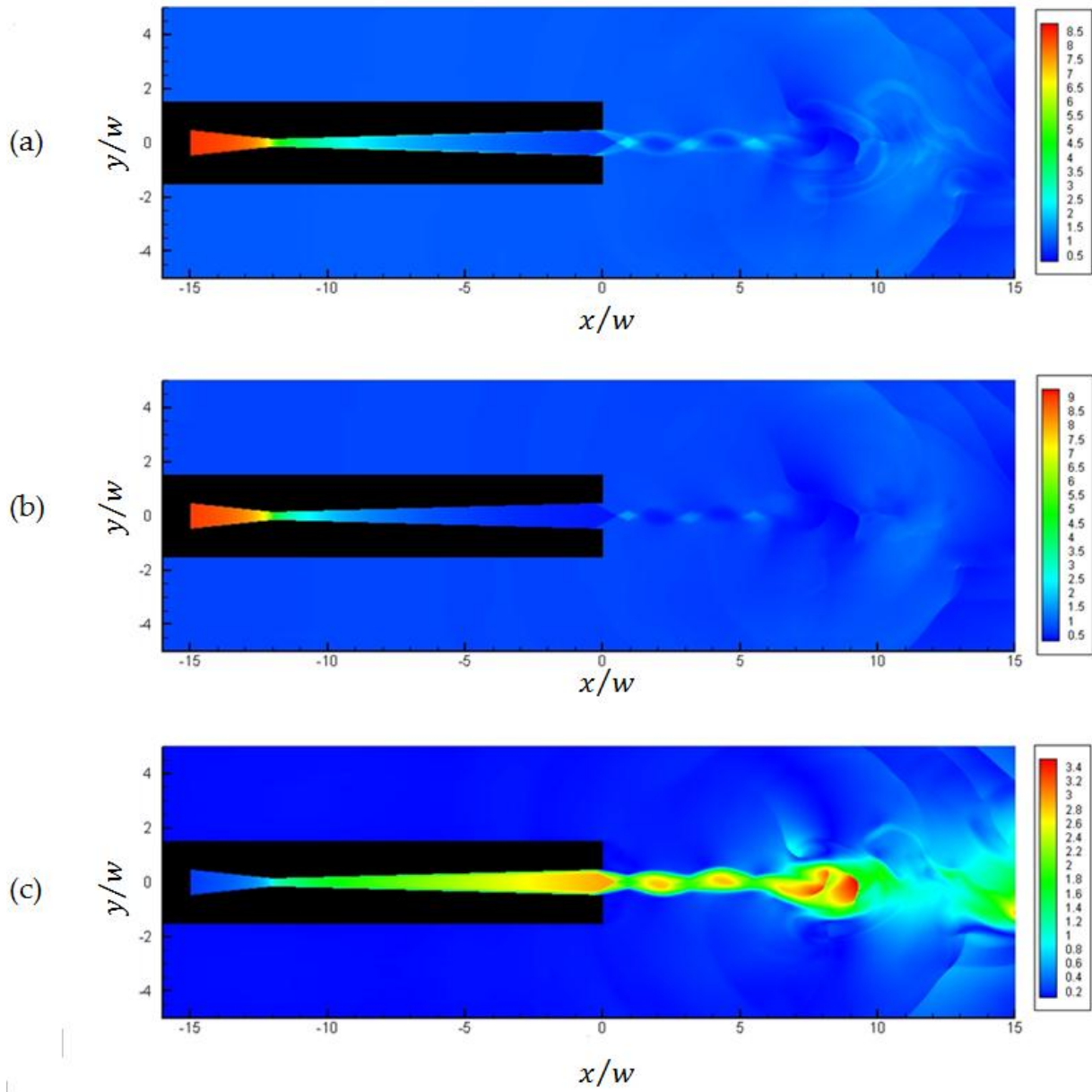


Figure 4.2 (a) Normalized density distribution; (b) normalized pressure distribution; (c) Mach number distribution.

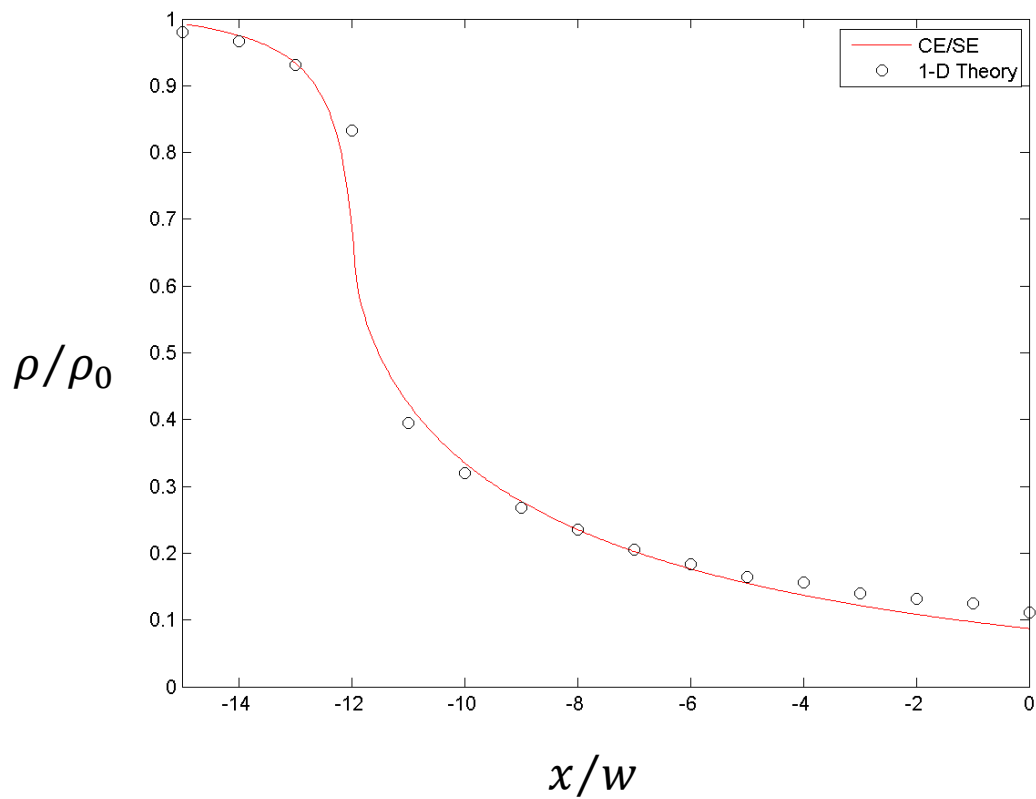


Figure 4.3 Density variations along the nozzle centerline.

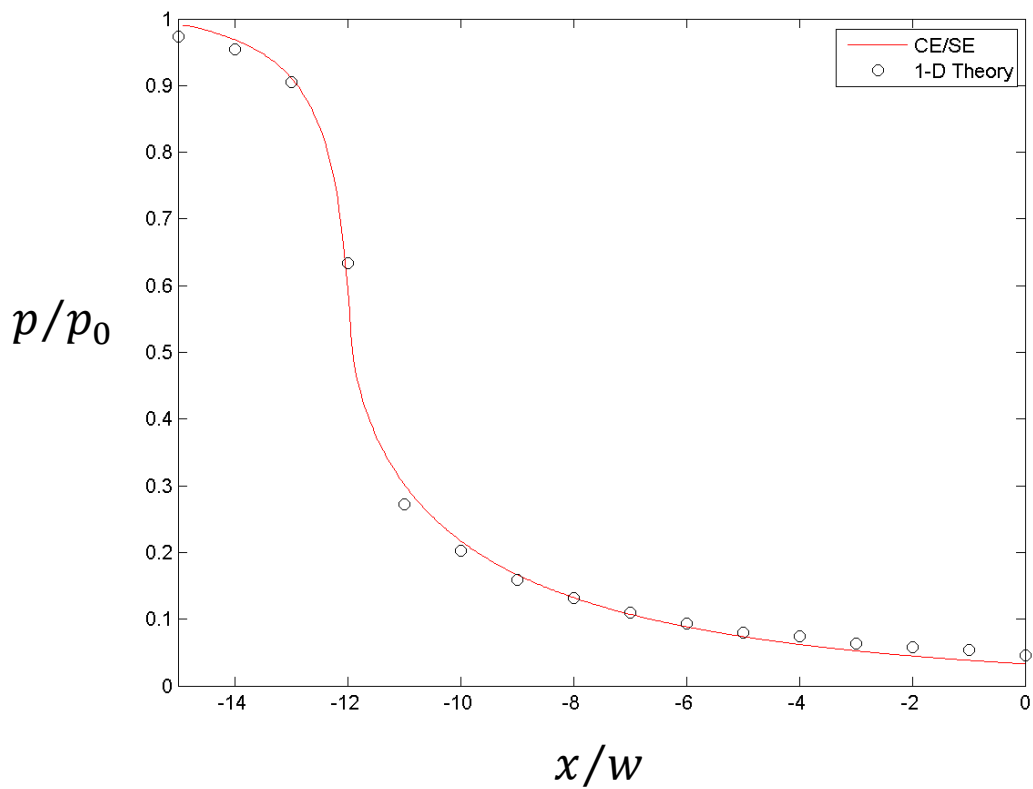


Figure 4.4 Pressure variations along the nozzle centerline.

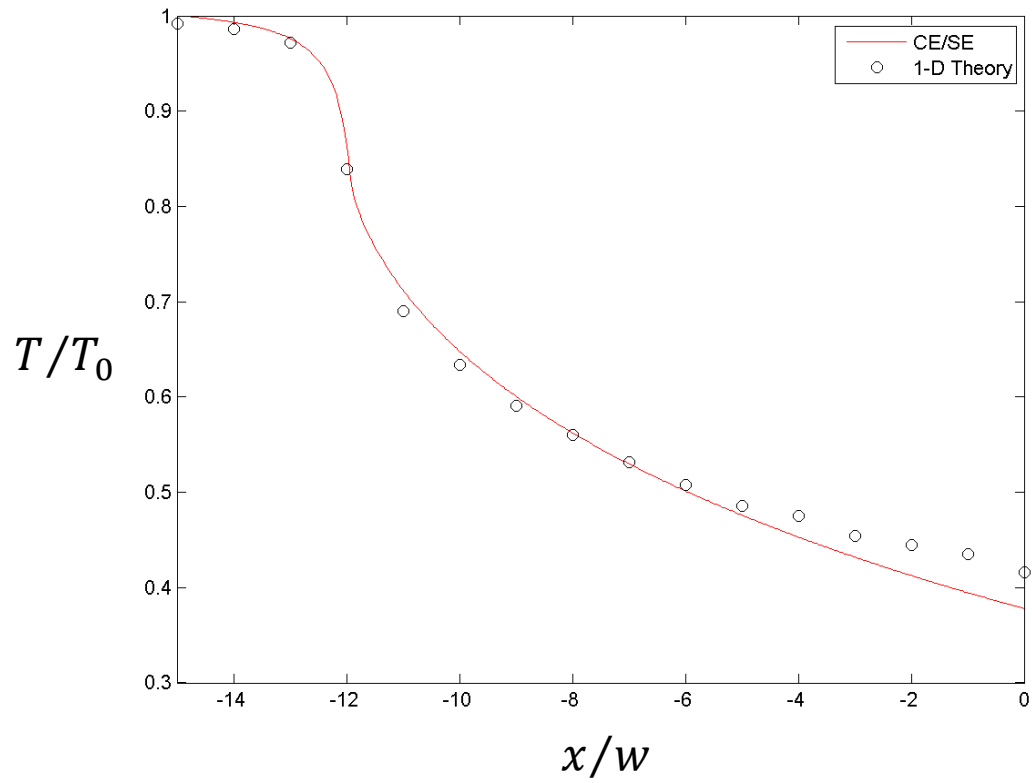


Figure 4.5 Temperature variations along the nozzle centerline.

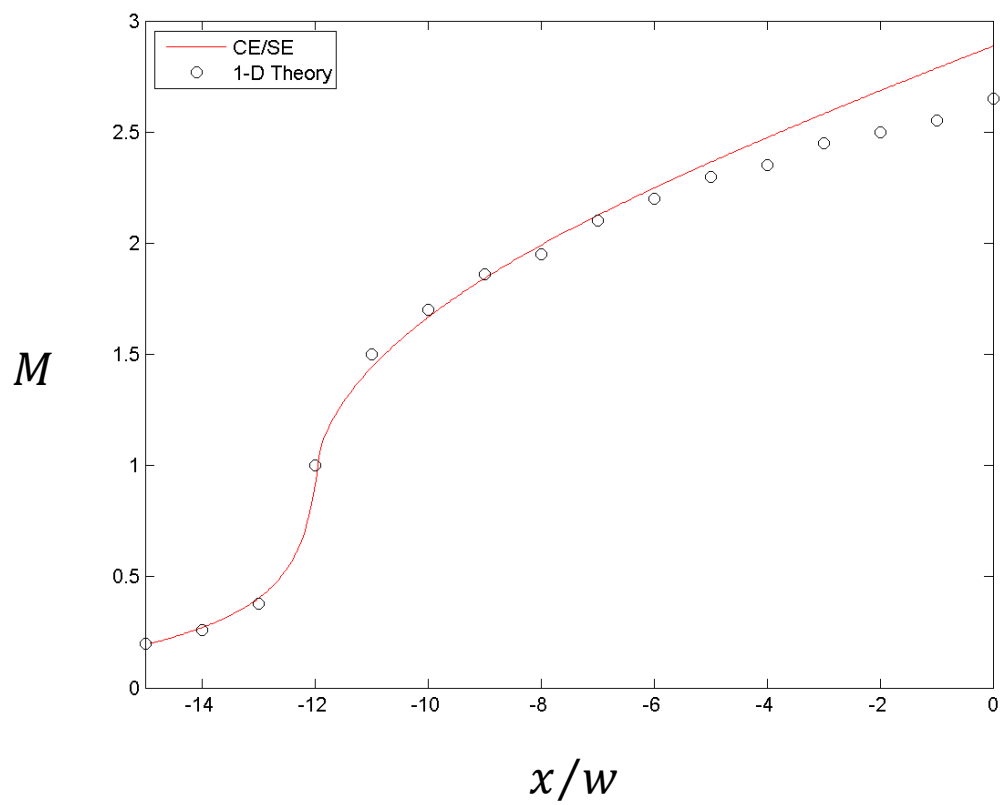


Figure 4.6 Mach number variations along the nozzle centerline.

4.1.2 CGDS gas dynamics simulations

Numerical studies of CGDS gas dynamics are carried out to provide flow field information for particle simulations. As mentioned in the previous chapter, a stand-off shock is developed in the impinging region, between the nozzle exit and the substrate surface. The Mach number drops across the shock and the driving force of particles decreases; therefore the impact velocity of particles is affected. In this section, the gas dynamics of the CGDS process with different substrate stand-off distances are studied.

The geometry of the nozzle and the schematic of the computational domain are shown in Figure 4.7. The nozzle used in these simulations is the same nozzle used in Chapter 4.1 but with a thinner nozzle wall. All the dimensions are normalized by the nozzle exit width w , the SODs between the nozzle exit and the substrate surface are in a range between $0.5w$ and $2w$. The physical domain is surrounded by a large buffer zone. The numerical setup is similar to the setup shown in Chapter 4.1, non-reflecting boundary conditions (NRBC) are applied at the domain edges as outflow boundaries and no-slip adiabatic wall boundary conditions are applied to the nozzle walls and substrate surface. The inlet boundary conditions discussed in Chapter 2.3.5, are applied to the nozzle inlet where inlet pressure $p_{in} =$

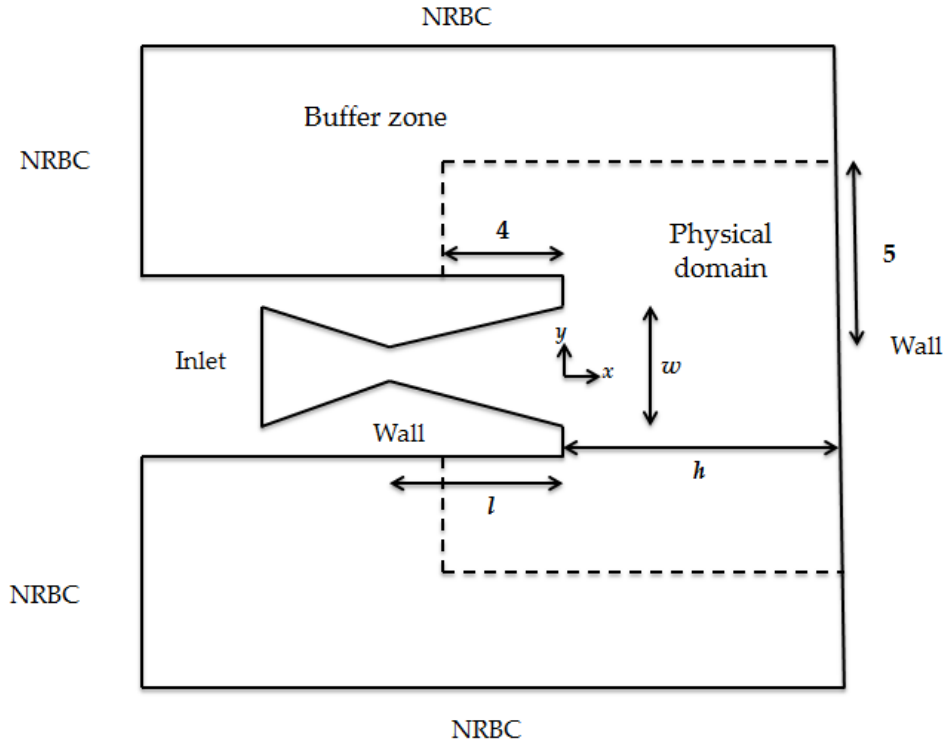


Figure 4.7 Computation domain for impinging jet simulations.

$NPR/\gamma = 8.93$, inlet temperature $T_{in} = 4$ and inlet density $\rho_{in} = NPR/T_{in} = 2.23$. The inlet streamwise velocity u_{in} at the inlet is calculated by Equations 1.2 and 1.6, with given area ratio of the nozzle, the Mach number M_{in} at the inlet can be found (Equation 1.6), so that $u_{in} = M_{in}\sqrt{T_{in}} = 0.5$. The initial conditions within the whole computational domain are defined as ambient conditions as discussed in Chapter 2.3.4, so that $p = 1/\gamma$, $T = 1$, $\rho = 1$ and $u = v = 0$. This simulation has a Reynolds number of 2.3×10^5 and the time-step Δt is 1×10^{-3} . The whole computational domain is filled up by about 0.5-0.7 million triangular meshes. The calculations took about 150,000

time steps to obtain converge solutions.

Results of gas dynamics simulation with $SOD = 2$

The results of simulation with $SOD = 2$ are discussed in this section. Figures 4.8 - 4.11 show the distributions of normalized density, pressure and Mach number in the impinging region, where the stand-off shock and the shear layer of the jet can be clearly seen. There are sharp increases in pressure and density across the stand-off shock and sharp decreases in Mach number. Figure 4.12 is the numerical schlieren image, which shows the density gradient magnitude in the impinging region, the shear layer and the stand-off shock can be seen more clearly.

The density, pressure, temperature and Mach number variations along the centreline of the jet are shown in Figures 4.13 - 4.16. The nozzle inlet, throat and exit are located at $x/w = -15$, $x/w = -12$ and $x/w = 0$ respectively, and the substrate is normally located at $x/w = 2$. The results show that the flow inside the nozzle follows the isentropic relationships; therefore it can be assumed that the substrate does not affect the flow inside the nozzle.

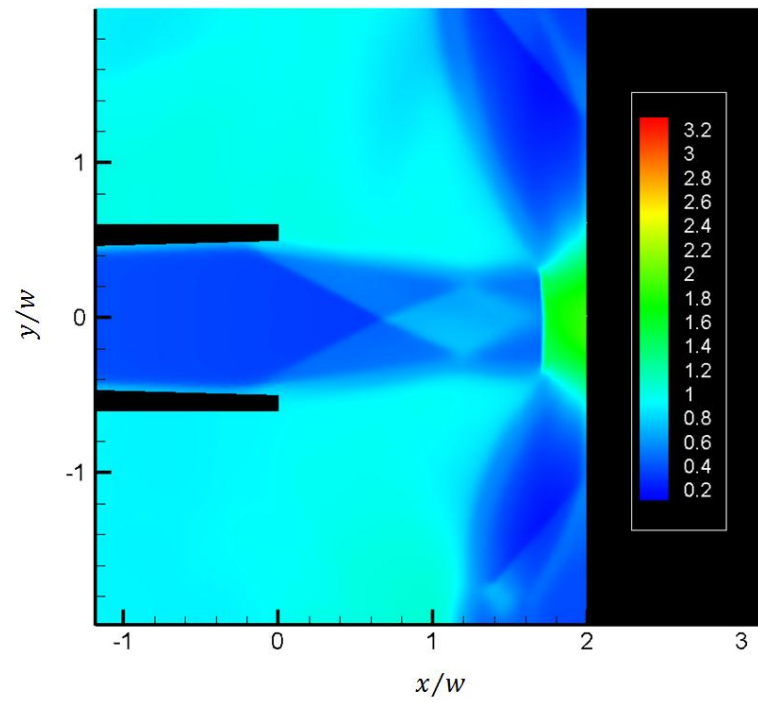


Figure 4.8 Normalized density distributions in the impinging region.

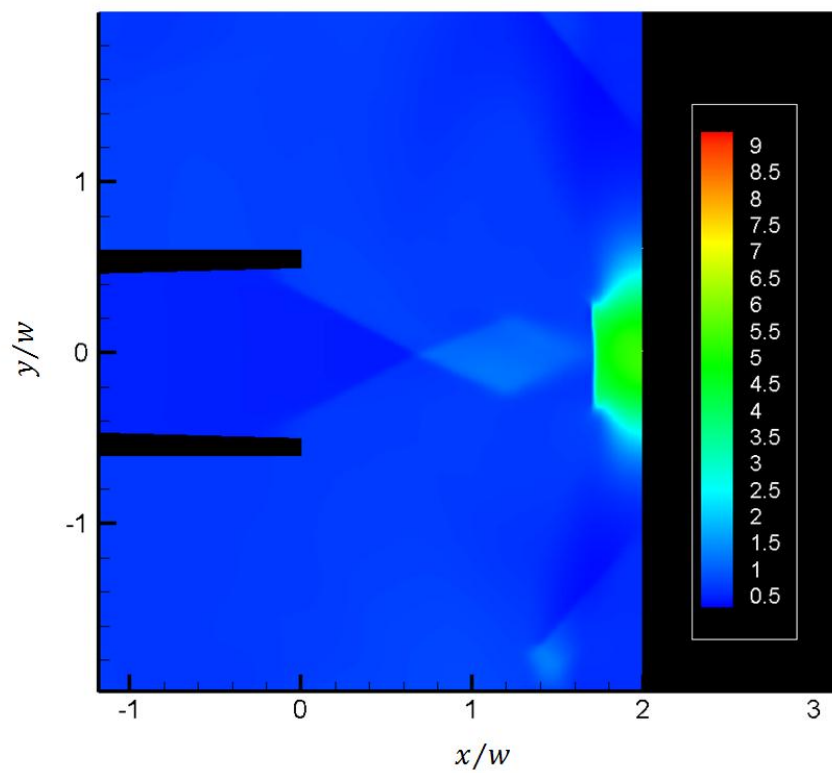


Figure 4.9 Normalized pressure distributions in the impinging region.

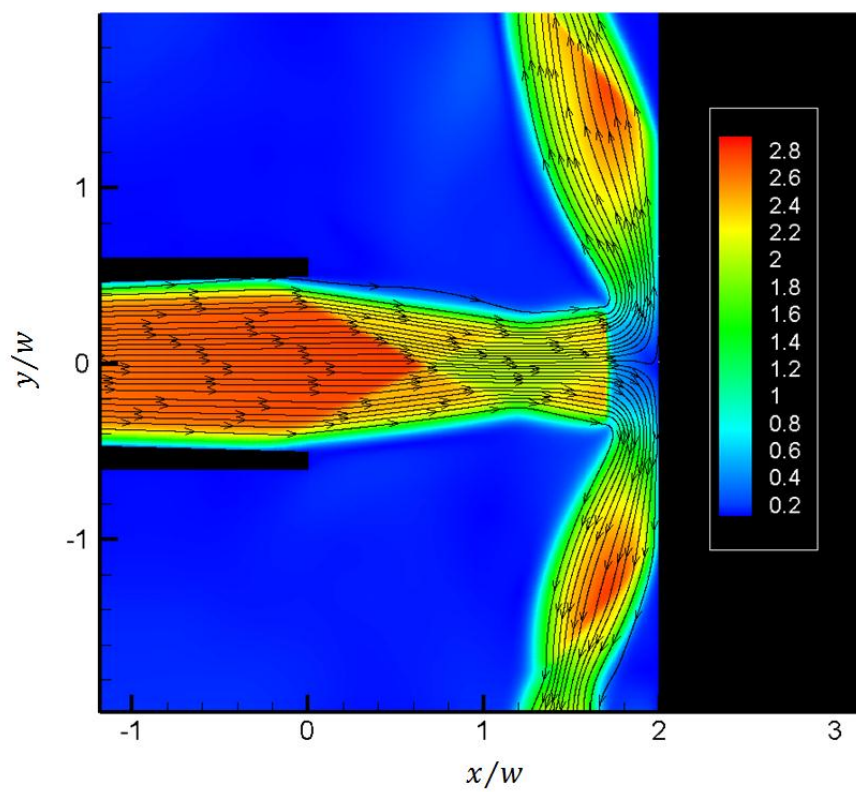


Figure 4.10 Mach number distributions with streamline in the impinging region.

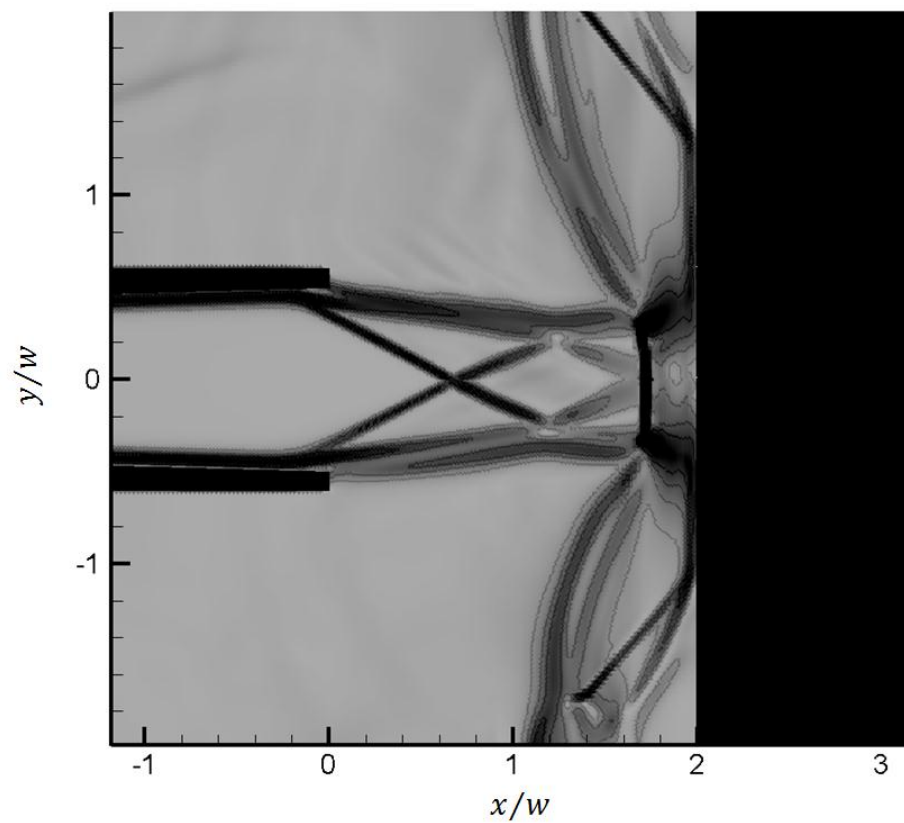


Figure 4.12 Schlieren in the impinging region.

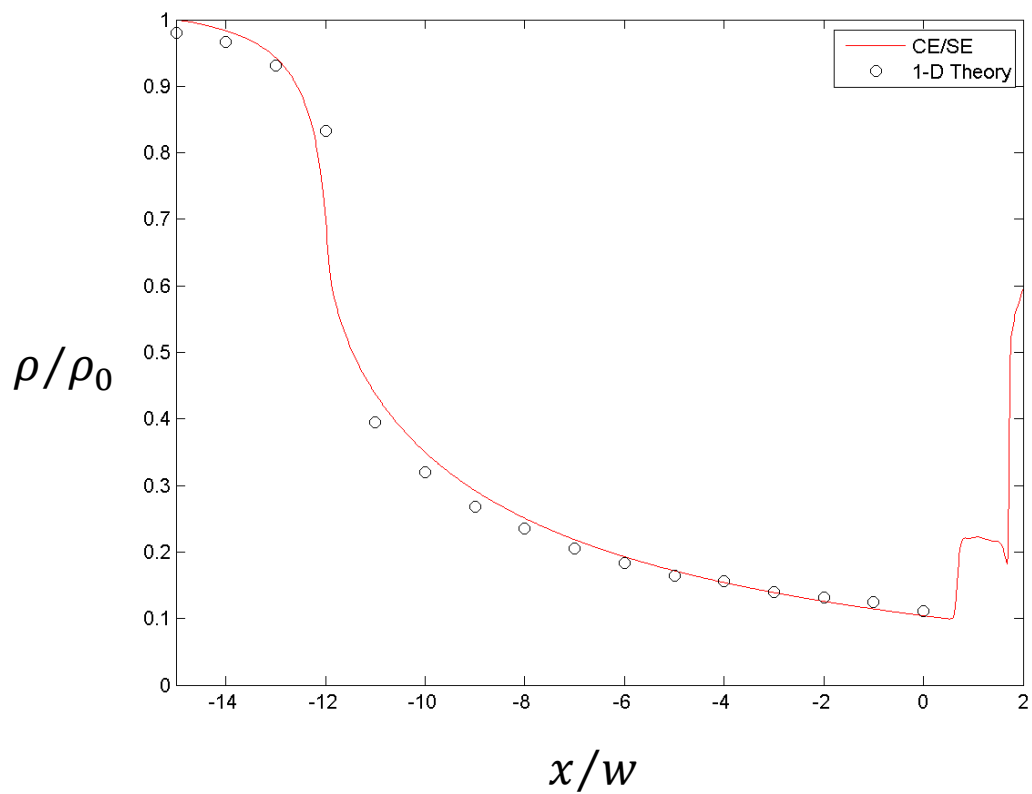


Figure 4.13 Density variations along the centerline.

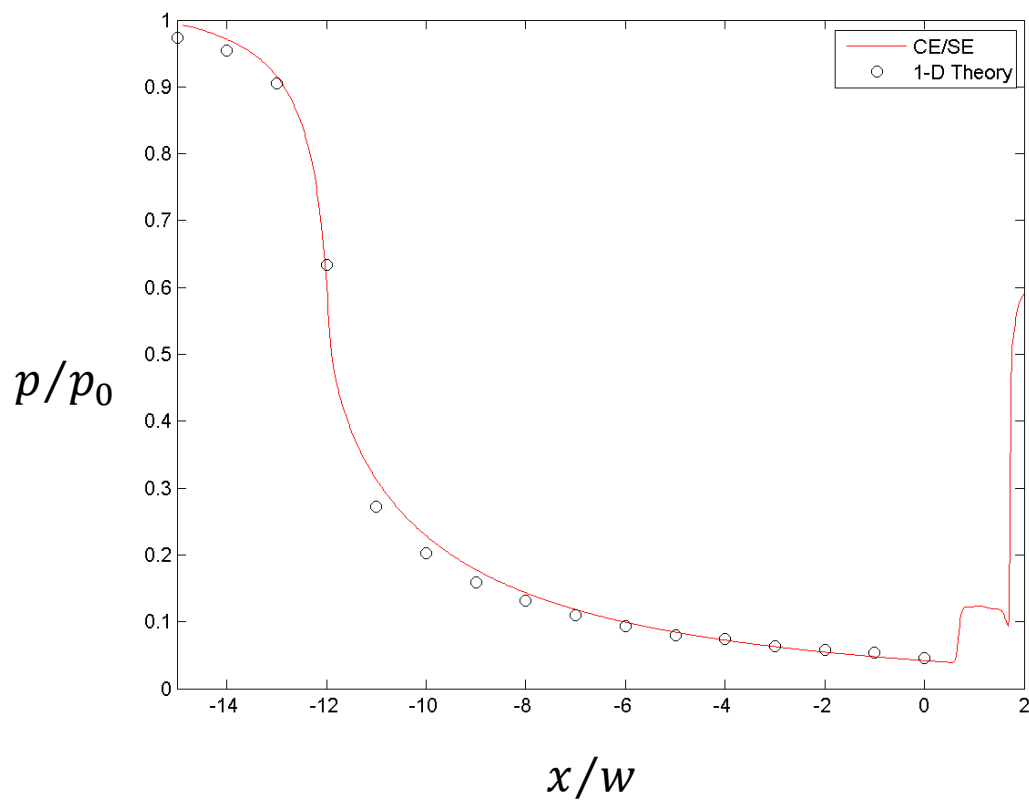


Figure 4.14 Pressure variations along the jet centerline.

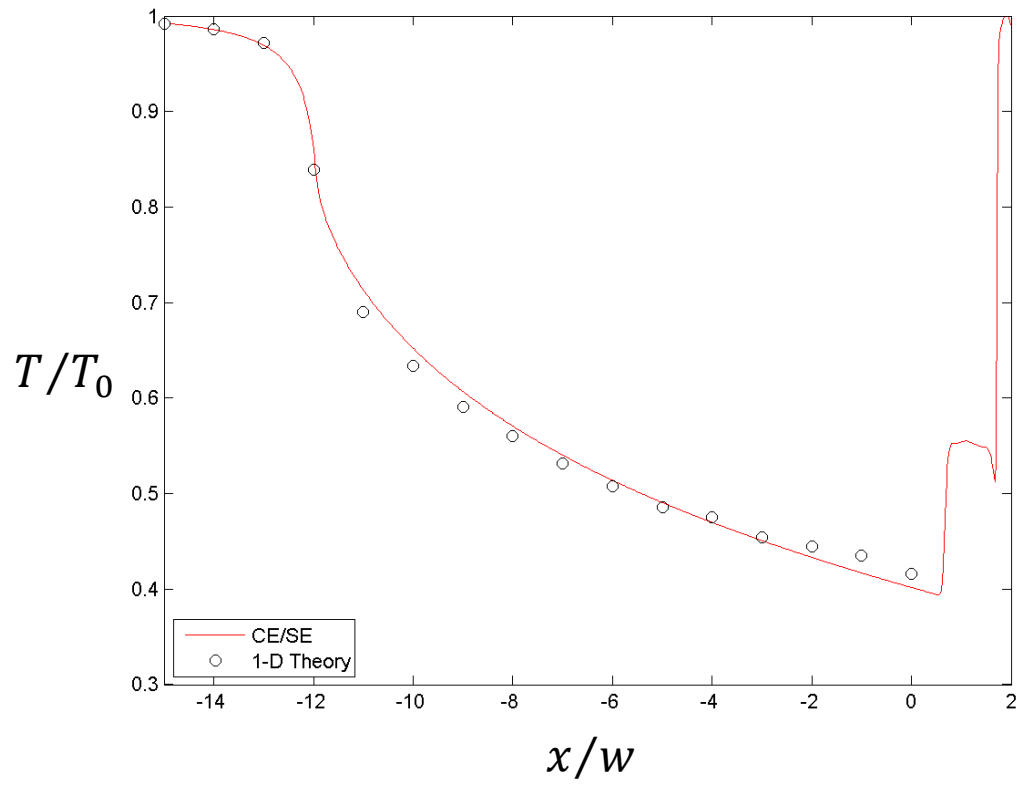


Figure 4.15 Temperature variations along the centerline.

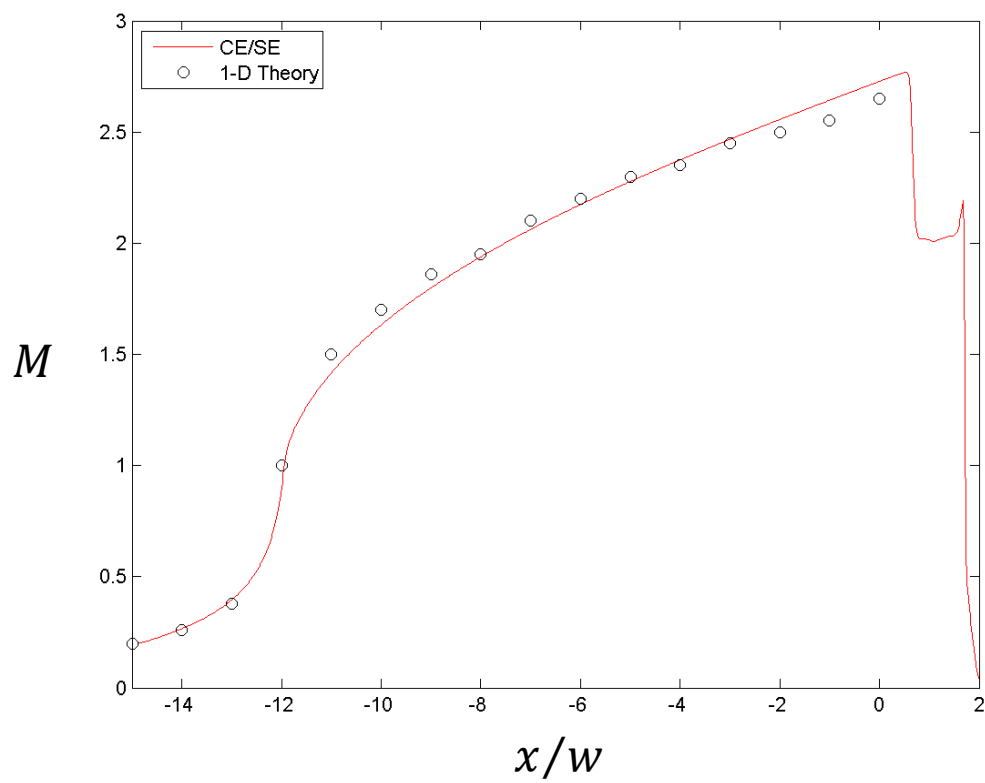


Figure 4.16 Mach number variations along the centerline.

Figures 4.17 and 4.18 show the pressure and Mach number variations along the centreline in the impinging zone. There are two obvious changes: the first is located at $x/w = 0.7$ which represents the exits of the shock cell, and the second represents the stand-off shock which has a sharp increase of pressure and a sharp decrease of Mach number. The pressure ratio p_2/p_1 across the shock, Mach number downstream of the shock M_2 and the distance between the stand-off shock and the substrate Δ are compared to normal shock relationships (Eqs. 1.11 – 1.12) and Billig's approximation (Equation 1.13) in Table 4.1.

| | p_2/p_1 | M_2 | Δ |
|---|-----------|-------|----------|
| CE/SE simulation | 5.2 | 0.5 | 0.24 |
| Normal shock relationships, $M_1 = 2.2$ | 5.48 | 0.55 | / |
| Billig's approximation, $M_e = 2.75$ | / | / | 0.22 |

Table 4.1 Comparison of stand-off shock location, Mach number and pressure ratio.

Table 4.1 shows that differences between CE/SE simulation and normal shock relationships and Billig's approximation are less than 10%. These results also show the shock capturing capability of the CE/SE solver.

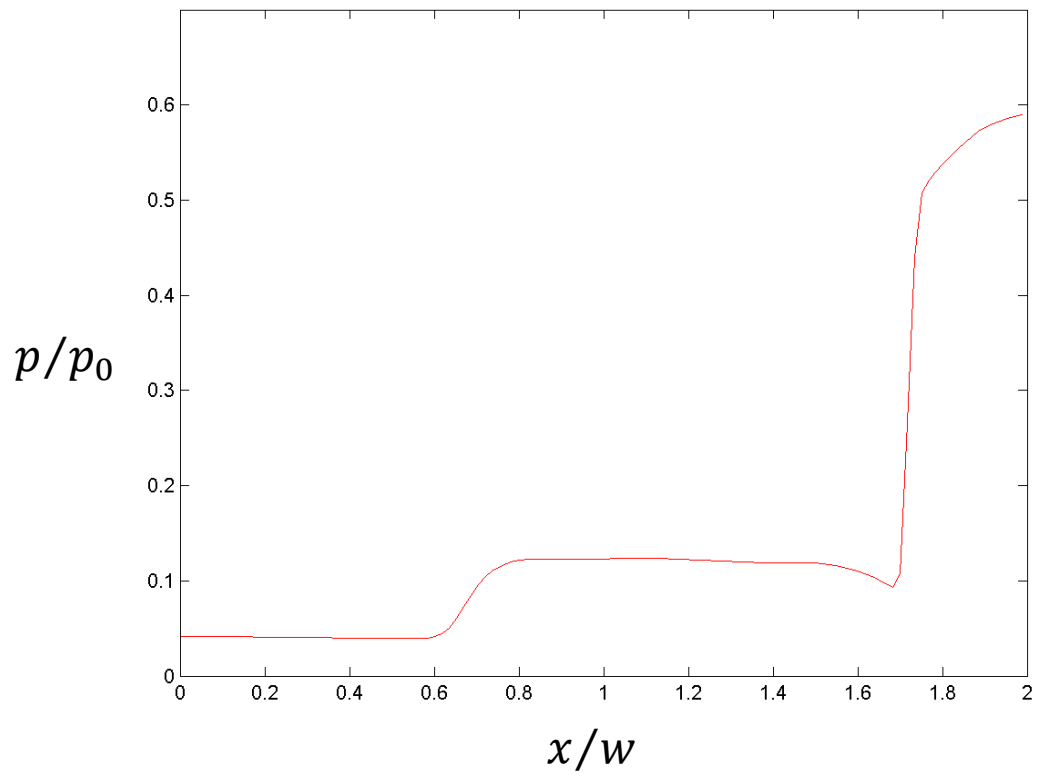


Figure 4.17 Pressure variations along the centreline of the impinging zone.

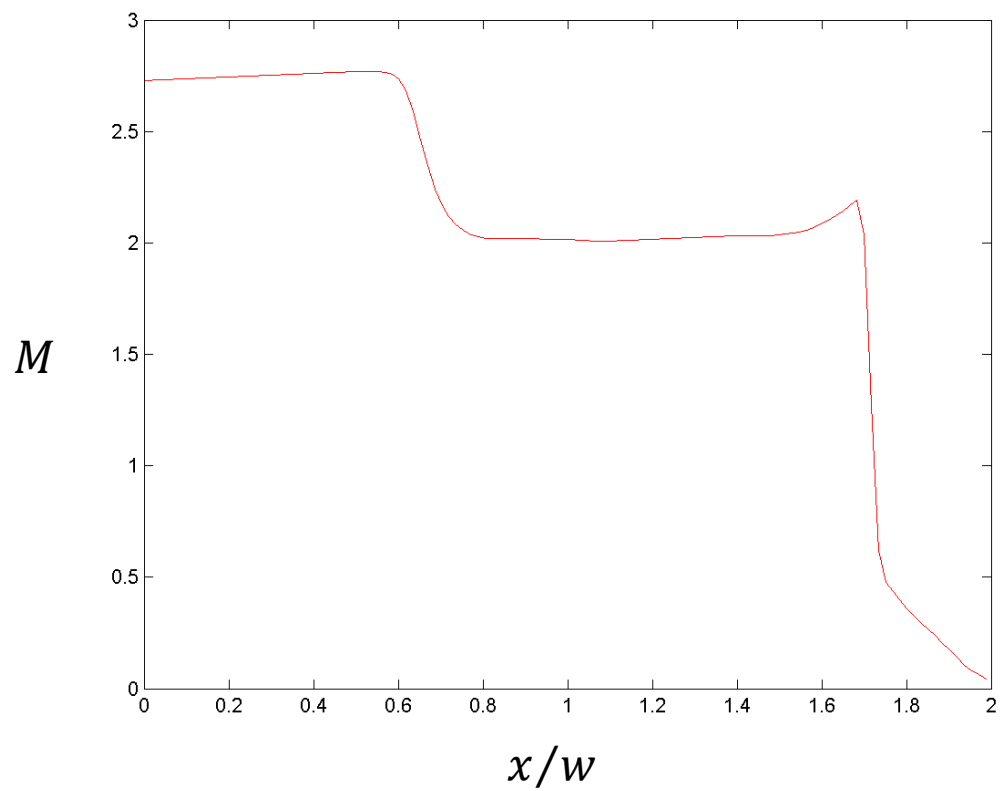


Figure 4.18 Mach number variations along the centreline of the impinging zone.

Results of gas dynamics simulation of different SODs

Figures 4.19 - 4.22 show the density, pressure, streamwise velocity and Mach number in the impinging zone of different SODs. The comparisons of the flow features are shown in Table 4.2. The exit Mach number of different simulations are nearly the same ($M_e = 2.75$), and Δ should also be the same according to Billig's approximation (Equation 1.13); however Δ is much larger when SOD is small. This result shows that Billig's approximation is not able to predict the location of the stand-off shock if the substrate is too close to the nozzle exit. From Figure 4.23 and 4.24, the pressure and Mach number variations inside the nozzle follow the isentropic relationships, which show that the internal flow inside the nozzle is independent of the substrate location.

| SOD | No. of Shock cell | Δ | Billig's approximation |
|-----|-------------------|----------|------------------------|
| 0.5 | 0 | 0.5 | 0.22 |
| 1.0 | 0 | 0.5 | 0.22 |
| 1.5 | 0.5 | 0.24 | 0.22 |
| 2.0 | 1 | 0.24 | 0.22 |

Table 4.2

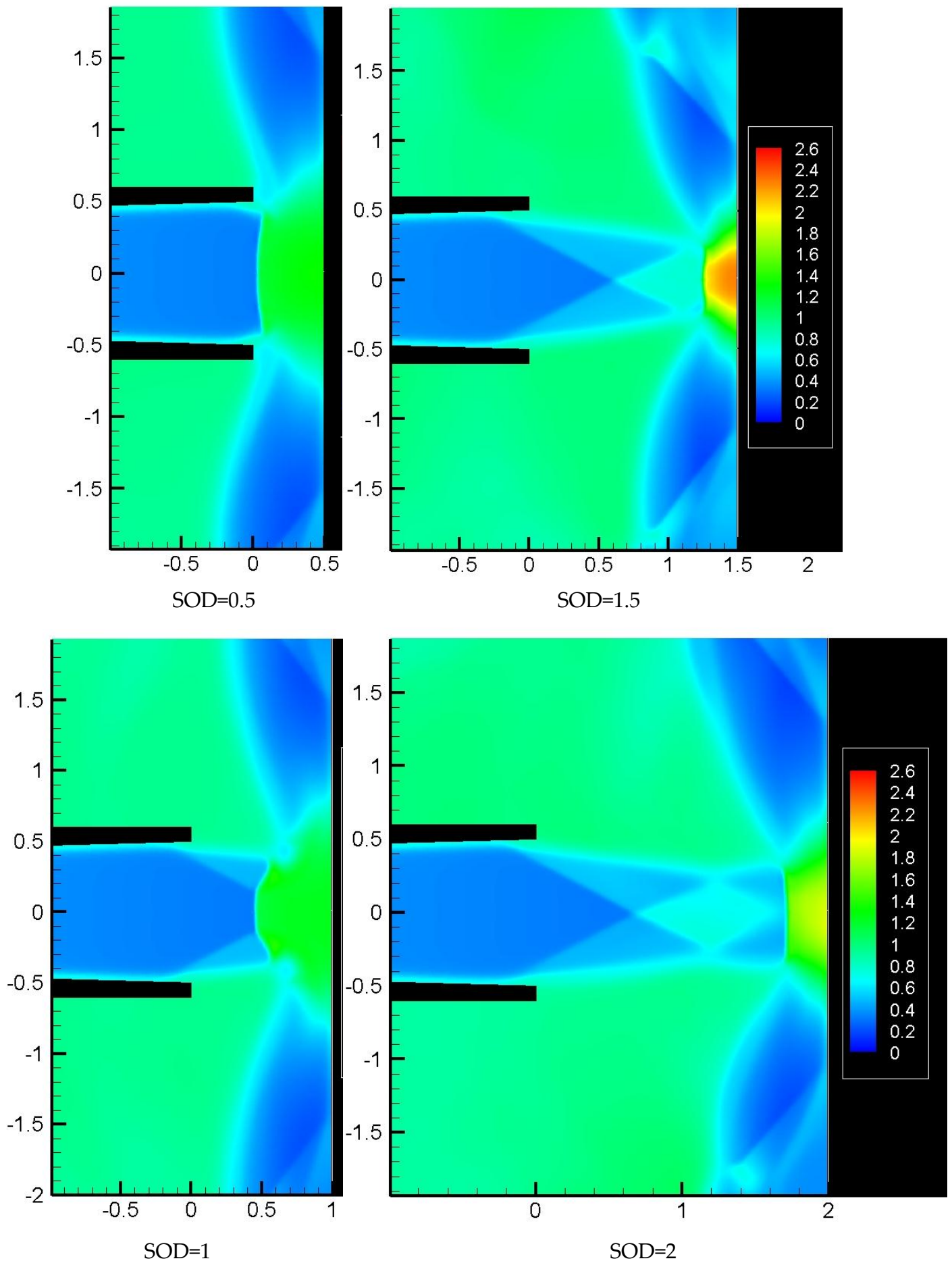


Figure 4.19 Density in the impinging zone.

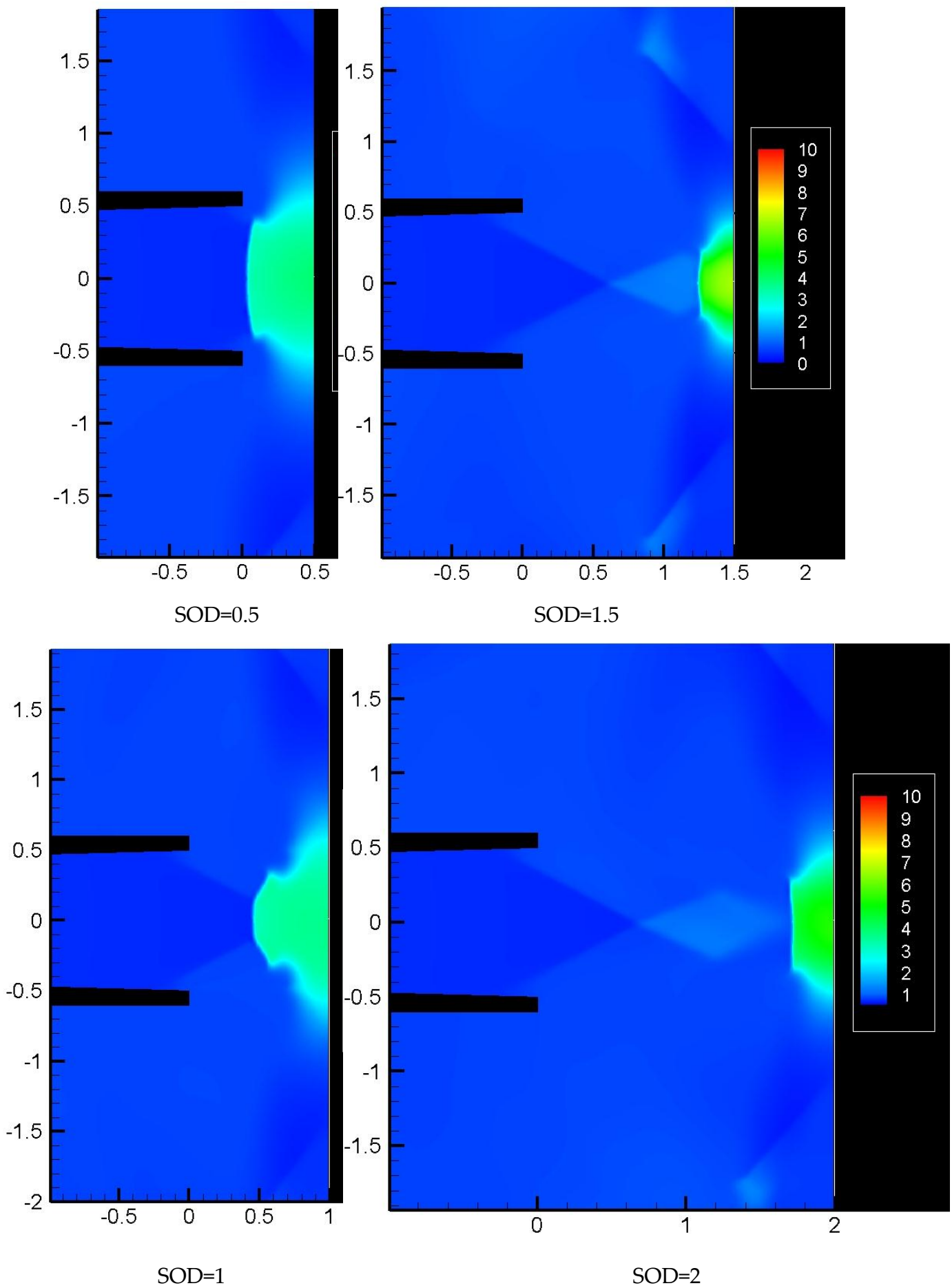


Figure 4.20 Pressure in the impinging zone.

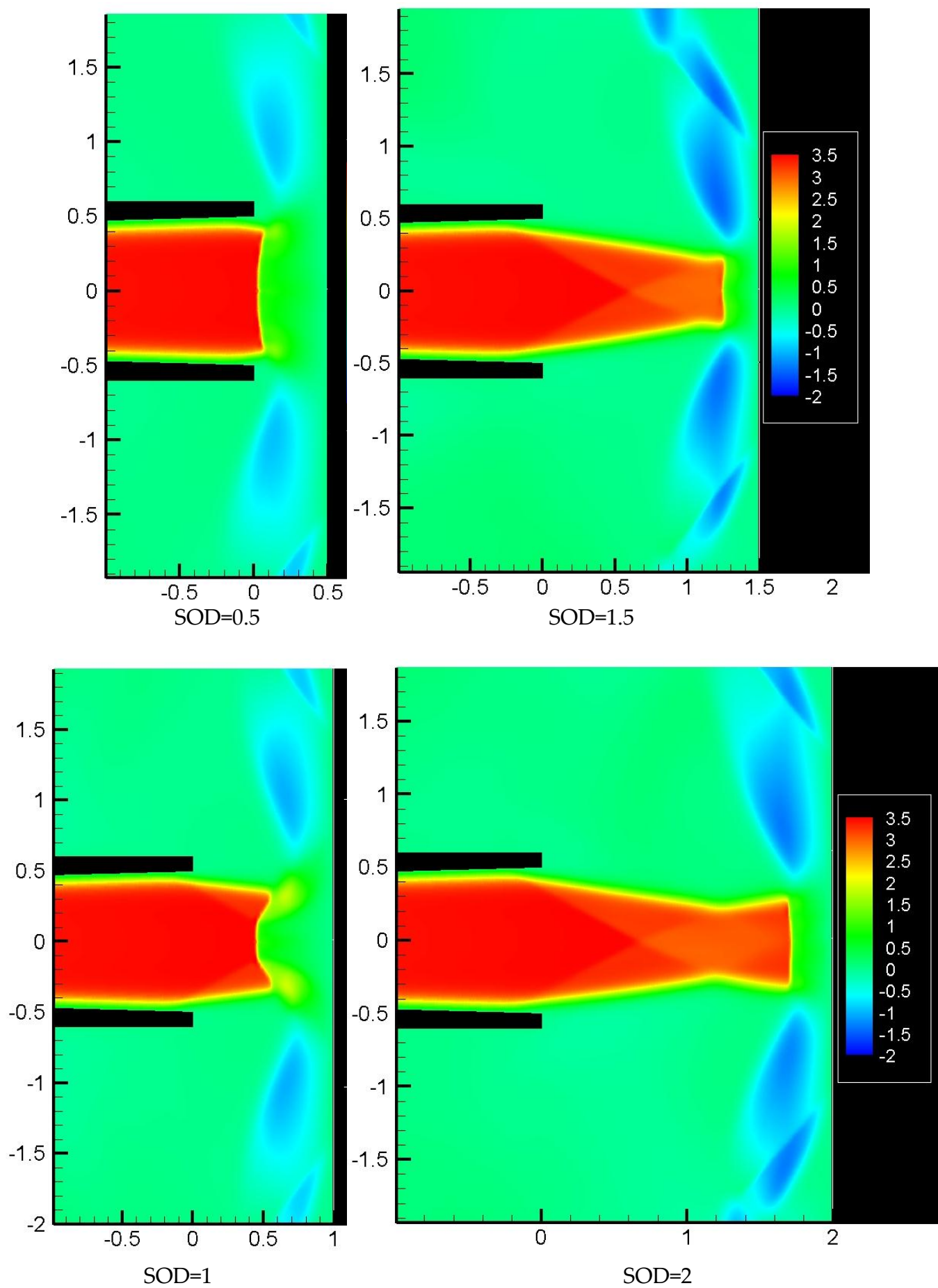


Figure 4.21 Streamwise velocity u in the impinging zone.

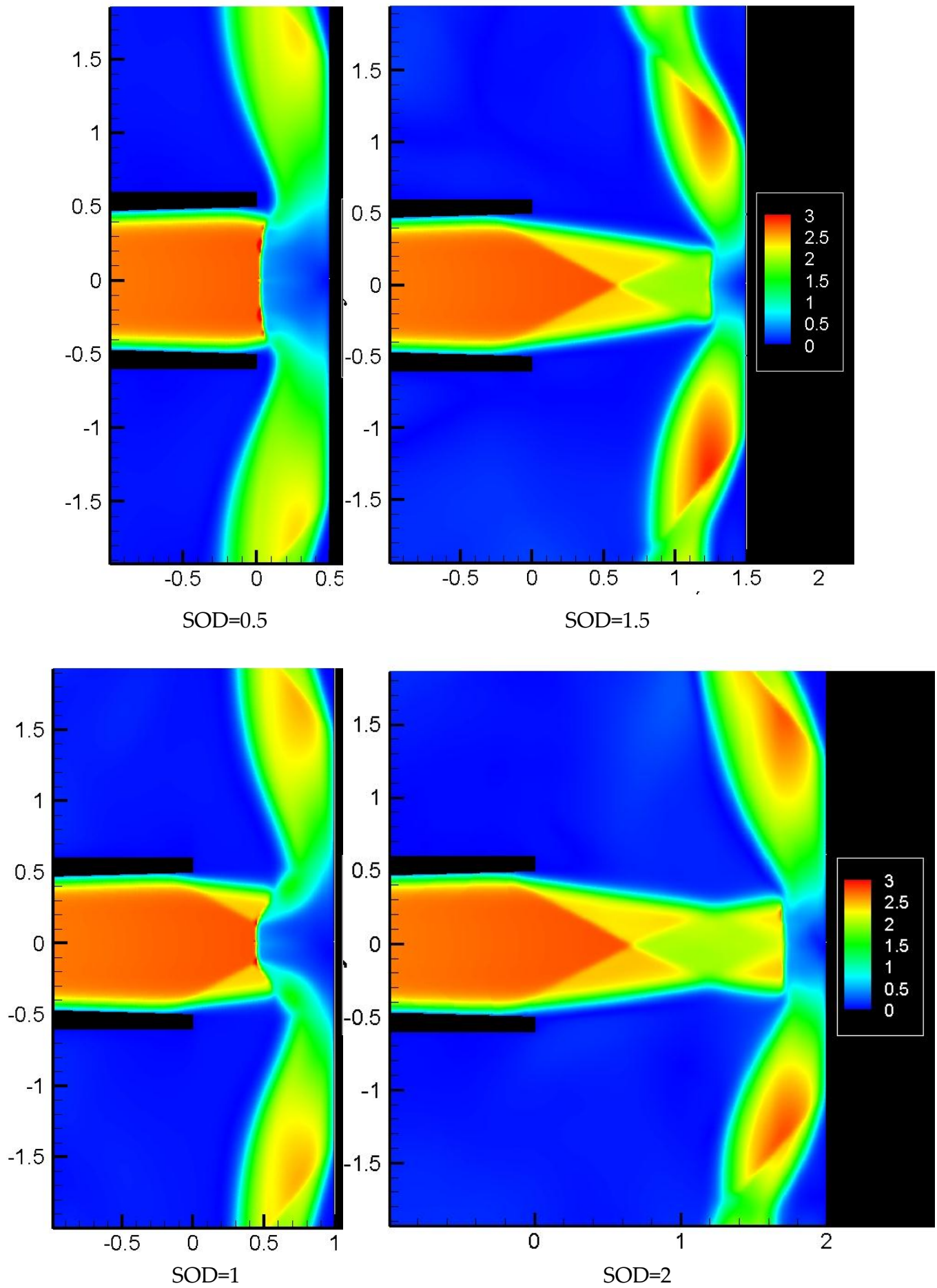


Figure 4.22 Mach number in the impinging zone.

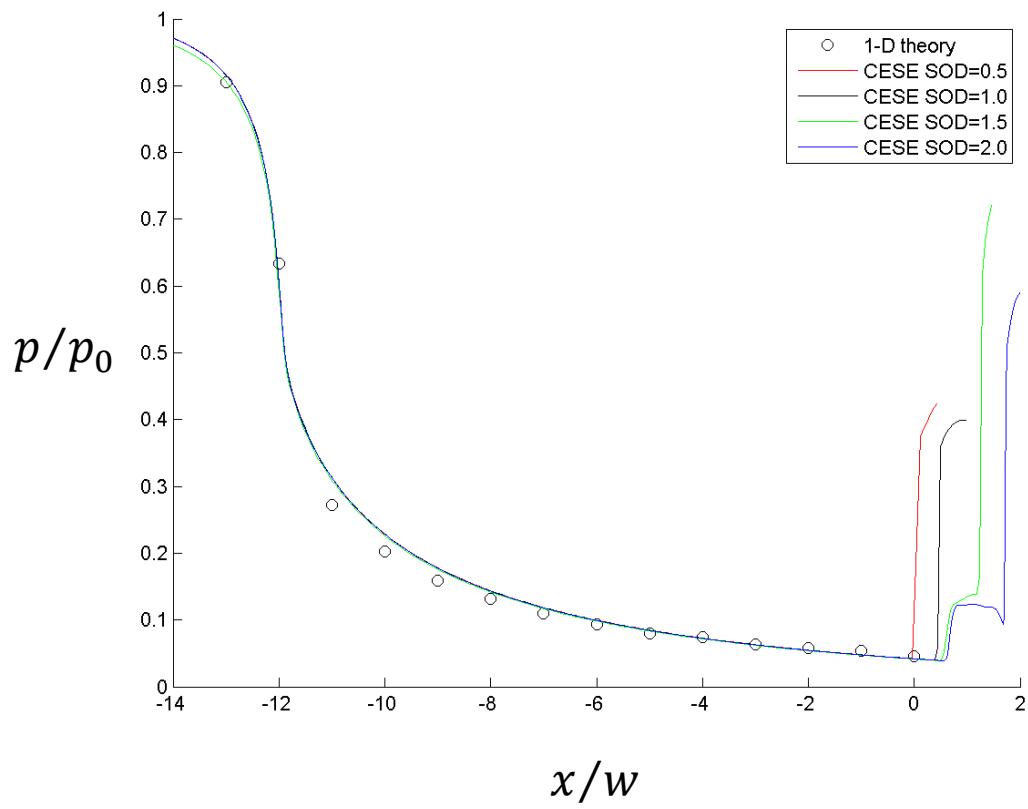


Figure 4.23 Pressure variations along the centerline.

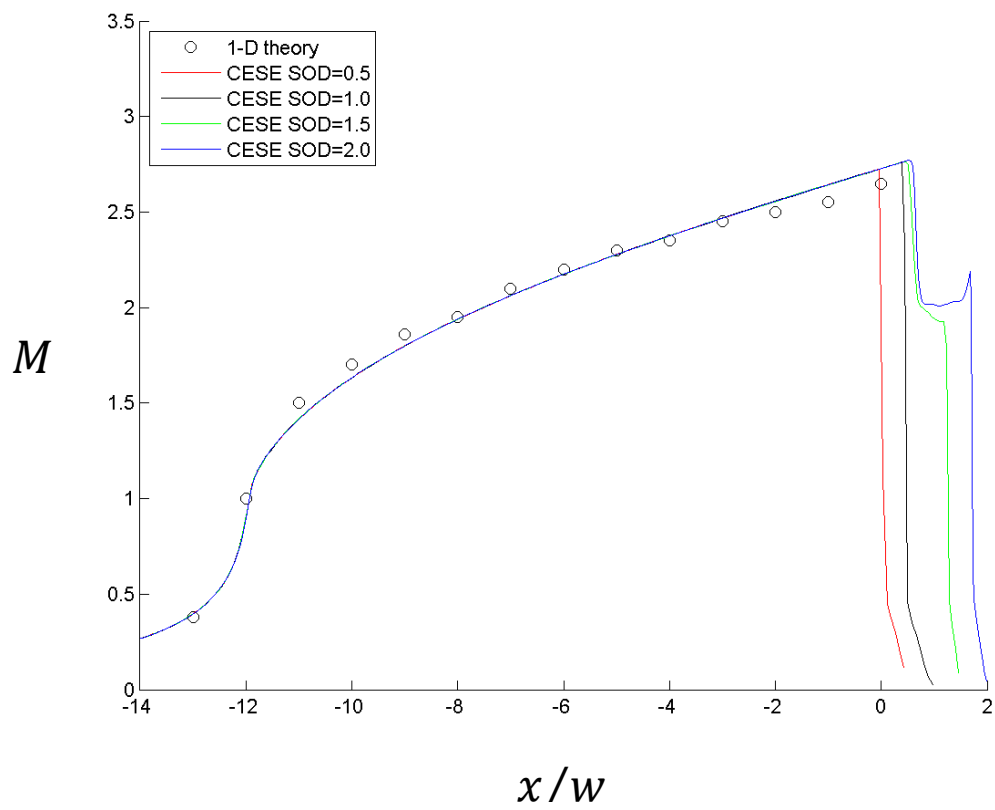


Figure 4.24 Mach number variations along the centreline

4.2 Particle simulations

The flight model, impact model and heat transfer model of particles are discussed in Chapter 2.4, and a particle solver is developed to simulate the CGDS process based on the formulations of these models. By applying the particle code to the field results from the CE/SE simulations, the flight path, temperature and impact result of each particle can be found.

The flow field data such as gas velocity vector \mathbf{V}_g , gas temperature T_g and gas density ρ_g at the solution point which has minimum distance from a particular particle are used to determine the acceleration and heat transfer rate of that particle. Then the complete flight path and the impact result of each particle is simulated by iterating the particle solver with a small time step value.

4.2.1 Initial particle data

Initial particle data are also required in the particle simulation. In this study, aluminium powder with constant diameter $\bar{d}_p = 15\mu\text{m}$ is used as the coating material, and the initial velocity of each particle is assumed to be stationary ($\mathbf{V}_p = 0$) after injection and the particles are injected at room temperature so that the initial particle temperature $T_p = 1$.

4.2.2 Particle motion

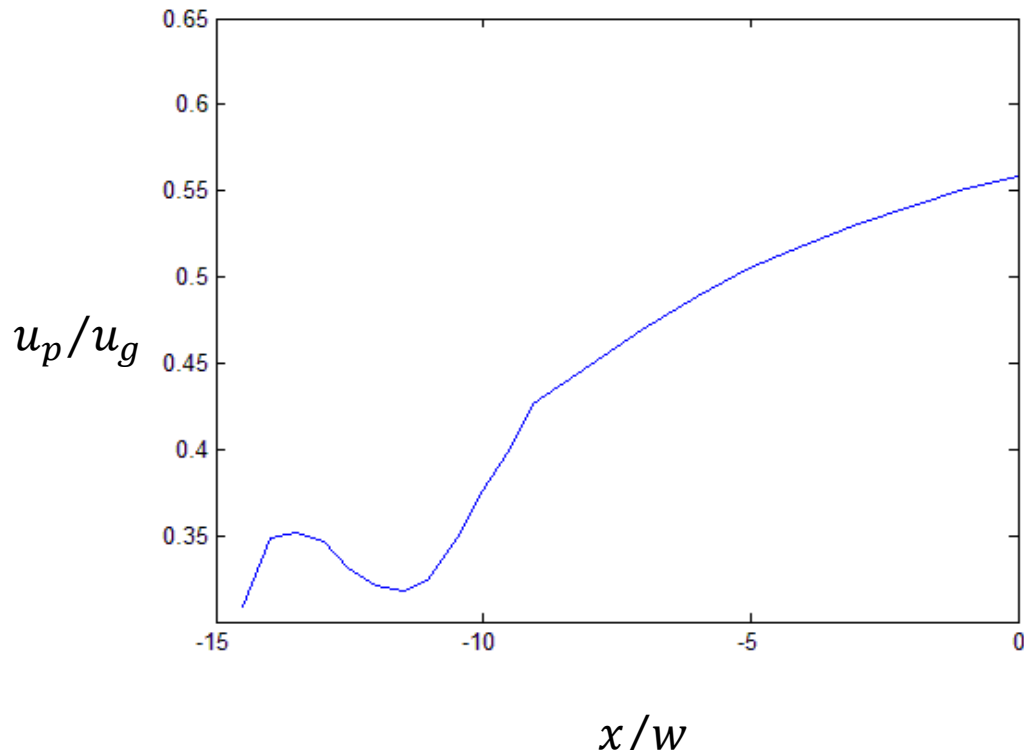


Figure 4.26 Velocity ratio variations between gas and particles.

converging zone ($x/w = -15$). This result shows that the percentage difference between particle velocity and gas velocity is decreasing. As discussed in Chapter 4.1, the internal nozzle flow follows the isentropic relationships and is not affected by the location of the substrate. Figures 4.27 - 4.29 show the velocity of particles injected at different locations along the nozzle, from which it is clear that particle motion inside the nozzle is independent of the SOD of the substrate.

The particle velocities drop due to the deceleration of the carrying gas across the stand-off shock; however the drop is very small compared with its velocity at the nozzle exit, so that the impact velocity can be approximated by the particle velocity at the nozzle exit.

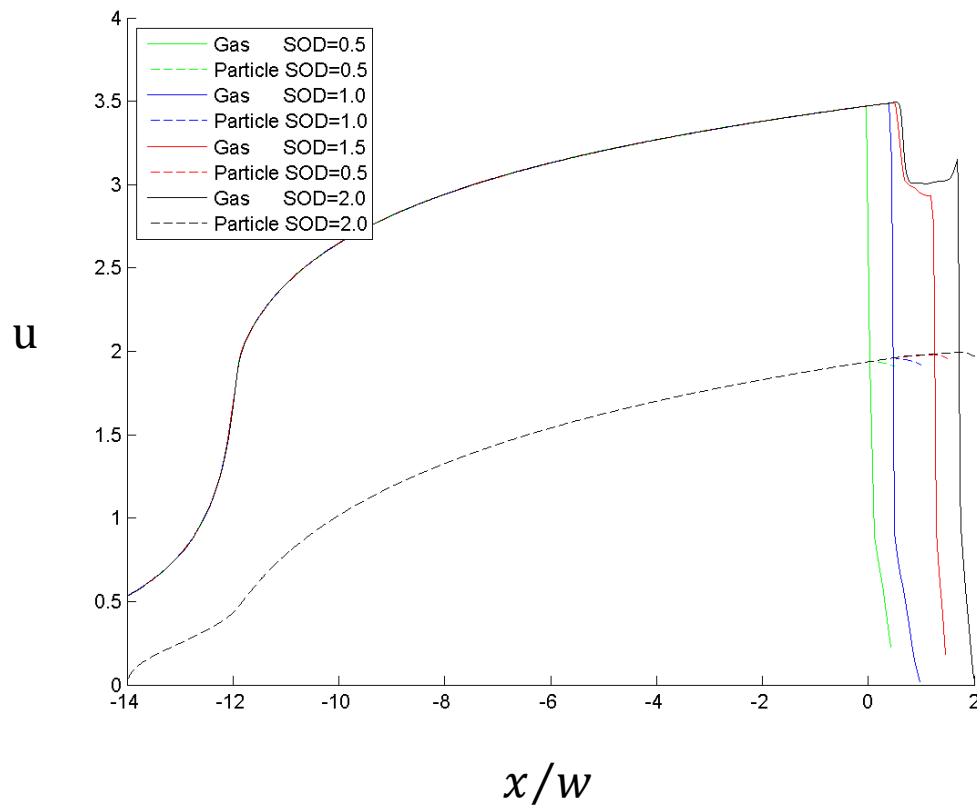


Figure 4.27 Velocity variation of particles injected at the $x/w = -14$.

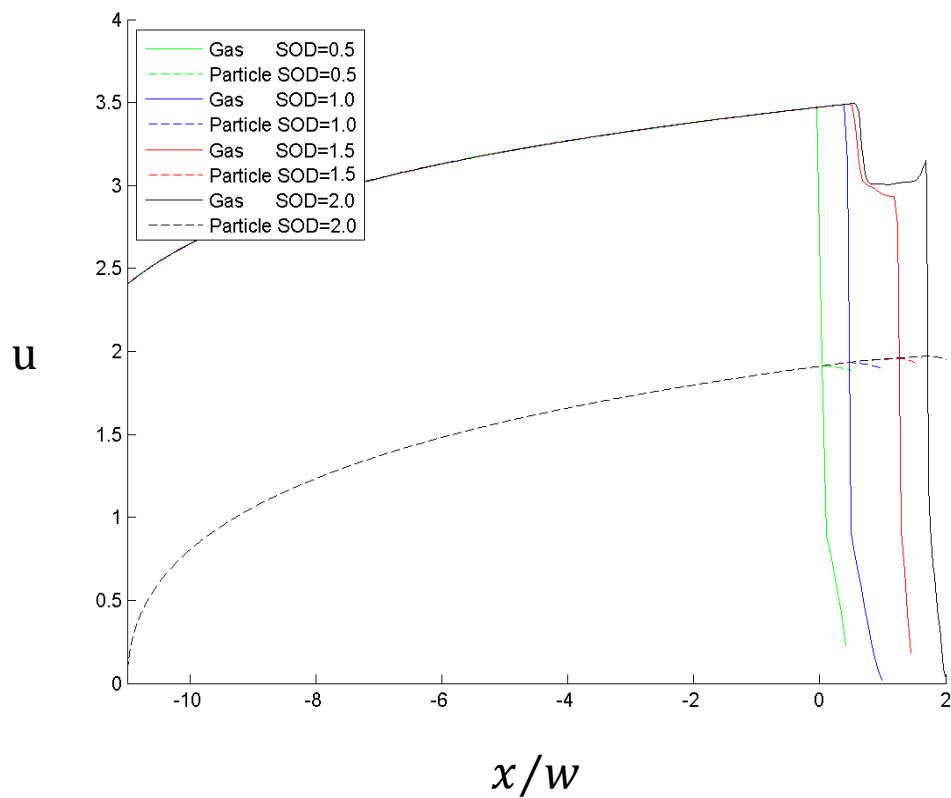


Figure 4.28 Velocity variation of particles injected at the $x/w = -11$.

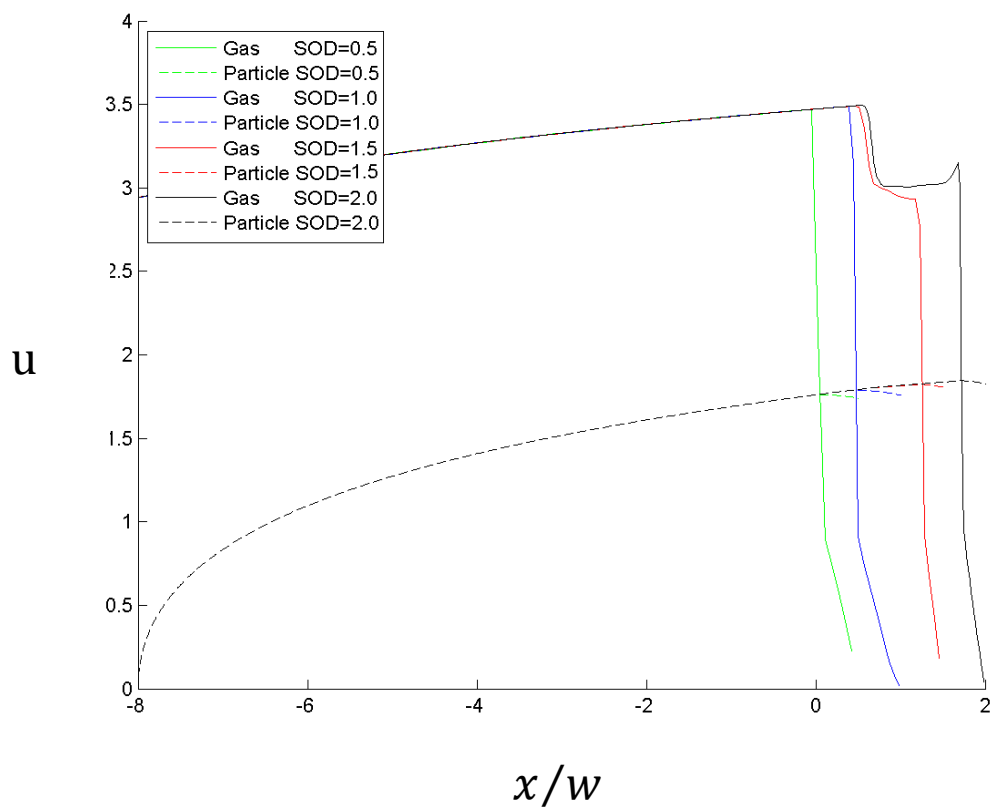


Figure 4.29 Velocity variation of particles injected at the $x/w = -8$

4.2.3 Heat transfer of particles

Apart from gains in kinetic energy, a particle also gains internal energy from the preheated gas in the CGDS process, and heat energy is transferred from the high temperature gas to the low temperature coating powder. A heat transfer model is developed. The temperature variations of particles injected

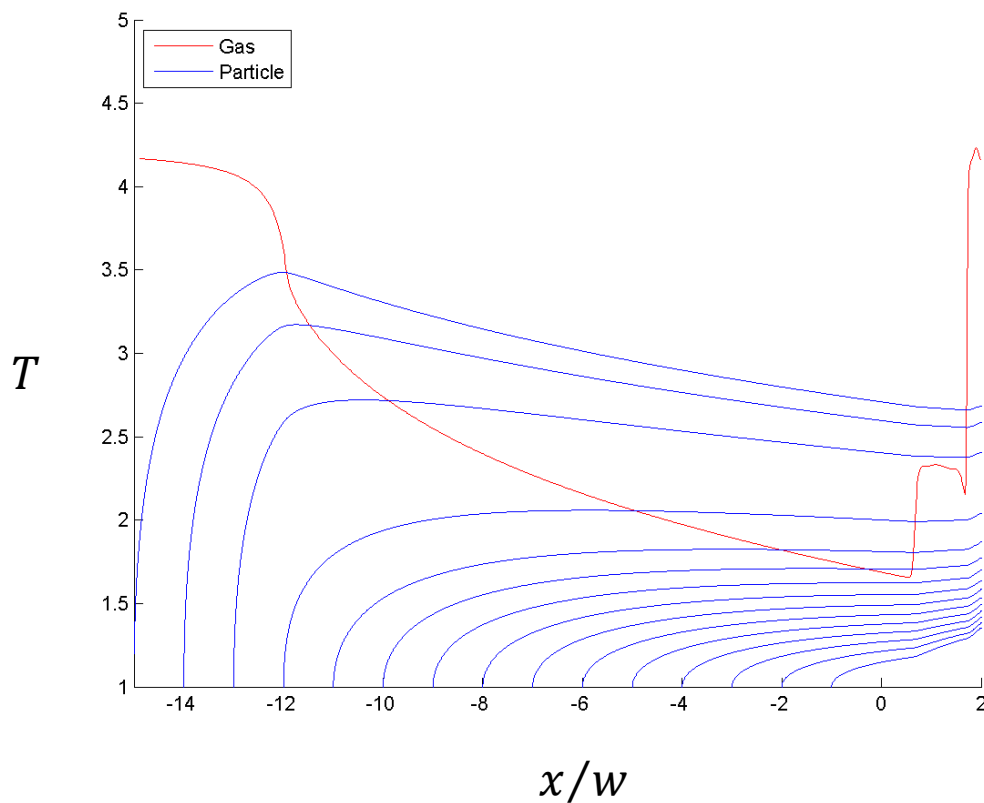


Figure 4.30 Temperature variations, SOD=2.

at different locations are shown in Figure 4.30. The result shows that particles are heated up rapidly in the converging zone of the nozzle due to the large temperature difference between gas and particles. The carrying gas

expands in the diverging zone, its temperature decreases and the particle temperature drops once $T_p > T_g$. The result also shows that T_p is higher if a particle is injected more upstream, especially in the converging zone of the nozzle. The gas temperature T_g increases after leaving the nozzle, and a high temperature region is formed in front of the substrate. However the temperature variation of particles in the region is small because the particles are travelling at high speed in that region and reach the substrate very soon after exiting from the nozzle. Therefore, the effect of SOD on particle impact temperature is very small, as shown in Figures 4.31 – 4.33.

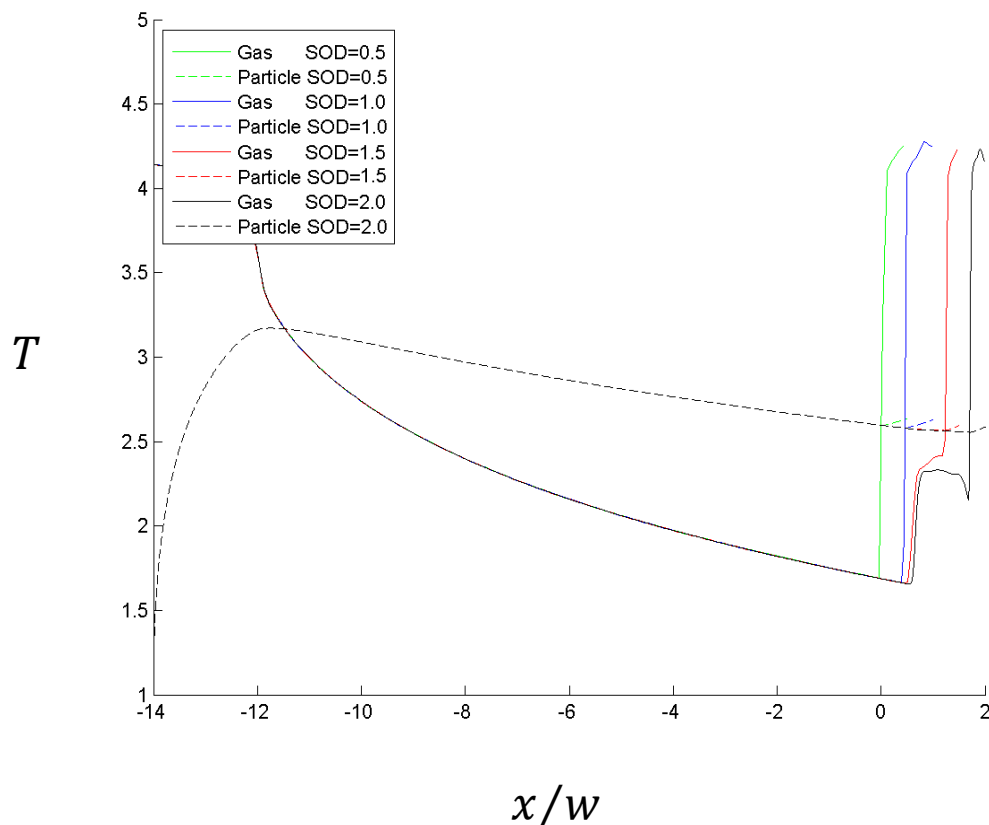


Figure 4.31 Temperature variation of particles injected at the $x/w = -14$.

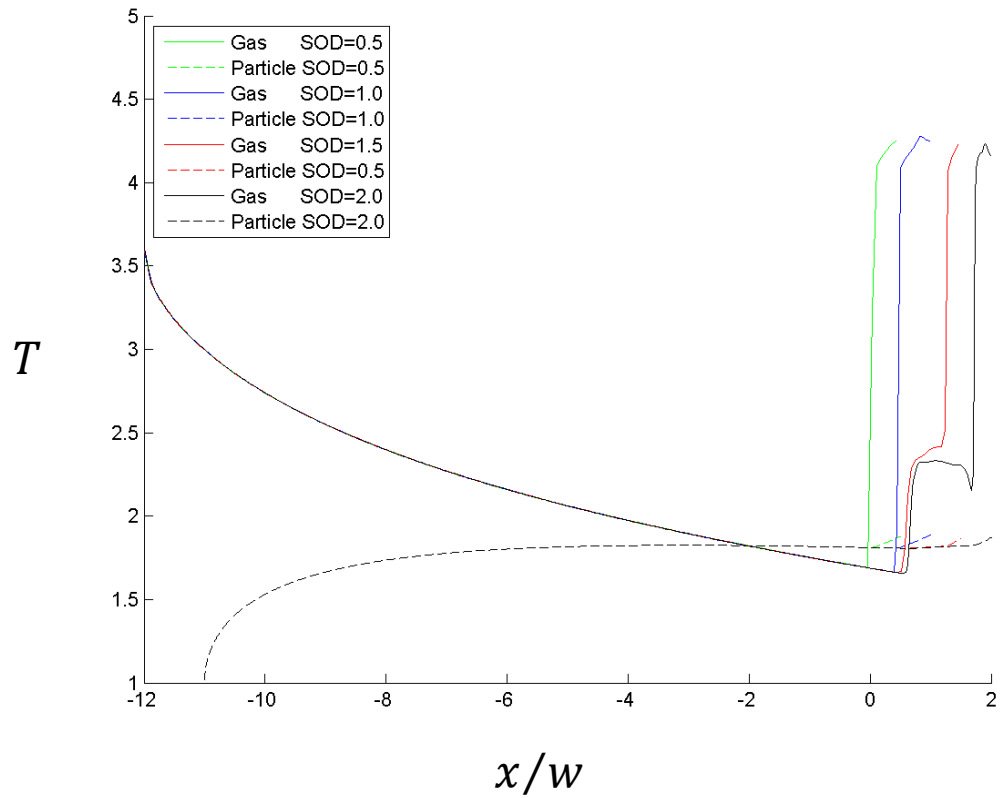


Figure 4.32 Temperature variation of particles injected at the $x/w = -11$.

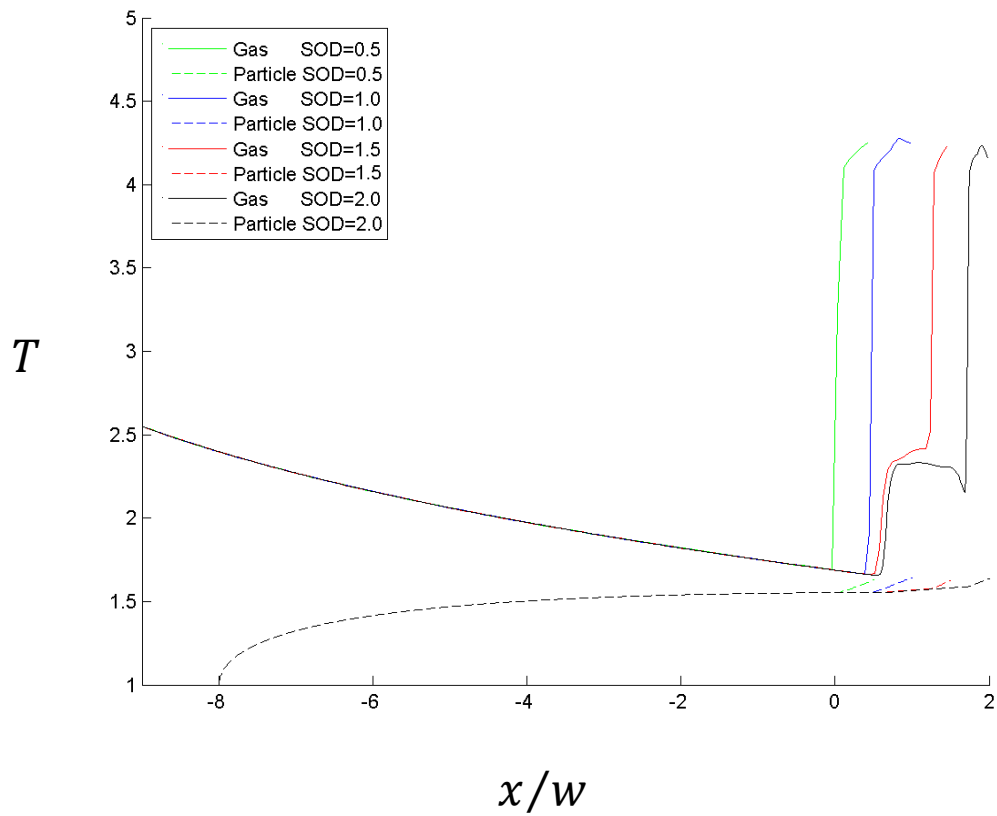


Figure 4.33 Temperature variation of particles injected at the $x/w = -8$.

4.2.4 Deposition of particles

The impact velocity of particle u_{impact} is required to exceed the critical velocity V_c for successful deposition in the CGDS process, and V_c is related to the impact temperature T_i (Equation 1.1). Figures 4.34 - 4.37 show the impact temperature, the corresponding critical velocity and the particle impact velocity of CGDS simulations with different SODs and injection locations. The results show that the higher the T_i , the lower the V_c ; and from previous results, the particles injected in the converging zone have a higher T_i , so depositions are successful for these particles.

There is a critical injection location x_c where $u_{impact} = V_c$, deposition is successful if particles are injected upstream of this location, and deposition fails if particles are injected downstream of it. These locations vary for different substrate locations, and they are listed in Table 4.3.

| | | | | |
|-------|------|------|------|------|
| SOD | 0.5 | 1.0 | 1.5 | 2.0 |
| x_c | -8.4 | -8.1 | -7.9 | -7.2 |

Table 4.3 Critical particle injection locations

From Table 4.3, x_c is closer to the nozzle exit for higher SODs, so it can be concluded that particles can be injected more downstream for high SOD for successful deposition.

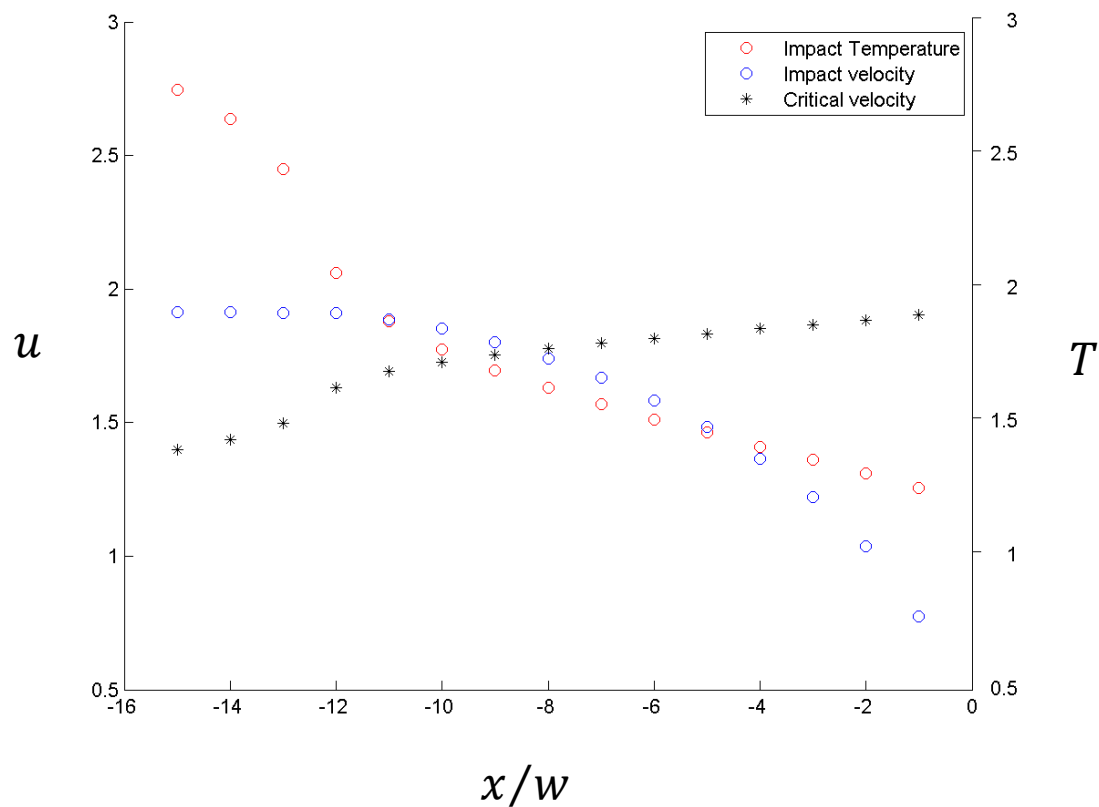


Figure 4.34 Impact velocity and temperature at different injection locations: $SOD=0.5$.

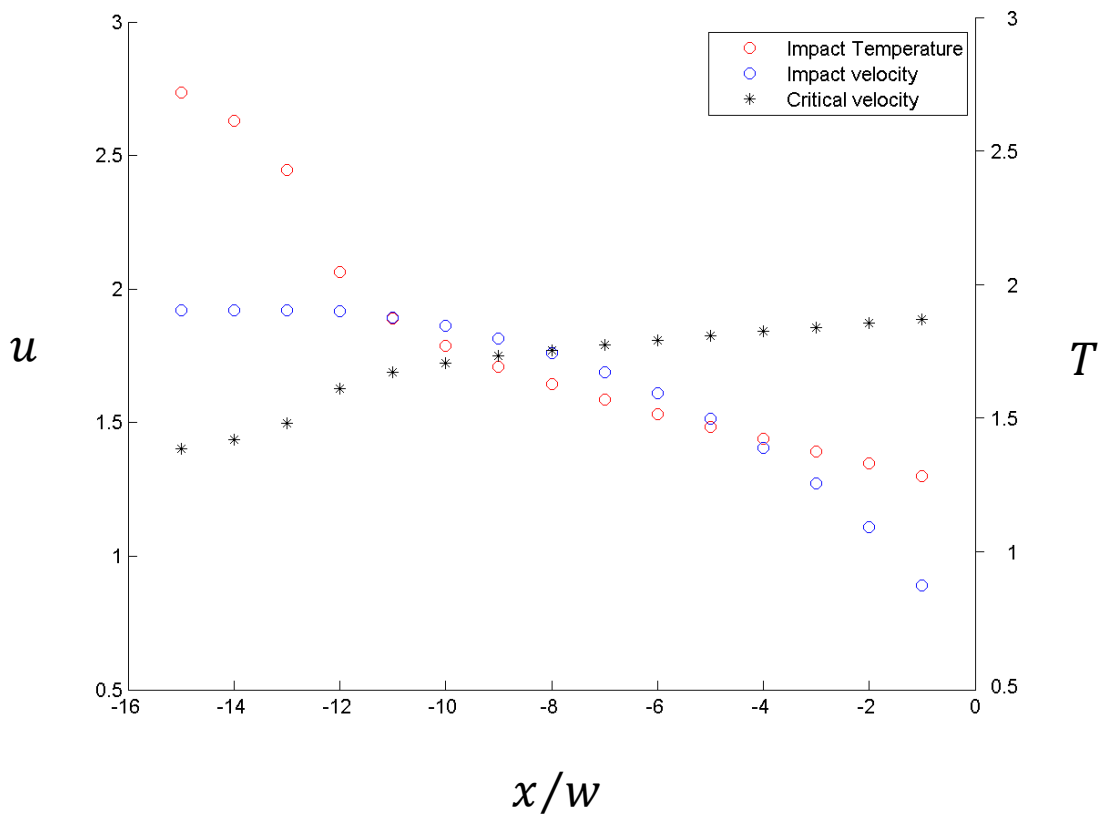


Figure 4.35 Impact velocity and temperature at different injection locations: $SOD=1.0$.

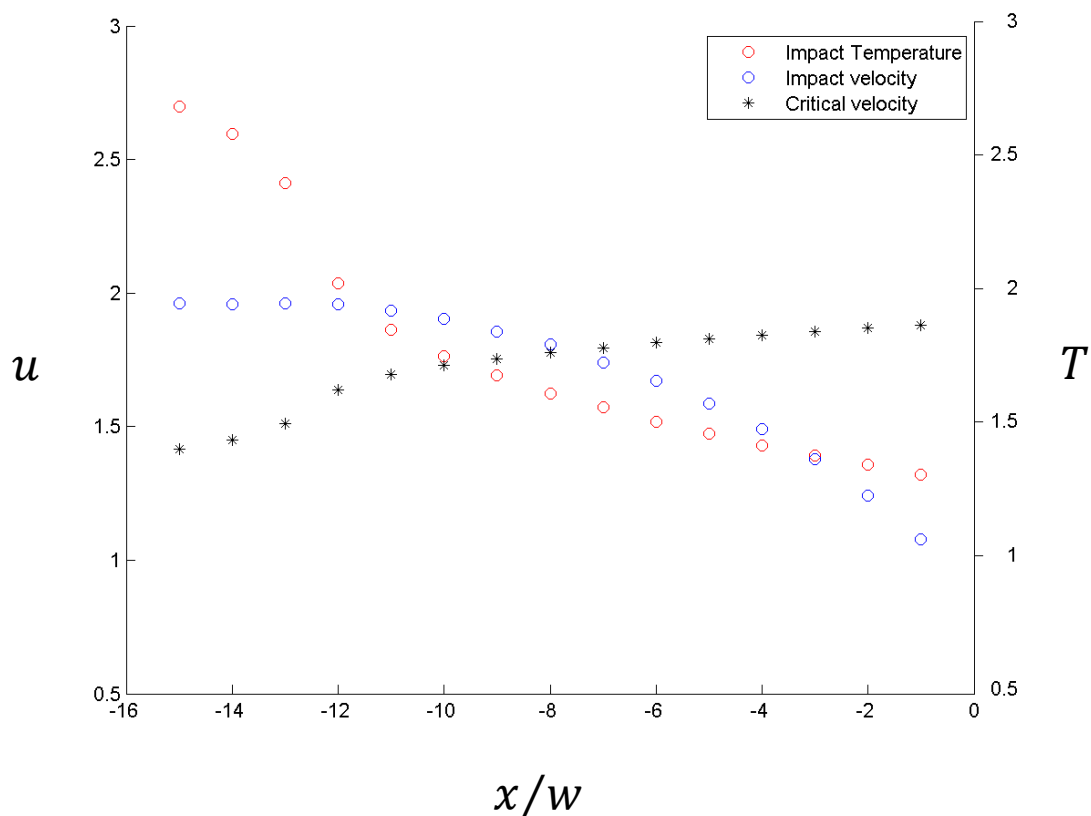


Figure 4.36 Impact velocity and temperature at different injection locations: SOD=1.5.

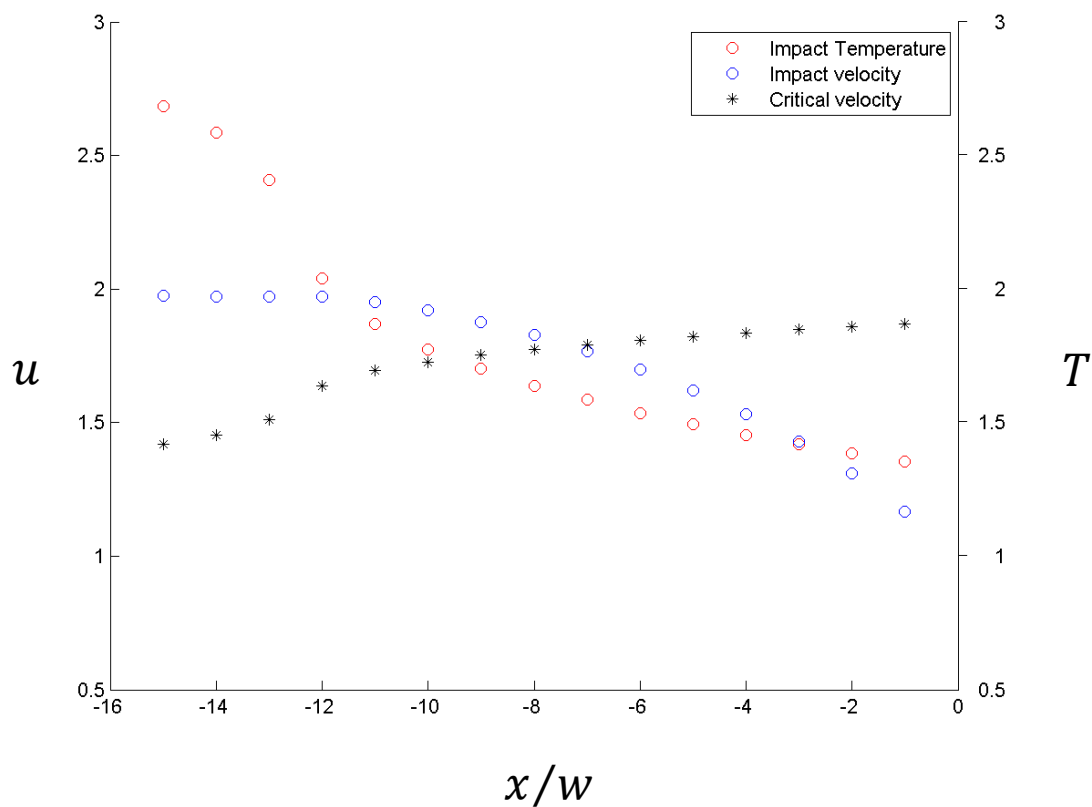


Figure 4.37 Impact velocity and temperature at different injection locations: SOD=2.0.

The size of the spray area of the CGDS process is also important for CGDS applications. Figure 4.38 is a sketch showing a typical particle injection pipe which is placed on the centre of the nozzle. Particle simulations are carried out to study the spray area ratio w_{spray}/w_{pipe} which is the ratio of the width of the spray area to the width of the injection pipe. In

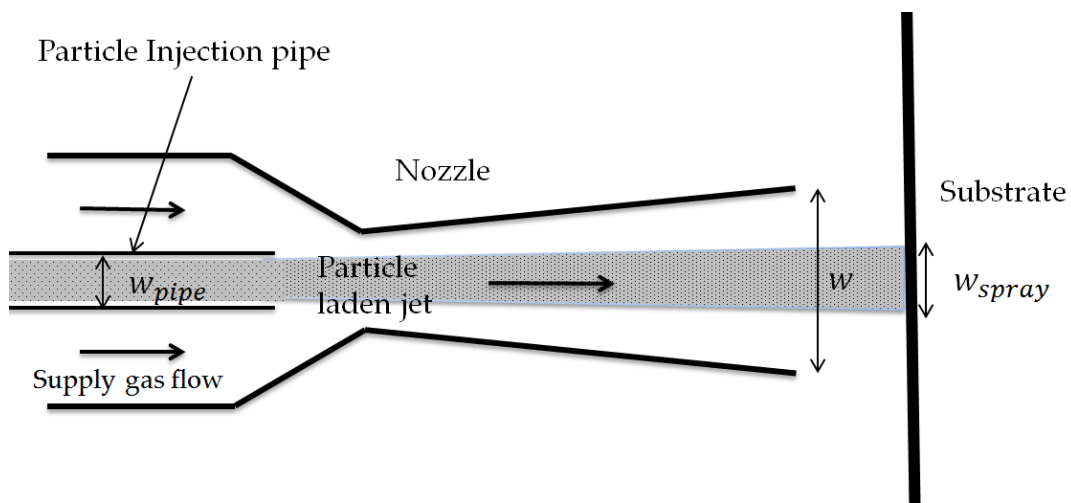


Figure 4.38 Schematic of the particle injection pipe in the CGDS system

the simulations, 1000 particles are initially placed across the width of the injection pipe $w_{pipe} = 0.3$, and the spray area ratio (w_{spray}/w_{pipe}) of different axial injection locations are shown in Table 4.2 and Figure 4.39. The spray width w_{spray} is defined as length of substrate where particle deposition is successful. The spray area ratio is larger when the substrate is further away from the nozzle and the spray area is very narrow when the injection pipe is placed in the converging zone ($x/w < -12$) of the nozzle; in

contrast, the spray area is maximum when the particles are injected just downstream ($x/w = -11$) of the nozzle throat.

| Injection locations (x/w) | SOD=0.5 | SOD=1 | SOD=1.5 | SOD=2.0 |
|-------------------------------|---------|-------|---------|---------|
| -15 | 0.04 | 0.04 | 0.04 | 0.05 |
| -14 | 0.08 | 0.08 | 0.09 | 0.10 |
| -13 | 0.17 | 0.17 | 0.17 | 0.16 |
| -12 | 2.44 | 2.52 | 2.58 | 2.63 |
| -11 | 2.72 | 2.81 | 2.89 | 2.96 |
| -10 | 2.41 | 2.48 | 2.54 | 2.60 |
| -9 | 2.16 | 2.22 | 2.27 | 2.31 |
| -8 | 1.98 | 2.02 | 2.06 | 2.10 |

Table 4.4 Particle injection locations of different SOD.

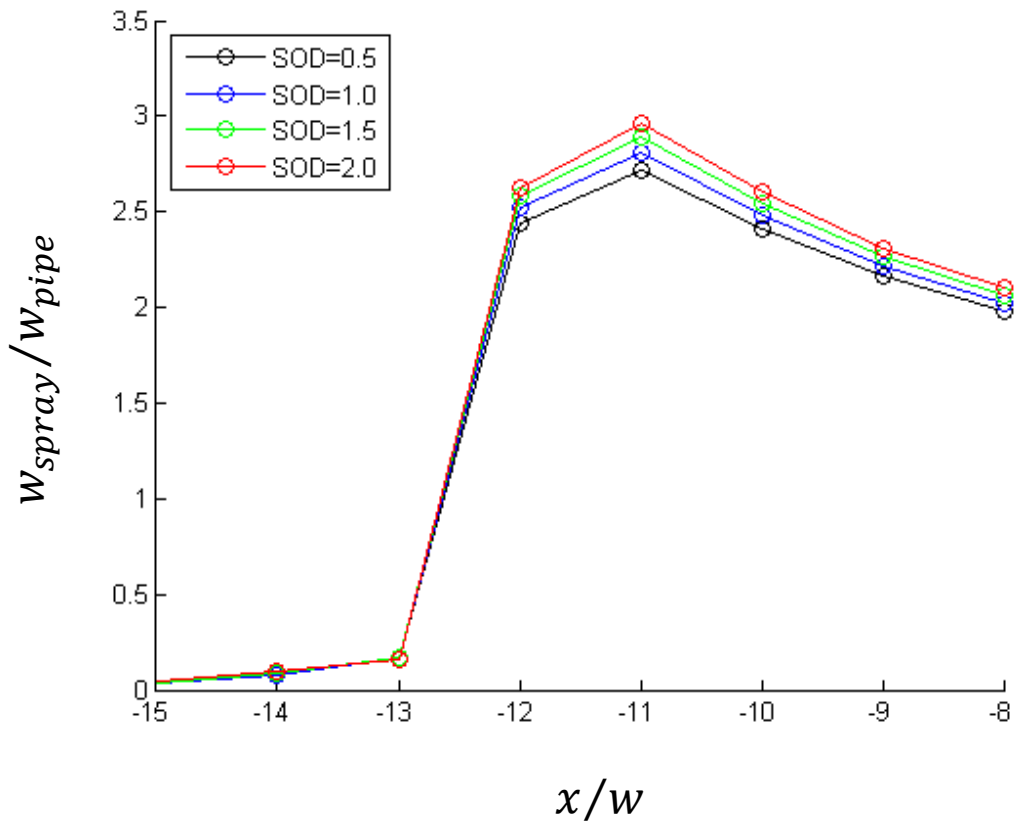


Figure 4.39 Spray area variations.

4.3 Conclusions

In the first part of this chapter, gas dynamics simulations results are discussed, showing that the internal nozzle flow of the CGDS process is independent of the substrate location, and it follows the one-dimensional nozzle theory. The pressure, density and temperature increase sharply and the gas velocity and Mach number drop significantly across the stand-off shock which is formed in front of the substrate in the impinging zone. The second part of this chapter shows the results of particle simulations, and the

particle motion and heat transfer are studied. The results show that the particle motion and heat transfer are independent of the substrate location; and the velocity and temperature variations of the particles in the impinging region are very small; therefore the impact conditions of the particles can be approximated by the conditions at the nozzle exit. Moreover, the location of the particle injection pipe plays an important role in the CGDS process; the results show that the more upstream the injection location is, the higher the impact velocity and temperature which is important for successful deposition. In addition, the injection location of particles also affects the size of the coating area; the coating area with particles injected in the converging zone is very narrow and the coating area can be maximized when the particles are injected just downstream of the nozzle throat.

5. Conclusions

The objective of this study was to provide a better understanding of the CGDS process by simulating the gas dynamics using a numerical method. The CE/SE solver, which is proved to be capable of simulating the CGDS gas dynamics, is applied to simulate the CGDS processes with different substrate stand-off distances. A particle simulation solver is developed based on the formulations of particle flight model, particle impact model and heat transfer model, and it is applied to the CE/SE results to simulate the particle motion and energetics in the CGDS process. The results give us a better understanding of the roles of different CGDS parameters, such as stand-off distance, particle injection location, carrying gas velocity and temperature, etc. These discoveries may help in the development of future CGDS systems which may have higher deposition efficiencies, better control of the coatings and lower operating costs.

References

Ahuja, K. K., and Burrin, R.H., "Control of Flow Separation by Sound," *AIAA Paper*, 84-2298, 1984

Alkhimov, A. P., A.N., Papyrin, Kosareve, V. F. , Nesterovich, A. N. and Shushpanov, M. M, "Method and Device for Coating," *European Patent No.* 0484533, 1995.

Alkhimov, A. P., A. N., Papyrin, Kosareve, V. F., Nesterovich, A. N. and Shushpanov, M. M., "Gas Dynamic Spraying Method for Applying a Coating," *U.S. Patent No.* 5, 302, 414, 1994.

Alkhimov, A. P., Kosareve, V.F., and Papyrin, A. N., "A Method of Cold Gas-Dynamic Spray Deposition," *Doklady Akademii Nauk SSSR*, 1990, Vol. 315, No. 5, pp. 1062-1065.

Alkhimov, A. P., Kosareve, V. F., Nesterovich, and Papyrin, A. N., "Method of Applying Coatings," 1990, *Russian Patent No.* 1618778.

Alkhimov, A. P., Kosareve, V. F., Nesterovich, A. N. and Papyrin, A. N., "Method of Applying Metal Powder Coatings," *Russian Patent No.* 1773072, 1992.

Alkhimov, A. P., Kosareve, V. F., Nesterovich, A. N., Papyrin, A. N. and Shushpanov, M. M., "Device for Applying Coatings," *Russian Patent No.*

1618777, 1990.

Alvi, F. S., Elavarsan, R., Shih, C., Gary, G., and Krothapalli, A., "Control of Supersonic Impinging Jet Flows using Microjets," *AIAA Journal*, Vol. 41, No. 7, 2003, pp. 1347-1355.

Anderson, J. D., *Modern Compressible Flow with Historical Perspective*, third edition, 2003, pp.202-218.

Asbury, S. C., Gunther, C. L., and Hunter, C. A., "A Passive Cavity Concept for Improving the Off-Design Performance of Fixed-Geometry Exhaust Nozzles," *AIAA Paper* 1996-2541, 1996.

Billig, F. S., "Shock-wave Shapes around Spherical and Cylindrical-nosed Bodies," *Journal of Spacecraft and Rockets.*, Vol. 4, No. 5, pp. 822-823, 1967.

Browning, J. A., "Thermal Spray Method Utilizing In-Transit Powder Particle Temperatures Below their Melting Point," *U.S. Patent* 5,271,965, 1993.

Carling, J. C., and Hunt, B. L., "The Near Wall Jet of a Normally Impinging, Uniform, Axisymmetric, Supersonic," *Journal of Fluid Mechanics*, Vol. 66, No. 1, 1974, pp. 159–176.

Chang, C. L., "Three-Dimensional Navier-Stokes Calculations Using the Modified Space-Time CESE Method," *AIAA Paper* 2007-5818, 2007.

Chang, S. C., "The Method of Space-Time Conservation Element and

Solution Element-A New Approach for Solving the Navier-Stokes and Euler Equations," *Journal of Computational Physics*, Vol. 199, 1995, pp. 295-324."

Chang, S. C., Wang, X. Y., and Chow, C. Y., "The Space-Time Conservation Element and Solution Element Method - A New High Resolution and Genuinely Multidimensional Paradigm for Solving Conservation Laws," *Journal of Computational Physics*, Vol. 156, No. 1, 1999, pp. 89-136.

Chang, S. C., Wang, X. Y., and Chow, C. Y., "The Space-Time Conservation Element and Solution Element Method- A New High Resolution and Genuinely Multidimensional Paradigm for Solving Conservation Laws. I. The Two Dimensional Time Marching Scheme," *NASA TM-1998-208843*, 1998

Chang, S. C., Yu., S. T., Himansu, A., Wang, X. Y., Chow, C. Y. and Loh, C. Y., "The Method of Space-Time Conservation Element and Solution Element-A New Paradigm for Numerical Solution of Conservation Laws," *Computational Fluid Dynamics Review*, Vol. 1, 1998, pp. 206-240.

Choi, J. J., Annaswamy, A. M., Lou, H., and Alvi, F. S., "Active Control of Supersonic Impingement Tones Using Steady and Pulsed Microjets," *Experiments in Fluids*, Vol. 41, No. 6, pp. 841-855, 2006.

- Donaldson, C., Snedeker, R. S., "A Study of Free Jet Impingement, Part 1: Mean Properties of Free and Impinging Jets," *Journal of Fluid Mechanics*, Vol. 45, No. 2, 1971, pp. 281-319.
- Dykhuisen, R. C., and Smith M. F., "Gas Dynamic Principles of Cold Spray," *Journal of Thermal Spray Technology*, Vol. 7, No. 2, 1998, pp. 205-212."
- Gabel, H. and Tapphorn, R. M., "Coating or Ablation Applicator with a Debris Recovery Attachment," U.S. Patent 5,795,626, 1998.
- Gottlieb, D. and Orszag, S., "Numerical Analysis of Spectral Method: Theory and Applications," *CBMS-NSF Regional Conference Series in Applied Mathematics*, 1977.
- Greenblatt, D., De Rosset, W. S., and Helfritch, D., "The Control of Flow Separation by Periodic Excitation," *Progress in Aerospace Sciences*, Vol. 36, 2000, pp. 487-545.
- Gubanov, O. I., Lunev, V. V., and Plastinina, L. N., "The Central Breakaway Zone with Interaction Between a Supersonic Underexpanded Jet and a Barrier," *Journal of Fluid Dynamics*, Vol. 6, 1973, pp. 298-301.
- Gummer, J. H., and Hunt, B. L., "The Impingement of a Non-Uniform, Axisymmetric, Supersonic Jet on a Perpendicular Flat Plate," *Israel Journal of Technology*, 1974, Vol. 12, No. 3-4, pp. 221-235.

- Harten, A., Engquist, B., Osher, S. and Chakravarthy, S. R., "Uniformly High Order Accurate Essentially Non-Oscillatory Schemes," *Journal of Computational Physics*, Vol. 71, 1987, pp. 231-303.
- Henderson, B., and Powell, A., "Experiments Concerning Tones Produced by an Axisymmetric Choked Jet Impinging on Flat Plates," *Journal of Sound and Vibration*, Vol. 168, No. 2, 1993, pp. 307–326.
- Hirsch, C., *Numerical Computation of Internal and External Flows*, Vol.2, 1990.
- Hiroshi K. and Kazuyazu M., "Gasdynamic Simulation of Aerosol Deposition Method," *Materials Transactions*, 2006, Vol. 47, No. 7, pp. 1620-1625.
- Huang, L. S., Maestrello, L., and Bryant, T. D., "Separation Control over an Airfoil at High Angles of Attach by Sound Emanating from the Surface," *AIAA paper*, 87-1261, 1987.
- Hunter, C. A., "An Experimental Analysis of Passive Shock-Boundary Layer Interaction Control for Improving the Off-Design Performance of Jet Exhaust Nozzles," M.S. Thesis, Joint Institute for Advancement of Flight Sciences, George Washington University, 1993.
- Hunter, C. A., "Experimental, Theoretical and Computational Investigation of Separated Nozzle Flows," *AIAA Paper* 1998-3107, 1998.

Hunter, C. A., "Experimental Investigation of Separated Nozzle Flows,"

Journal of Propulsion and Power, Vol. 20, No. 3, 2004, pp. 527-532.

Hunter, C. A., "Experimental, Theoretical and Computational Investigation

of Separated Nozzle Flows," *AIAA Paper* 1998-3107.

Krothapalli, A. "Discrete Tones Generated by an Impinging Underexpanded

Rectangular Jet," *AIAA Journal*, Vol.23, No. 12, 1985, pp. 1910-1915.

Krothapalli, A., Rajakuperan, E., Alvi, F. S., and Lourenco, L., "Flow Field

and Noise Characteristics of a Supersonic Impinging Jet," *Journal of Fluid*

Mechanics, Vol. 392, 1999, pp. 155–181.

Lam, G. C. Y., Leung, R. C. K., Leung, K.F ., Tang, S. K., "Computational Duct

Aeroacoustics using CE/SE Method," *AIAA Paper* 2008-2824, 2008.

Lamont, P. J., and Hunt, B. L., "The Impingement of Underexpanded

Axisymmetric Jets on Perpendicular and Inclined Flat Plates," *Journal of*

Fluid Mechanics, Vol. 100, No. 3, 1980, pp. 471–511.

Lele, K., "Compact Finite-Differences Schemes with Spectral-Like

Resolution," *Journal of Computational Physics*, Vol. 103, 1992, pp.16-42.

McCune, R. C., Papyrin, A. N., Hall, J. N. Riggs, W. L. and Zajchowski, P. H.,

"An Exploration of the Cold Gas–Dynamic Spray Method for Several

Material Systems," *Proceedings of the National Thermal Spray Conference*,

Houston Texas, ASM International, 1995, p. 1-3.

Middha, P., and Wexler, A. S., "Particle Focusing Characteristics of Sonic Jets," *Aerosol Science and Technology*, Vol. 37, 2003, pp. 907-915.

Middha, P., and Wexler, A. S., "Particle-Focusing Characteristics of Matched Aerodynamic Lenses," *Aerosol Science and Technology*, Vol. 39, 2005, pp. 222-230.

Neuwerth, G., "Acoustic Feedback of a Subsonic and Supersonic Free Jet Which Impinges on an Obstacle," *NASA TT F-15719*, 1974.

Payrin, A. N., "Cold Spray Technology," *Advance Material Process*, 2001, pp. 49-51."

Powell, A., "On Edge Tones and Associated Phenomena," *Acoustica*, Vol. 3, 1953, pp. 233-243.

Powell, A., "The Sound-Producing Oscillations of Round Underexpanded Jets Impinging on Normal Plates," *Journal of Acousical Society of America*, 1988, Vol. 83, No. 2, pp. 515-533.

Raletz, F., "Contribution to the Development of a Cold Gas Dynamic Spray System (C.G.D.S.) for the Realization of Nickel Coatings," PhD thesis, Université de Limoges, France, 2005.

Schmidt, T., Gartner, H., Kreye, H., Marple, B. R., Hyland, M., Lau, Y., Lima,

R. and Voyer (Eds), "New Developments in Cold Spray Based on Higher Gas- and Particle Temperatures, " *Thermal Spray 2006: Science, Innovation and Application*, ASM International, 2006, p. 35.

Schmidt, T., Gartner, Kreye, F. H., Borchers, C., Stoltenhoff, T., Kreye, H., Assadi, H., "Numerical and Microstructural Investigations of the Bonding Mechanisms in Cold Spraying," in: B. R. Marple, C. Moreau (Eds.), *Thermal Spray 2003: Advancing the Science and Applying the Technology*, May 5–8 2003, Vol. 1, ASM International, Orlando, FL, 2003, p. 1.

Seifert, A., Darabi, A., and Wygnanski, I., "Delay of Airfoil Stall by Periodic Excitation," *Journal of Aircraft*, Vol. 33, No. 4, 1996, pp. 691-698

Shu, C. W., Zang, Z. C., Erlebacher, G., Whitaker, D. and Osher, S., "High-Order ENO Schemes Applied to Two- and Three-Dimensional Compressible Flow," *Journal of Applied Numerical Mathematics*, Vol. 1, No. 9, 1992, pp. 45-71.

Smith, G. H., Kenmore, N. Y., Eschenback, R. C, and Pelton, J. F., "Jet Plating of High Melting Point Materials," *U.S. Patent* No. 2,861,900, 1958.

Tam, C. K. W., and Ahuja, K. K., "Theoretical Model of Discrete Tone Generation by Impinging Jets," *Journal of Fluid Mechanics*, Vol. 214, 1990, pp. 67–87.

Tapphorn, R. M. and Gabel, H., "Coating or Ablation Applicator with Debris Recovery Attachment," *U.S. Patent 6,074,135*, 2000.

Tapphorn, R. M. and Gabel, H., "Powder Fluidizing Devices and Portable Powder-Deposition Apparatus for Coating and Spray Forming," *U.S. Patent 6,715,640*, 2004

Taylor, K., Jodoin, B., and Karov, "Particle Loading Effect in Cold Spray," *Journal of Thermal Spray Technology*, Vol. 15, No. 2, 2006, pp. 273-279.

Van Steenkiste, T. H., Smith, J. R., Teets, R. E., Moleski, J. J. and Gorkiewiez, D. W., "Kinectic Spray Coating Apparatus," *U.S. Patent 6,283,386*, 2001.

Van Steenkiste, T. H., Smith, J. R., Teets, R. E., Moleski, J. J. and Gorkiewiez, D. W., "Kinetic Spray Coating Method and Apparatus," *U.S. Patent 6,139,913*, 2000.

Van Steenkiste, T. H., Smith, J. R., Teets, R. E., Moleski, J. J. and Gorkiewiez, D. W., "Spray Coatings For Suspension Damper Rods," *U.S. Patent 6,189,663*, 2001.

Vejrazka, J., Tihon, J., Marty, Ph., and Sobollk, V., "Effect of an External Excitation on the Flow Structure in a Circular Impinging Jet," *Physics of Fluids*, Vol. 17, 2005, No. 105102.

Venkatachari, B., Cheng, G. C. and Chang, S. C., "Development of a Transient

Viscous Flow Solver Based on Conservation Element-Solution Element Framework," *AIAA Paper* 2004-3413, 2004.

von Neumann, J., Richtmyer, R. D., "A Method for the Numerical Calculation of Hydrodynamics shocks," *Journal of Applied Physics*, Vol. 21, 1950, pp. 232-237.

Washington, D., Alvi, F. S., Strykowski, P. J., and Krothapalli, A., "Multi-Axis Fluidic Thrust Vectoring of a Supersonic Jet Using Counterflow," *AIAA Journal*, Vol. 34, No. 8, 1996, pp. 1734-1736.

Yee, H. C., Warming, R. F. and Harten, A., "Implicit Total Variation Diminishing Schemes for Steady State Calculations," *Journal of Computational Physics*, Vol. 57, 1985, pp. 327-360.